

The Pennsylvania State University
The Graduate School
Department of Energy and Geo-Environmental Engineering

**THE INFLUENCE OF A FRACTURE TIP ON
TWO-PHASE FLOW DISPLACEMENT PROCESSES**

A Thesis in
Petroleum and Natural Gas Engineering
by

Abdullah F. Alajmi

Copyright 2003 Abdullah F. Alajmi

Submitted in Partial Fulfillment
of the Requirements
for the Degree of

Doctor of Philosophy

August 2003

The thesis of Abdullah F. Alajmi has been reviewed and approved* by the following:

A. S. Grader
Professor of Petroleum and Natural Gas Engineering
Thesis Advisor
Chair of Committee

Turgay Ertekin
Professor of Petroleum and Natural Gas Engineering
Program Chair of Petroleum and Natural Gas Engineering

Phillip M. Halleck
Associate Professor of Petroleum and Natural Gas Engineering

Derek Elsworth
Professor of Energy and Geo-Environmental Engineering
Associate Dean for Research
College of Earth and Mineral Sciences

Michael Adewumi
Professor of Petroleum and Natural Gas Engineering
Graduate Program Chair in Petroleum and Natural Gas Engineering

* Signatures are on file in the Graduate School.

ABSTRACT

This work focuses on multi-phase flow in the presence of a fracture tip. Fluid flow interactions between a fracture and the surrounding matrix are not well documented in the literature, especially in the case of a fracture tip. This work studies two-phase fluid flow (Water-Oil) displacements in layered Berea Sandstones that have been artificially fractured with a single extensional fracture perpendicular to the natural layers. Two experiments are considered in this work. In the first experiment, the fracture was induced at the inlet end of the sample and it spanned the first third of the core. Thus, the diverging flow at the tip of the fracture was studied. In the second experiment, the fracture was induced at the outlet end of the sample and it spanned about one third of the core. Multi-phase fluid flow convergence to the fracture tip was studied in this experiment. The temporal and spatial saturation distributions of the two cases were determined using x-ray computed tomography, CT.

The 4D-CT experimental data and recovery information were used as the basis for simulation in an effort to determine the interaction of fracture-matrix environment with multi-phase flow. At the tip of the fracture, the two experiments showed different fluid flow patterns. The presence of the tip of the fracture in both experiments influenced the displacement path along each layer.

The presence of the fracture tip is essential for highlighting the property contrast between the natural layers in the sample, much more than in a displacement process without a fracture. Matches of the simulation results to the experimental data showed that when the fracture is at the inlet end, fluid diverges from the fracture to the matrix along the entire

length of the fracture. The displaced phase is delayed in the regions neighboring the fracture and it preferentially flowed in the outer regions of the core.

Understanding multi-phase fluid flow in fractured rocks is essential for designing and optimizing hydrocarbon recovery processes. The fluid flow interactions between the fractures and the matrix have a significant impact on displacement processes. This work provides modeling results and experimental observations that explain some of the displacement processes around a fracture tip.

TABLE OF CONTENTS

LIST OF FIGURES	vii
LIST OF TABLES	x
NOMENCLATURE	xi
ACKNOWLEDGEMENTS	xiii
Chapter 1. INTRODUCTION	1
Chapter 3. HYPOTHESES AND OBJECTIVE	9
3.1 Hypotheses.....	9
3.2 Objectives	12
3.3 Approach	12
Chapter 4. EXPERIMENTAL DATA	14
4.1 Fluids	14
4.2 Rock Samples	14
4.3 Experimental Apparatus	16
4.4 Experimental Procedure	16
4.4.1 Porosity	19
4.4.2 Absolute Permeability	26
4.4.3 Oil Injection	29
4.4.4 Oil Flood Patterns Caused by Permeability and Porosity Variations	35
4.4.5 Water Injection	42
Chapter 5. MODELING	47
5.1 Introduction.....	47
5.2 Simulator Input Requirements	47
5.3 History Matching Method	48
5.3.1 Step One.....	48
5.3.2 Step Two	50

5.3.3 Step Three	50
5.3.4 Step Four	51
5.3.5 Step Five	51
5.3.6 Algorithm Verification	52
5.4 The Two-Dimensional Model	56
5.4.1 Preliminary Results	56
5.5 The Three-Dimensional Model	65
Chapter 6. RESULTS AND DISCUSSION	69
6.1 Oil Flood	69
6.2 Water Flood	87
Chapter 7. CONCLUSIONS	99
REFERENCES	102
APPENDIX A	106
APPENDIX B	110
APPENDIX C	117
APPENDIX D	119

List of Figures

Figure 3.1: Diagram of the matrix-fracture system and the fluid flow behavior	10
Figure 3.2: Schematic drawing of different fluid flow patterns.....	11
Figure 3.3: Schematic diagram of the approach.	13
Figure 4.1: Dry images of the core. Schematic drawing showing where the 460 images were acquired along the core	15
Figure 4.2: Stages of the modified Brazilian Test	17
Figure 4.3: Fracture inducement in the laboratory. A: Before fracturing. B: After fracturing.....	18
Figure 4.4: Dry images of core after fracture. Same scanning position as Figure 4.1	20
Figure 4.5: Some slices from the high-resolution scanner.....	21
Figure 4.6: A) Average porosity profile across the core layers. B) Porosity profile along one layer	23
Figure 4.7: Axial slices of the two experiments showing the dry and porosity maps of each experiment	24
Figure 4.8: Dry reconstruction with porosity images in three locations along the core ...	25
Figure 4.9: Schematic Reconstruction of the region of major pressure drop	27
Figure 4.10: Porosity images with the 15 layers.....	28
Figure 4.11: Porosity and absolute permeability as a function of layer position.....	30
Figure 4.12: Oil saturation at different oil pore volume injected	31
Figure 4.13: Axial oil saturation maps of the second experiment at different pore pore volume injected.....	32
Figure 4.14: Two plates of images at two stages of the oil injection process. Top: at 0.051 PVOI. Bottom: at 0.143 PVOI	34
Figure 4.15: Axial slice of the dry core showing the three investigated areas	36
Figure 4.16: Oil saturation profiles at inlet side of core, position A in Figure 4.15	37
Figure 4.17: Oil saturation profiles at fracture tip, position B in Figure 4.15	38
Figure 4.18: Average oil saturation as a function of pore volumes of oil injected.....	40
Figure 4.19: Oil saturation profiles at away from the fracture tip, position C in Figure 4.15.....	41
Figure 4.20: Axial slices during the water flood at different values of pore volumes injected, prior to breakthrough.....	43
Figure 4.21: Water saturation profiles across the layers at the fracture tip	44

Figure 4.22: Water saturation profiles across layers away from the fracture tip	45
Figure 4.23: Axial slice of water flood at different pore volume injected for the second experiment	46
Figure 5.1: Schematic chart of the history match technique.....	49
Figure 5.2: Verification of optimization algorithm using the relative permeability curves ..	53
Figure 5.3: Reduction of error in the verification stage.....	54
Figure 5.4: Simulated average saturation along the sample used for verification of the optimization algorithm.....	55
Figure 5.5: Simulation grid for the two-dimensional system	57
Figure 5.6: Simulated oil saturation for the two-dimensional single-layer case.....	59
Figure 5.7: Experimental and simulated oil saturation maps for the two-dimensional system	60
Figure 5.8: The major three layers in the core	61
Figure 5.9: Simulated and experimental oil profiles of layer 8 at different pore volume. 62	
Figure 5.10: Simulated and experimental oil saturation for layers 9 and 10 at 0.143 PVOI	63
Figure 5.11: An axial slice of the simulated water flood for the two-dimensional model	64
Figure 5.13: Three Dimensional layout of the system.....	26
Figure 5.14: Simulated and experimental axial oil saturation maps for layer 8	67
Figure 5.15: Simulated and experimental oil saturation at 0.143 PVOI.....	68
Figure 6.1: Four maps showing streamline of two fluids at 0.212 PVOI. a: Oil saturation map. b: Injected fluid streamline map. c: Displaced fluid streamline map. d: Injected and displaced fluids streamline map	70
Figure 6.2: a) Expanded view of the oil streamlines during the oil flood. b) Combined streamlines map shown at the actual proportions of the core ...	72
Figure 6.3: Sketches of fracture-matrix interaction during two-phase flow	73
Figure 6.4: Simulation grid for a two layer system	75
Figure 6.5: Saturation and pressure profiles for two isolated layers.....	76
Figure 6.6: Oil saturation profiles for the low k and ϕ layer as a function of inter-layer communication.....	77
Figure 6.7: Oil saturation profiles for the high k and ϕ layer as a function of inter-layer communication.....	78
Figure 6.8: Average oil saturation profiles for the two-layered system, with and without inter-layer communication	80

Figure 6.9: Oil saturation transition along the two layers (high and low).	82
Figure 6.10: Oil saturation profiles across layers just before the fracture tip	84
Figure 6.11: Oil saturation profiles across layers just ahead of the fracture tip	85
Figure 6.12: Tip influence on oil flow rate at different location of the core	86
Figure 6.13: Axial slices showing water saturation during various stages of the water flood	88
Figure 6.14: Illustration of water volume before and ahead of the fracture tip	89
Figure 6.15: Illustration of first test of water saturation maps and capillary pressure curves	91
Figure 6.16: Illustration of second test of water saturation maps and capillary pressure curves	92
Figure 6.17: Illustration of third test of water saturation maps and capillary pressure curves	94
Figure 6.18: Illustration of fourth test of water saturation maps and capillary pressure curves	95
Figure 6.19: Illustration of water saturation map and capillary pressure curves after the improvement	97
Figure 6.20: Illustration of water saturation map and capillary pressure and relative permeability curves for the matrix and fracture.....	98

List of Tables

Table 4.1: Average porosity and correlated absolute permeability of layers	28
----------------------------------------------------------------------------------	----

NOMENCLATURE

ROMAN

A	= cross-sectional area normal to flow
a	= Corey's equation coefficient
b	= Corey's equation coefficient
c	= Corey's equation coefficient
CT	= CT number
d	= Corey's equation coefficient
G	= sensitivity coefficient matrix
H	= Hessian matrix
J	= least-square function
k	= permeability
kr	= relative permeability
L	= length
p	= pressure
q	= flow rate
s_{wr}	= irreducible water saturation
s_o	= oil saturation
s_{or}	= residual oil saturation
s_w	= water saturation

GREEK

α	= step size
----------	-------------

ε = improvement term

μ = viscosity, cp

ϕ = porosity

λ = stability factor

SUBSCRIPTS

abs = absolute

avg = average

cor = correlation

mb = material balance

o = oil

w = water

ACKNOWLEDGEMENTS

All thanks are due to Allah (God) the most merciful and most generous for the achievement and the completion of my graduate studies.

I want to express my deep appreciation and unlimited thanks to my parents and my family (brothers and sisters) for their continuous moral support. I want to thank my wife and my children for their support, patience, understanding and sacrifice.

I would like to express my gratitude and appreciation to the thesis advisor, Dr. Abraham S. Grader for his continues support, guidance and encouragement. Dr. Grader's great personality made me learn from him many things beyond the academic work. I also would like to thank the committee members, Dr. Turgay Ertekin, Dr. Phillip Halleck, and Dr. Derek Elsworth, for their guidance and positive criticism. I want to thank all my fellow PNGE friends for their kindness and support. Special thanks go to my colleagues, Majid Al-Wadahi, Meshal Algharaib, Gaoming Li, Mohammad Alajmi, Robert Strout, Tohami Eltohami, Saad Al-madhi and Fasial Al-Faqeer for their support and assistance.

Many thanks are due to Kuwait University and Pennsylvania State University for making this research project possible.

Chapter 1

INTRODUCTION

Natural and artificially-induced fractures in a reservoir have a great impact on fluid flow patterns and on the ability to recover hydrocarbons. In tight formations, the naturally fractured system provides access to the hydrocarbon fluids stored in the matrix. Fractures can have a negative effect on recovery process when they form bypass paths, especially in production-injection systems. For example, injected fluid may preferentially flow through the fractures leaving behind inaccessible and non-contacted hydrocarbons. Fractures can enhance the efficiency of displacement operations when the main direction of flow is perpendicular to the direction of fractures. Fracture may also be non-conductive and form barriers to fluid flow. The mass transport between the fractures and the surrounding matrix has an important role predicting and optimizing recovery processes from fractured reservoirs.

It is important to understand the local and global effect of fluids on reservoir performance. In this research, we are studying a porous medium that has a single fracture and a fracture tip. The main goal of this work is to study the influence of the fracture tip on multi-phase flow and its influence on fracture-matrix interactions. Hydrocarbon recovery depends on the interaction between fluids in the fractures and in the matrix. In this work, two-phase flow experiments of partially-fractured layered Berea sandstone cores are analyzed and simulated. In these experiments, the fluid phases were benzyl alcohol and NaI-tagged water. The rock samples were artificially fractured using the modified Brazilian Test. The displacement processes were performed in a horizontal direction. Saturation distributions at different values of pore volumes of water and oil

injected were determined using X-ray computer tomograph (CT). The inverse numerical modeling is expected to yield the fluid transport properties of the matrix and the fracture, and provide new analysis tools to directly relate four-dimensional saturation distributions to these properties.

Chapter 2

LITERATURE REVIEW

Fractures play an important role in fluid mass transport in rock formations. There are two types of fractures, permeable and sealed. The permeable fractures provide high porosity and permeability channels that enhance the process of fluid transport. These fractures may be artificially induced or naturally formed. Sealed natural fractures are barriers due to their low porosity and permeability. In the petroleum industry, the permeable natural and artificially induced fractures increase the productivity of wells. They increase the connectivity between the well and the reservoir.

2.1 Multi-Phase Flow Displacement

The conceptualization of a system containing two fluid phases and a solid phase is as follows. The porous medium is composed of a solid phase and a connected void space in which the fluids may move and interact. The two phases, oil and water, are considered here to be immiscible and to have distinct thermodynamic properties. When these two fluids are in contact a clearly defined interface exists between them reflecting the interfacial tension.

The immiscible two-phase flow in a partially fractured layered system is complex. The impact of the tip of fracture on the fluid flow displacement needs to be investigated in detail. It is important to try to understand the behavior of fluids upstream and downstream of the fracture tip. This understanding will improve our ability to predict the

recovery of hydrocarbons, disposal of waste materials, and other fluid transport processes in fractured porous media.

2.2 Relative Permeability

When two fluids flow simultaneously through a porous medium, the overall flow characteristics of each of the fluids are determined by fluid-fluid and fluid-solid interaction. Darcy introduced the concept of the rock absolute permeability, k , to describe the ability of the rock to transmit a single fluid.

$$k_{abs} = \frac{q\mu}{A\left(\frac{\Delta p}{\Delta L}\right)} \quad (2.1)$$

The flow rate, q , of a fluid through a porous medium is proportional to the pressure gradient, $\Delta P / \Delta L$, and the cross sectional area, A , normal to the direction of the flow, and inversely proportional to the viscosity of the fluid, μ . When there are two or more fluids flowing simultaneously through the rock, the permeability of each fluid is expressed as a function of the absolute permeability of a single fluid flowing through the rock, k_{abs} . and k_j is the effective permeability of the fluid j in the presence of other fluids. In the case of two fluids, the relative permeability, k_{rj} , is:

$$k_{rj} = \frac{k_j}{k_{abs}} \quad (2.2)$$

the relative permeability, k_{rj} , is a dimensionless quantity that represents the ability of the rock to transport fluids in a multi-phase environment. The value of k_j changes depending

on the saturation of each phase. Therefore, the relative permeabilities are functions of saturations of the fluids in the porous media.

2.3 History Matching Approach

History matching is a tool that is used as an inverse solution technique to obtain the system parameters. History matching techniques are used to provide appropriate parameters as inputs to predictive models. The simulation outputs are used by history matching algorithms for testing the improvement of the matching process. When a satisfactory history match is obtained, the optimization process is terminated.

Kruger (1961) presented the first report on a history matching technique applied to reservoir characterization. *Archer and Wong* (1973) introduced a history matching technique to determine the relative permeability from core flood data. They used a trial and error method to determine the relative permeabilities that created a match to the production and pressure history of the core flood experiments. *Sigmund and McCaffery* (1979) introduced automatic history matching to this process. *Watson et al.* (1980) developed an automatic history matching algorithm to estimate the porosity, permeability and coefficients of the relative permeability functions in two-phase reservoirs.

Kerig and Watson (1987) and *Watson et al.* (1986) presented a new algorithm for estimating the relative permeabilities from the displacement experiments. *Chardaire-Riviere et al.* (1990, 1992) estimated the relative permeability and capillary pressure simultaneously using a least-squares method technique, and optimal control theory was used to minimize the error function. For the first time, the saturation profiles along the

core at different times were used together with cumulative production data, and pressure drop in history matching.

Yang and Watson (1991) introduced Bayesian theory to incorporate prior information in determining relative permeability, which greatly reduced the uncertainty. *Savioli et al.* (1992) compared different algorithms used in history matching. *Nordtvedt et al.* (1993) applied history matching to simultaneously extract relative permeabilities and capillary pressure from the centrifuge experiments. *Nordtvedt et al.* (1996) analyzed three-phase flow problems with similar method. *Akin Demiral* (1997) and *Akin and Kovscek* (1999) studied imbibitions processes with history matching. They matched the saturation distribution acquired by a CT scanner to extract the relative permeabilities and capillary pressure, using a simulated annealing global optimization technique. Recently *Kulkarni and Datta-Gupta* (1999) presented a streamline-based approach for estimating relative permeability from production data. One of the advantages of using a streamline simulator is that the sensitivity coefficients can be calculated analytically.

2.4 Concept of Fracture

A fracture is typically defined as a surface or a zone in which a loss of cohesion has taken place in a rock. A natural fracture is any break or crack occurring in the rock, including those cracks which can be identified by the presence of mineralization. Induced fractures are cracks or breaks that result from experimental work in laboratory coring (such as breaks along the bedding plane), or induced in the formation to enhance productivity. Fracture orientation is important in multi-phase fluid flow. It is a key of having a successful hydrocarbon recovery processes.

The presence of fractures improves the porosity and permeability of the system. In some rocks like carbonate rocks, where fracturing is common because they are brittle, fractures only slightly increase the porosity but heavily impact permeability. Some reservoirs have such low matrix permeability that fractures provide the permeability necessary to produce oil.

The permeability of a fracture to the fluid flow decreases under compressive stress. The aperture decreases under increasing compression, and the resistance to flow increases. Also, the fracture permeability varies with fluid pressure. Increasing the fluid pressure increases the permeability because it causes the fracture to open, and decrease the area of contact between the surfaces.

Walsh (1981) studied the effect of pore pressure and confining pressure on fracture permeability. He described how fluid flow through a fracture varies as a function of pore fluid pressure and external confining pressure. A fracture is assumed to be two rough surfaces in contact. Resistance to flow through the fracture is caused by viscous drag of the fluid in the narrow openings between the surfaces and by the tortuosity of the flow path as fluid is diverted around asperities in contact. *Abdallah et al.* (1995) studied the thermal convection of fluid in fractured media the results suggest that convection phenomenon should not be neglected in modeling thermal flow in fractured rock masses. Convection is sensitive to the hydraulic aperture (pore fracture) of the fracture, the circulation velocity and the viscosity of the fluid. *Waite et al.* (1999) conducted a series of experiments to study the movement of water through four artificial fractures, each with different two-dimensional surface topography. Their main focus was to determine how the cubic law, derived for fluid flow through parallel plates, could be modified to

accommodate a tortuous fracture geometry. *Grader et al.* (2000) studied fractured-matrix interaction during the two-phase fluid flow. They used a layered Berea Sandstone core that was fractured by a Brazilian-like test. The fracture was internal and did not reach either ends of the core. CT imaging was used to scan the core at different stages of the experiment. CT imaging was used to capture the movement of the displaced and displacing fluids in the core, and quantify the interaction between the fracture and the matrix. The single experiment described in the above work did not reach the residual water saturation and did not flood the core with water. Also since both of the fracture tips were near the end of the core, the displacement front in the non-fractured regions was not established.

In this research, experiments with partially fractured cores (fracture tip) are analyzed and simulated, since in the literature no work is reported on the role of the tip of the fracture on fluid flow. The experiments and modeling investigate the influence of the fracture tip on two-phase displacement processes.

Chapter 3

HYPOTHESES AND OBJECTIVE

3.1 Hypotheses

Figure 3.1 shows a picture of one of the layered core used in this research with three slices representing different locations in the core. The extensional fracture spans about half of the length of the core. It also shows an axial slice through the center of the core after fracturing and an axial slice showing the distribution of injected fluid in one of the layers of the core. Figure 3.2 shows four possible flow patterns in the fractured region of the sample. To understand the fluid flow behavior and the presence of the fracture tip, the following hypotheses are posed:

1. The presence of the fracture tip accentuates the permeability contrast between the core layers.
2. There is more fluid flow between the layers ahead of the fracture tip in comparison to the region behind the fracture tip.
3. The displaced fluid in the region that contains the fracture is flowed away and diverged from the fracture to the matrix due to combined effects of relative permeability and capillary pressure, for both oil loading and water flooding (Figure 3.2 – d).

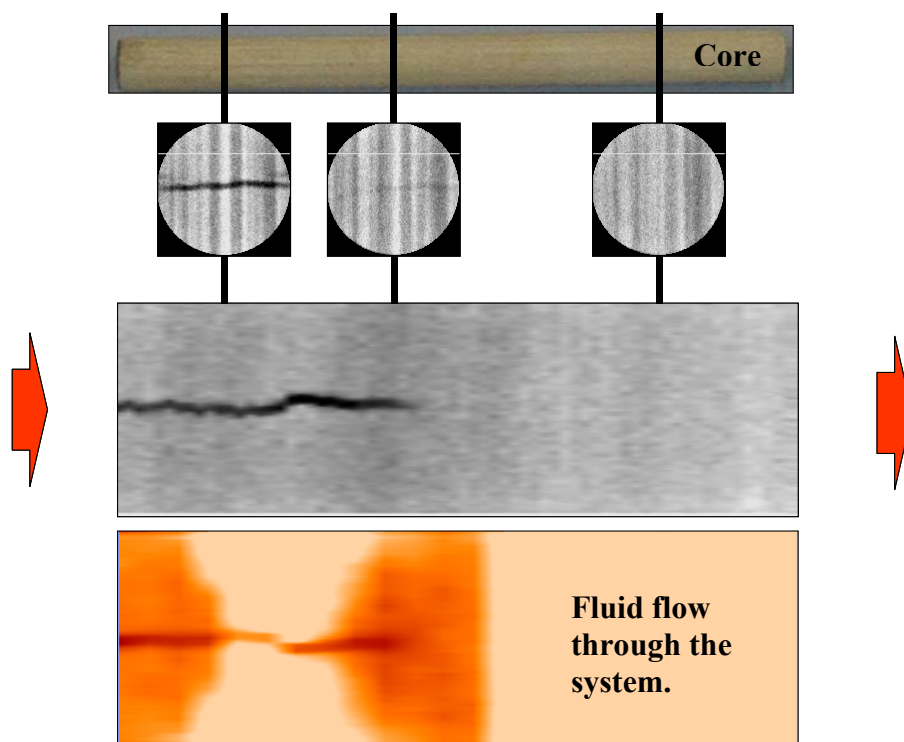


Figure 3.1: Diagram of the matrix-fracture system and the fluid flow behavior.

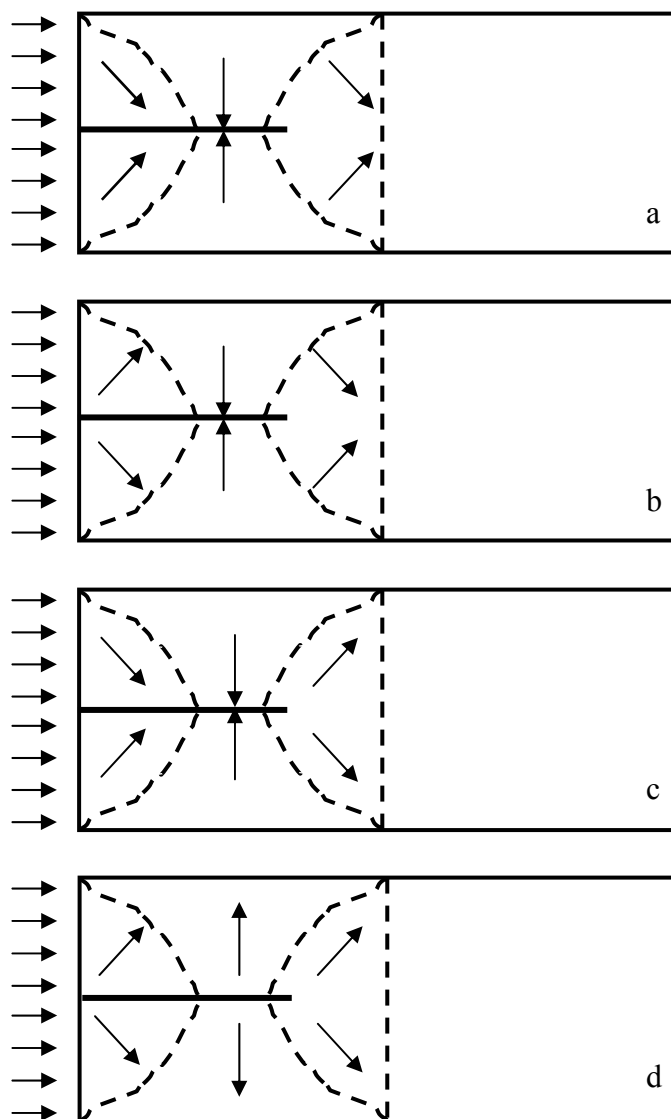


Figure 3.2: Schematic drawing of different fluid flow patterns.

3.2 Objectives

1. Quantify and understand the impact of the fracture tip on accentuating the permeability contrast between the layers.
2. Investigate the inter-layer communication within the sample, before and ahead of fracture tip.
3. Determine the fluid displacement path of the fractured region of the sample.
4. Understand the physical effects of relative permeability and capillary pressure characteristics on displacement process in the presence of a fracture tip.

3.2.1 Approach

The approach to explore the hypotheses was to combine experimental observation and history matching modeling in order to understand the fluid flow mechanisms in the system. The experimental data include 4-D saturation distributions, pressure drops, injection rates, fluid recoveries, CT derived porosity distributions, and correlated absolute permeability.

The modeling process was done in two main stages:

- A. Two-dimensional modeling of one layer.
- B. Three-dimensional modeling of the entire system.

In the first stage, the simulation model was formed, and refined to yield a performance similar to the experimental observations. In the second stage, the entire performance of the experiments was studied using an optimizing history matching technique. Figure 3.3 shows a schematic diagram summarizing the approach.

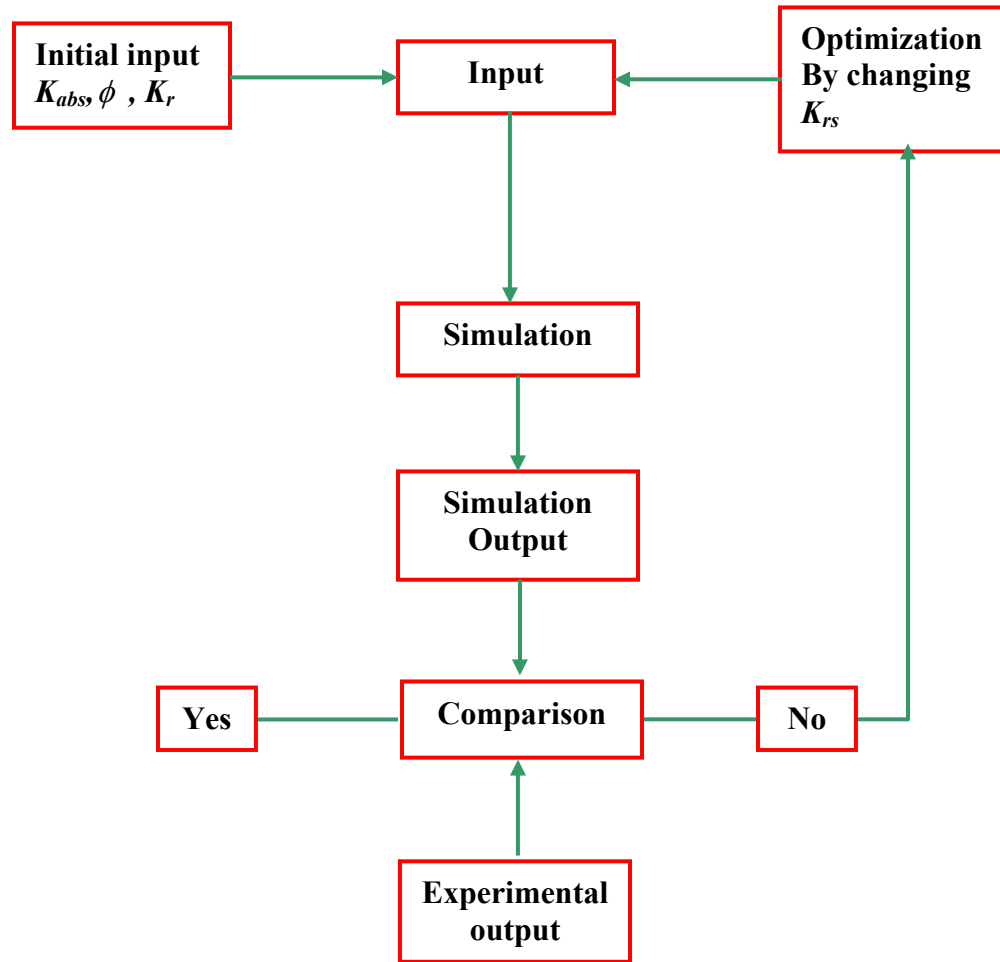


Figure 3.3: Schematic diagram of the approach.

Chapter 4

EXPERIMENTAL DATA

The experimental data that form the basis of the model are presented in this chapter. Two-phase experiments were conducted on layered Berea sandstone cores that were artificially fractured at the ends. The cores were saturated with water, then flooded with oil, and finally flooded with water. Saturation distributions were monitored using x-ray computed tomography (CT).

4.1 Fluids

Two immiscible liquids were used to carry out the experiments. They were distilled water and benzyl alcohol, representing water and oil, respectively. The water was tagged with 7% by weight sodium iodide to give it a high CT signature. The oil had a low CT signature. The CT contrast between the water and the oil permitted the monitoring of displacement processes using one energy setting (120 kV and 125 mA). The two fluids were equilibrated prior to injection into the rock sample. The viscosity, density, and interfacial tension are given by *Al-Wadahi (1994)*.

4.2 Rock Samples

Layered Berea sandstone cores were used. The cores had a diameter of 51 mm and a length of 610 mm. The cores were purchased from Cleveland Quarries. Figure 4.1 illustrates the dry images of one of the cores prior to the fracturing process. The images had a spacing of 25.4 mm. The gray scale color scheme depicts low density as dark

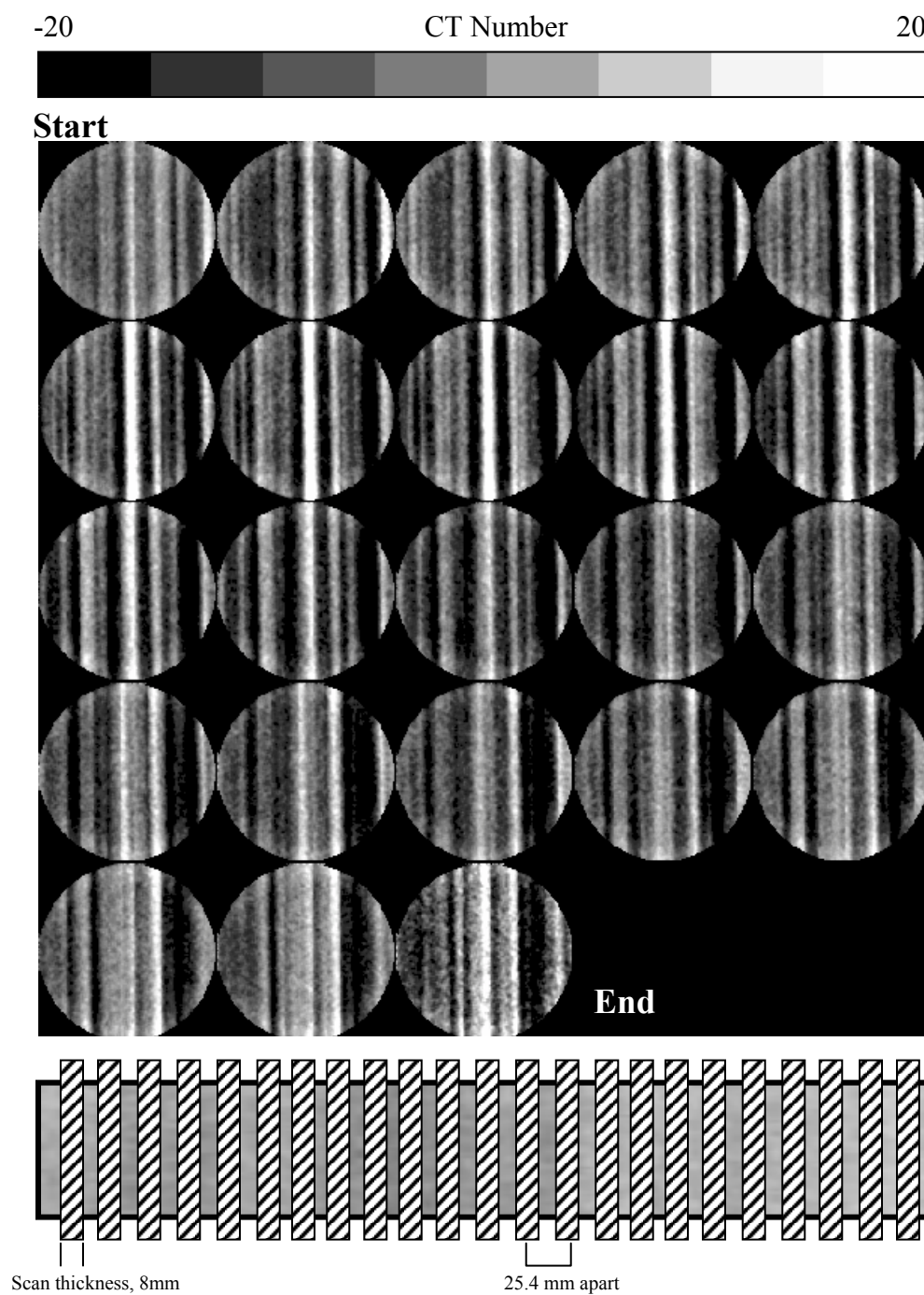


Figure 4.1: Dry images of the core. Schematic drawing showing where the 460 images were acquired along the core.

regions and high density as light regions. The images show the strong layering of the rock.

4.3 Experimental Apparatus

The fluid flow system was built to handle three-phase flow experiments and consisted of injection pumps, a circulation system, a pressure monitoring system, and a fraction collector system. The rock samples were placed in an aluminum core holder and positioned in the scanning domain of the x-ray images. Details of the experimental setup are given by *Alajmi (1999)*.

4.4 Experimental Procedure

The experiments were preformed: a) with the fracture at the inlet end of the core, and b) with the fracture at the outlet end of the core. A modified Brazilian test was used to fracture the sample, Figure 4.2. In this test compression is applied across the diameter of a cylindrical rock sample, splitting the core. The fracture starts at the center, where the tensile stresses are greatest, and then spreads to the outer ends of the sample. Details of these experiments are given *Alajmi (1999)*.

The experimental procedure followed these steps:

- A. Fracture the core, Figure 4.3a, and b.
- B. Load the fracture into the core holder.
- C. Scan the dry sample.
- D. Vacuum saturate the sample.
- E. Scan the wet sample.

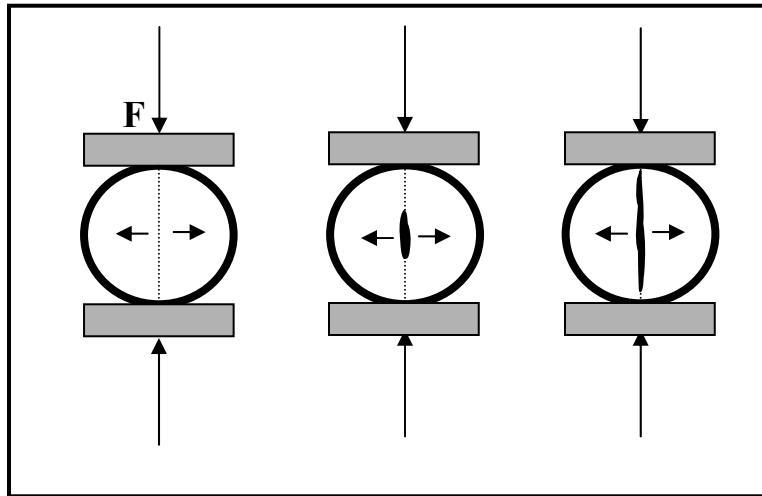


Figure 4.2: Stages of the modified Brazilian Test.

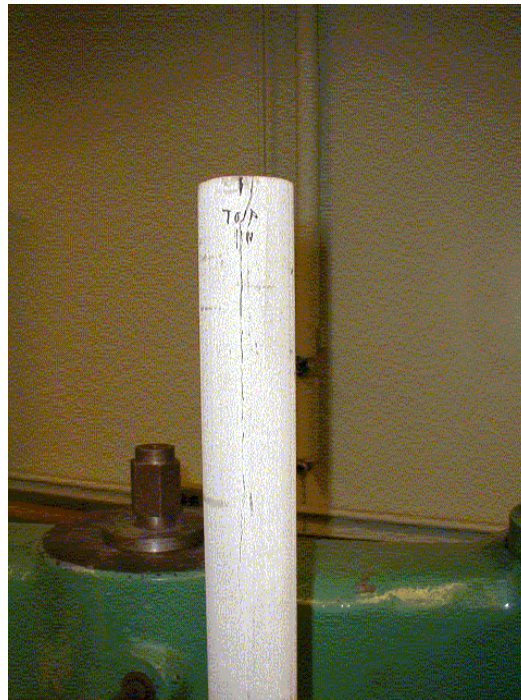
**A****B**

Figure 4.3: Fracture inducement in the laboratory. A: Before fracturing. B: After fracturing.

F. Inject oil into the sample and scan during the injection period.

G. Inject water into the sample and scan during the injection period.

In the first experiment, the fracture was approximately 250 mm long. The dry fracture sample was scanned and the images are shown in Figure 4.4. The fracture is identified as the dark horizontal region in the first eleven slices. The apparent fracture aperture is amplified by the resolution of the scanner and by the color scheme. The core was vacuum-saturated with water. The core pore volume was measured to be 217 cc yielding a porosity of 17.5%, a typical value for Berea Sandstone. In the second experiment, the fracture length at the outlet end was 100 mm with an average porosity of 19%. Figure 4.5 illustrates images of the matrix and the fracture scanned by the industrial scanner at high resolution. The scanning circle did not cover the full diameter of the prior scans. The three big layers are not in the center. The resolution of the images shown in figure 4.5 is about 0.05 mm in all directions.

4.4.1 Porosity

The porosity distribution of the porous medium was determined using the CT images. The porosity distribution in the core is obtained by the following procedure:

1. Obtain dry scans of the core.
2. Obtain water saturated scans of the core at the same position as the dry scans.
3. Subtract the dry scans from the water-saturated scans. The resulting images are the net CT values of the water in the core, Equation 3.1.
4. Compute the average CT value of the net water images from part 3.
5. Compute the average core porosity from external material balance.

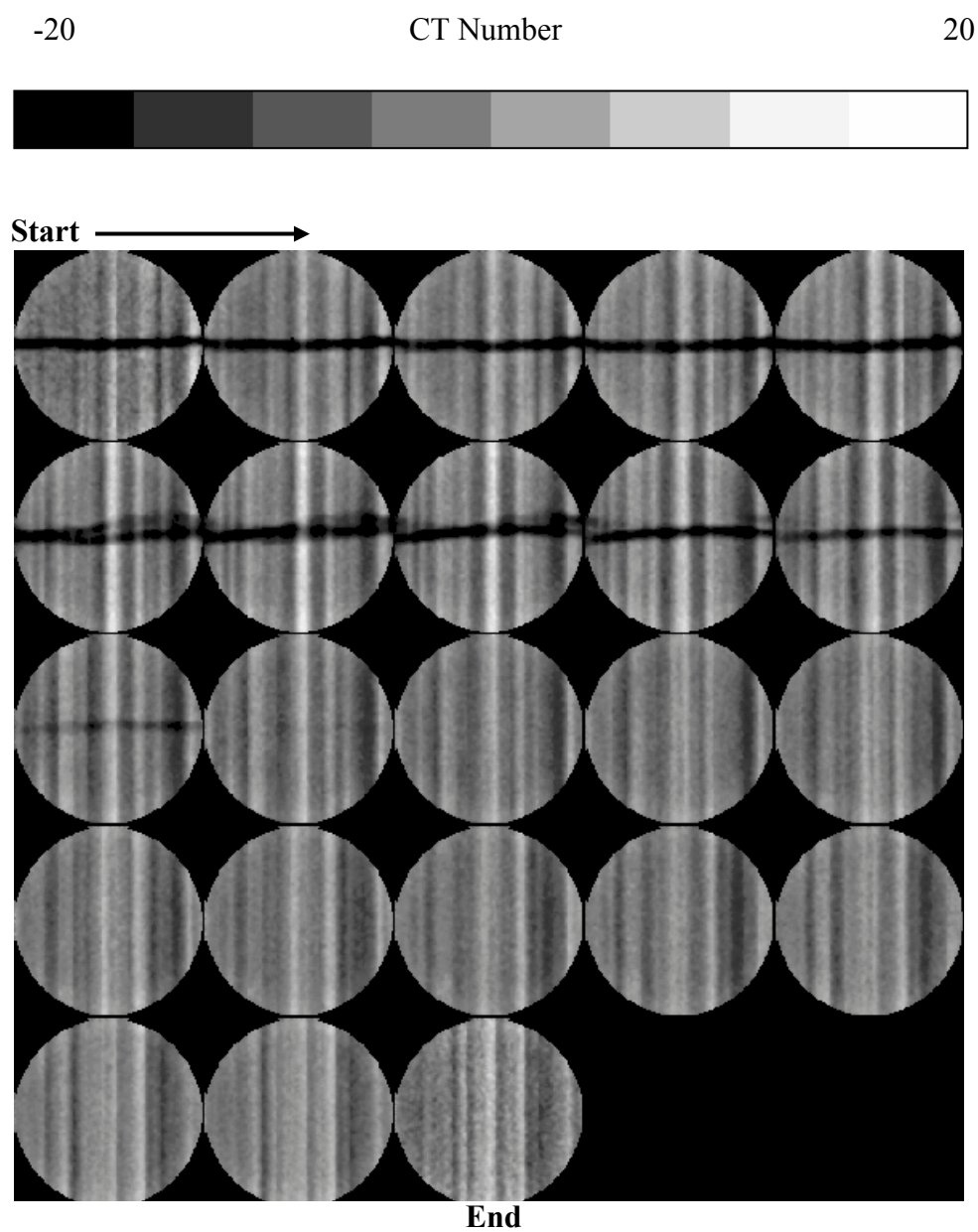


Figure 4.4: Dry images of core after fracture. Same scanning position as Figure 4.1.

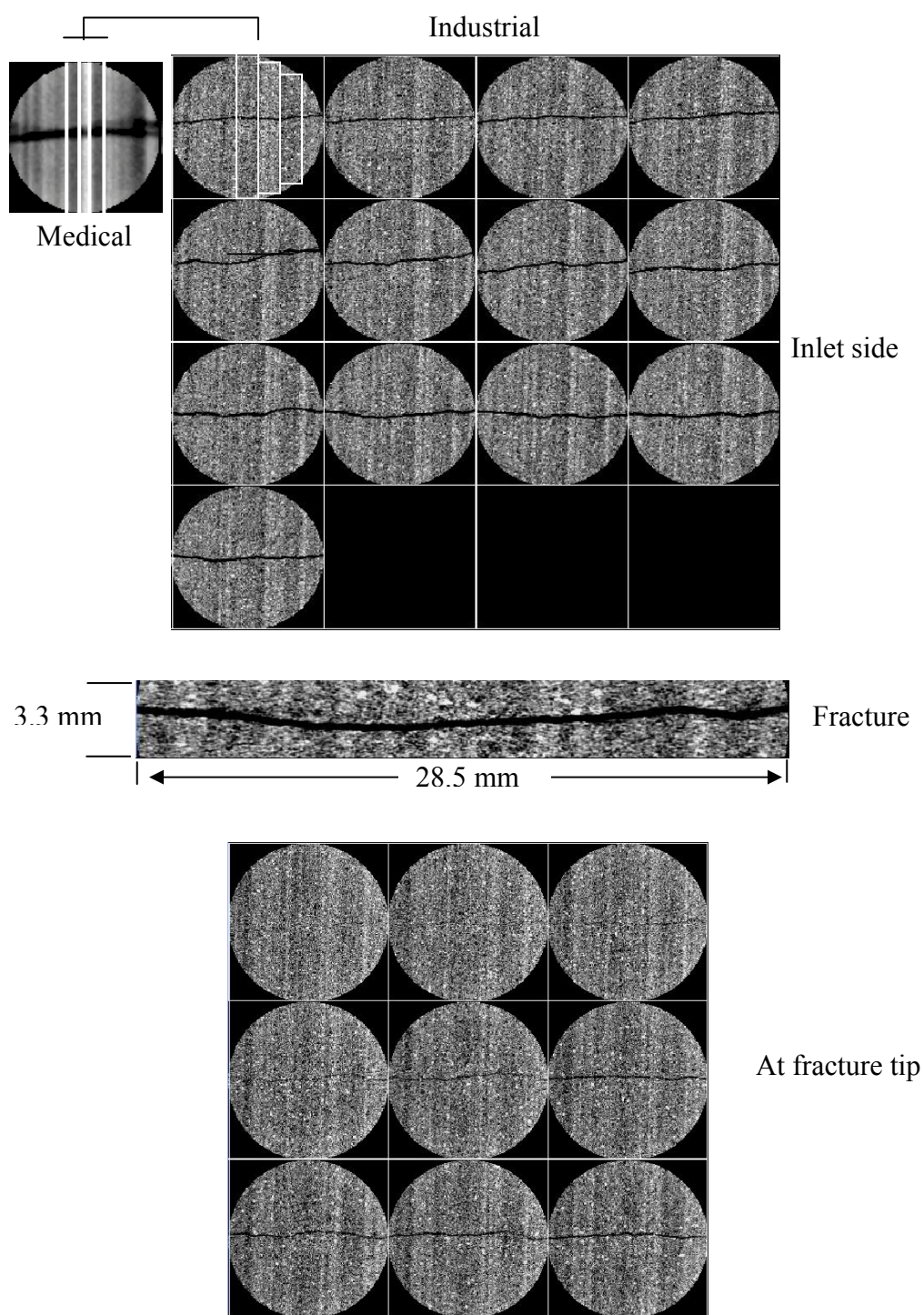


Figure 4.5: Some slices from the high-resolution scanner.

6. The average CT value for the net water images (step 4) corresponds to the average porosity value (step 5) and provides the basis for computing the porosity distribution.
7. Convert the net CT water images to porosity images. In the first experiment, each net water CT pixel value was multiplied by (17.5%/155.8) to obtain the porosity distribution, equation 3.2. In the second experiment the porosity conversion factor was multiplied by (19% / 51.2).

$$\overline{CT}_{wet} - \overline{CT}_{dry} = \Delta \overline{CT}_{w-d} \quad (3.1)$$

$$\Phi^{\#} = \frac{CT_{wet}^{\#} - CT_{dry}^{\#}}{\Delta \overline{CT}_{w-d}} \Phi_{mb} \quad (3.2)$$

where \overline{CT}_{wet} is the average CT number of the wet scans and \overline{CT}_{dry} is the average CT number of the dry scans of the core.

Figure 4.6 shows two porosity images with their profiles. The image was located 127 mm from the injection end of the core at the center of the fracture. Image A shows a profile that is taken across the layers, 4.0 mm above the fracture. The profile shows the average porosity of the layers. The average porosity of the middle layer is 15.5% while the adjacent two layers show an average porosity of 19%. Image B shows a profile along one of the middle layers. The fracture aperture is not as large as it appears due to the low resolution of the CT scanner used.

Figure 4.7 shows the dry and porosity maps of the two experiments. Figure 4.8 shows five rectangular regions 6.2 mm by 30.8 mm (16 X 80 pixels) inside three images along

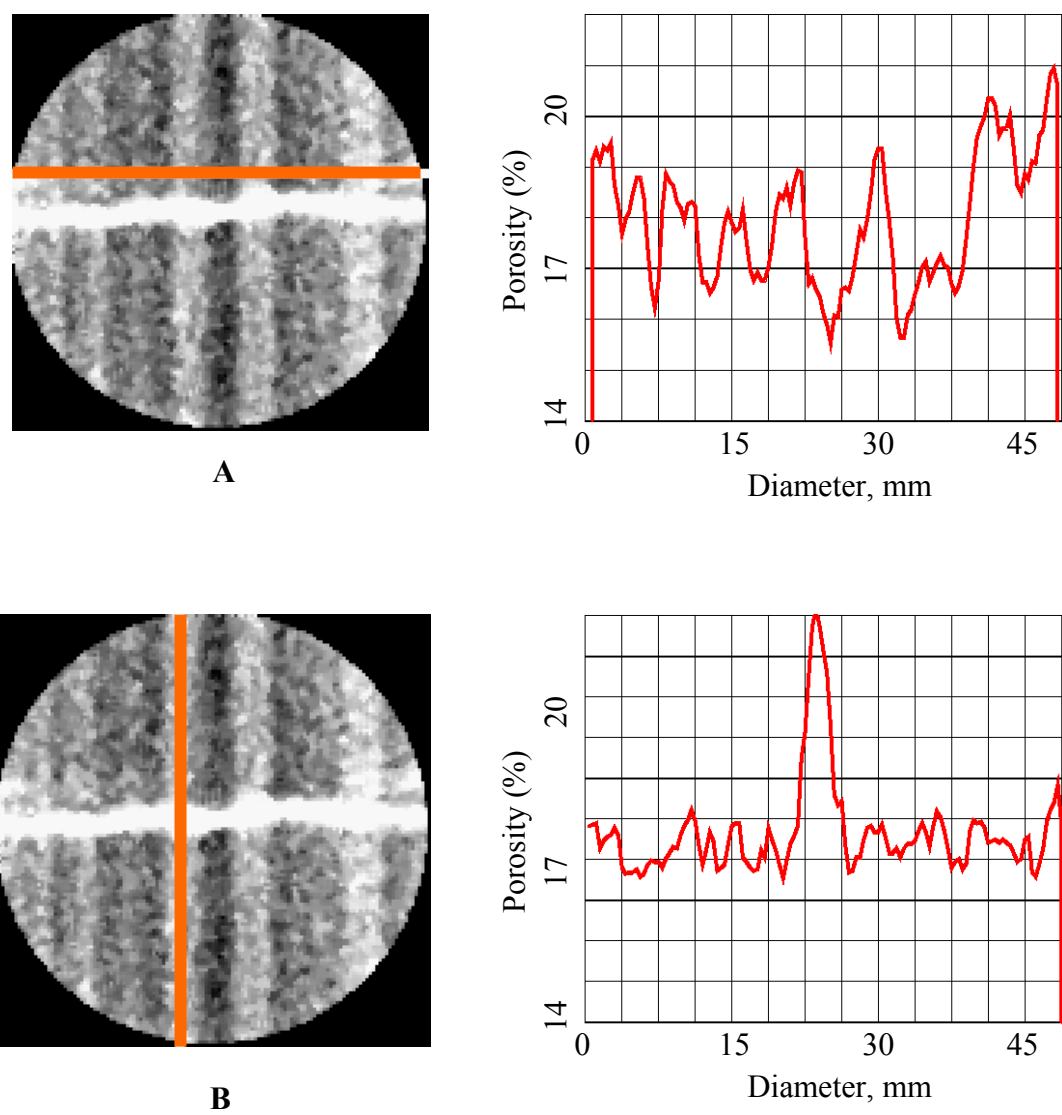


Figure 4.6: A) Average porosity profile across the core layers.
B) Porosity profile along one layer.

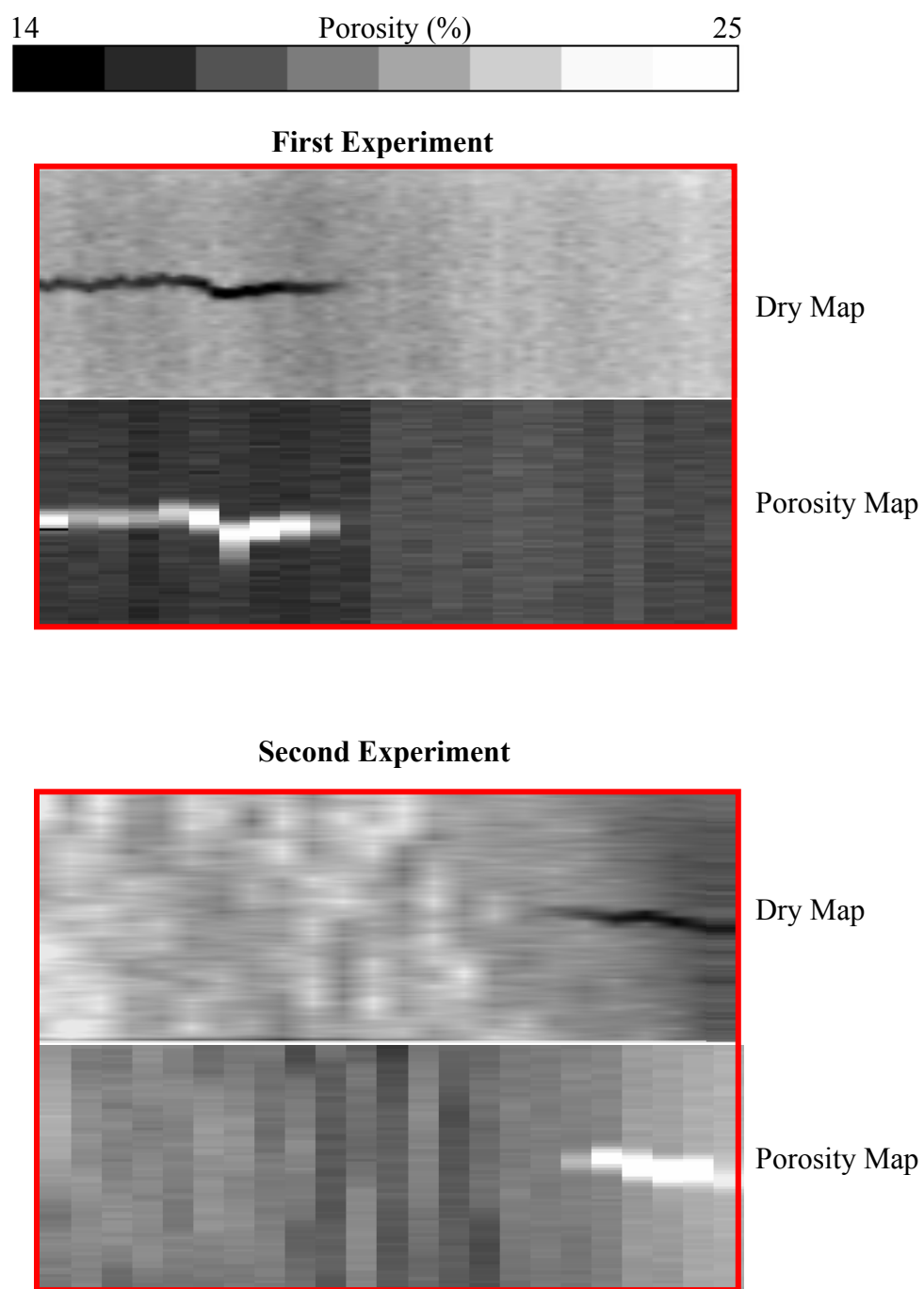


Figure 4.7: Axial slices of the two experiments showing the dry and porosity maps of each experiment.

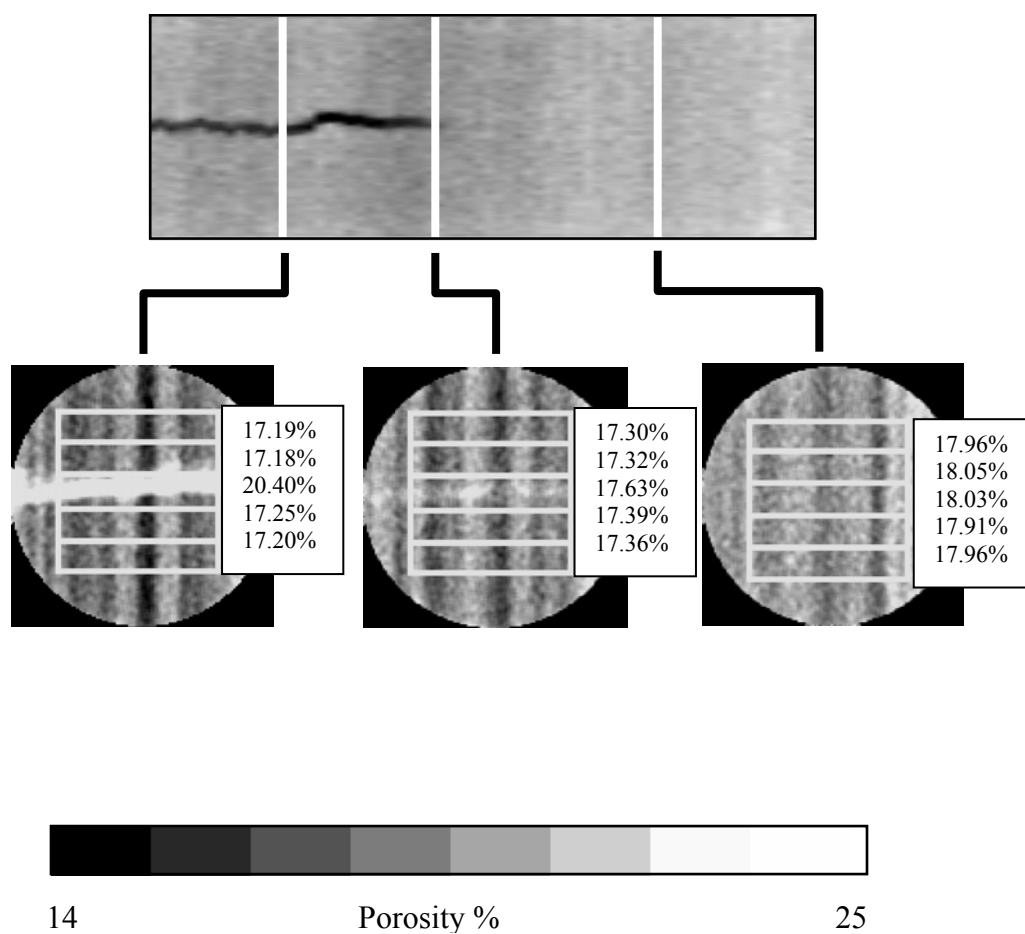


Figure 4.8: Dry reconstruction with porosity images in three locations along the core.

the core. The average porosity in each rectangle was computed and is indicated to the right of the image. The four rectangles that do not contain the fracture have almost identical porosity values. Hence, it can be concluded that prior to fracturing the sample, the middle rectangle had the same porosity as the other four rectangles (on the scale of the rectangles, the system was homogeneous). The variation of average porosity along the core is typical of Berea Sandstone. Using material balance, one can calculate a correlation between fracture width and the porosity in the fracture. The method for developing the correlation was presented by *Grader et al. (2000)*.

4.4.2 Absolute permeability

The absolute permeability was measured in the laboratory by flowing three different flow rates, 1.0 cc/min, 1.5 cc/min, and 2.0 cc/min. The differential pressure was recorded for each flow rate. Estimation of the permeability of the non-fractured region can be obtained by neglecting the region that contains the fracture, Figure 4.9. The normalized permeability estimation for the first experiment was about 64.0 md and for the second experiment 76.0 md. The absolute permeability of the matrix is one of the inputs to the model. Several porosity-permeability correlations were tested to describe the matrix absolute permeability. Timur's correlation was successful in matching the average absolute permeability that was measured in the laboratory, given by Equation:

$$k_{cor} = 0.136 \frac{\phi^{4.4}}{S_{iw}^2} \quad (3.3)$$

where S_{iw} is the irreducible water saturation to each layers. Figure 4.10 shows a porosity image that was divided into 15 layers. Table 4.1 shows the porosity of each layer

Layers

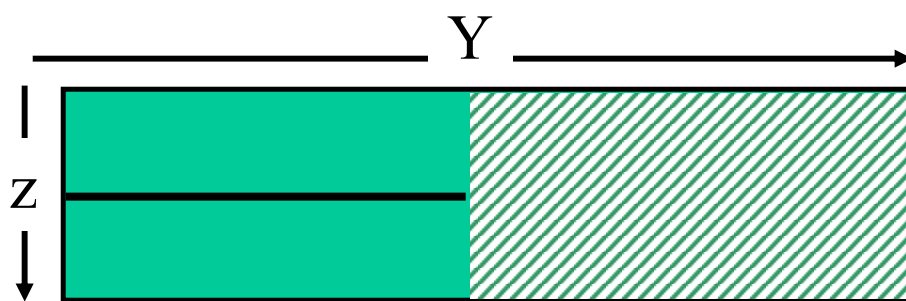
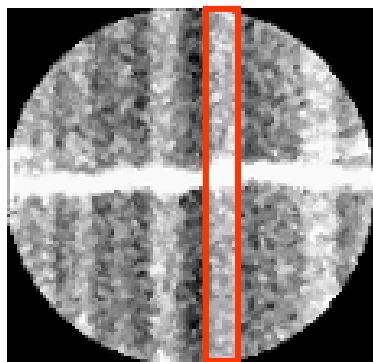


Figure 4.9: Schematic Reconstruction of the region of major pressure drop.

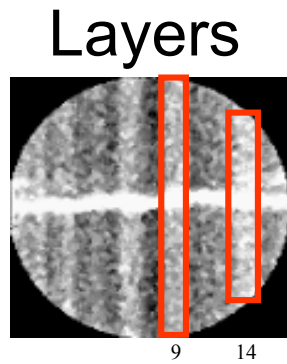


Figure 4. 10: Porosity images with the 15 layers.

Layer	por	k	Thickness
#	%	md	mm
1	18	50.41	3.40
2	19	63.95	3.68
3	18	50.41	2.27
4	17	39.20	3.12
5	17	39.20	3.68
6	19	63.95	1.13
7	17	39.20	3.40
8	20	80.14	4.53
9	15	22.60	4.53
10	20	80.14	4.53
11	16	30.02	2.55
12	17	39.20	2.55
13	18	50.41	3.68
14	21	99.33	5.67
15	18	50.41	5.67

Table 4.1: Average porosity and correlated absolute permeability of layers.

obtained from the CT data, and the correlating absolute permeability calculated using Equation 3.3. Two layers were highlighted (9 and 14).

The average absolute permeability of the sample was calculated using Equation 3.4, which is based on parallel fluid flow in the porous medium. The non-fractured area of the core was considered for the pressure drop since the pressure drop in the fractured region was very small.

$$\overline{k_{abs}} = \frac{\sum_{j=1}^n k_j A_j}{\sum_{j=1}^n A_j} \quad (3.4)$$

where k_j is the average absolute permeability for each layer as shown in Table 4.1, A_j is the area of the layer, and $\overline{k_{abs}}$ is the average absolute permeability. The average absolute permeability calculated was 62 md and the lab measurement was 64 md. Figure 4.11 shows cross-sections of the average porosity and permeability of the layers. Small variations in porosity amplify the variations in permeability.

4.4.3 Oil Injection

The water-saturated core was flooded with oil. Several CT scans were taken at different pore volumes to capture the oil flow as it moved in the fracture, and then diverged into the matrix from its tip. As the oil moved away from the fracture tip, a vertical saturation front formed. The oil injection was stopped after injecting 20 PV, which gave an overall oil saturation of 68% (first experiment). Figures 4.12 and 4.13 present axial maps of oil saturation in one of the high permeability layers that were constructed at various values of pore volumes of

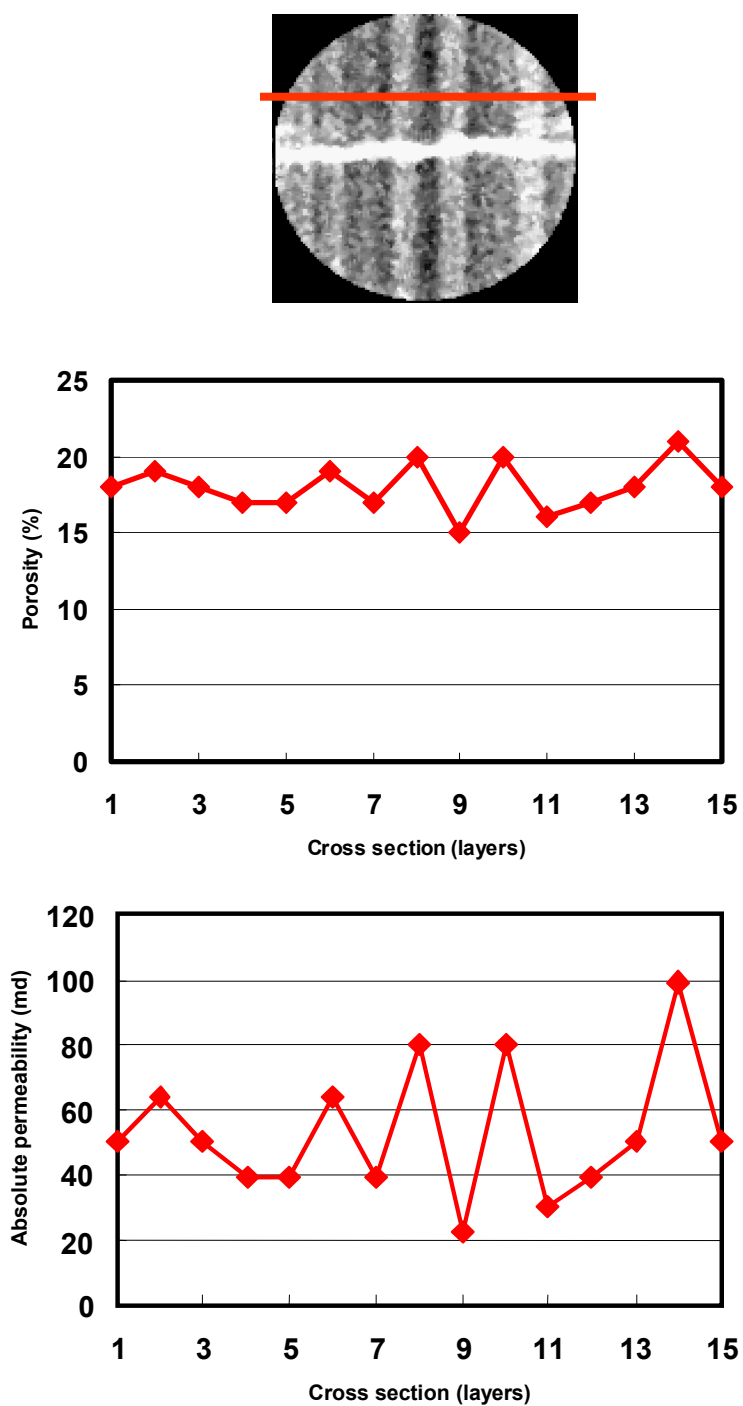


Figure 4.11: Porosity and absolute permeability as a function of layer position.

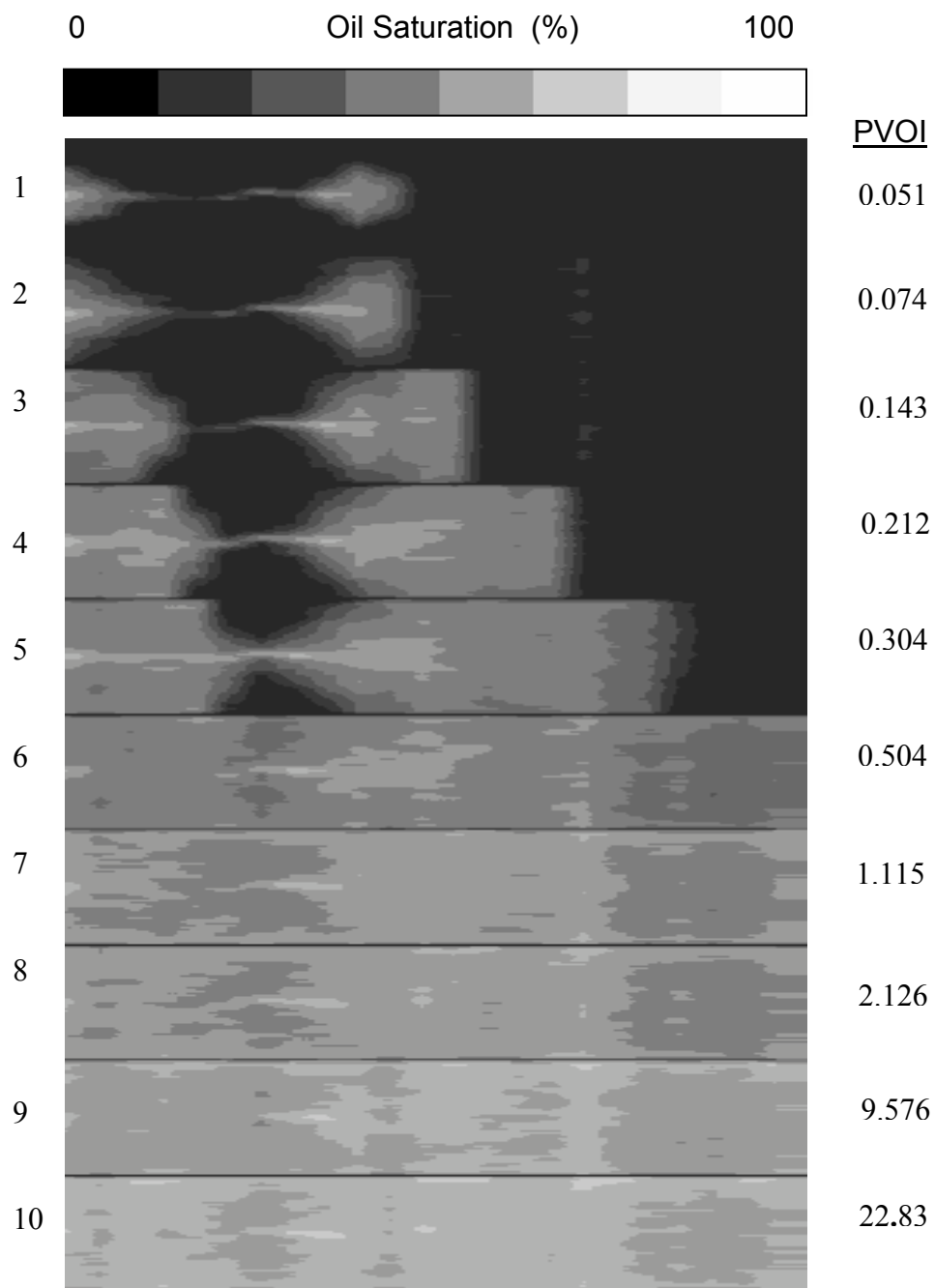


Figure 4.12: Oil saturation at different oil pore volume injected.

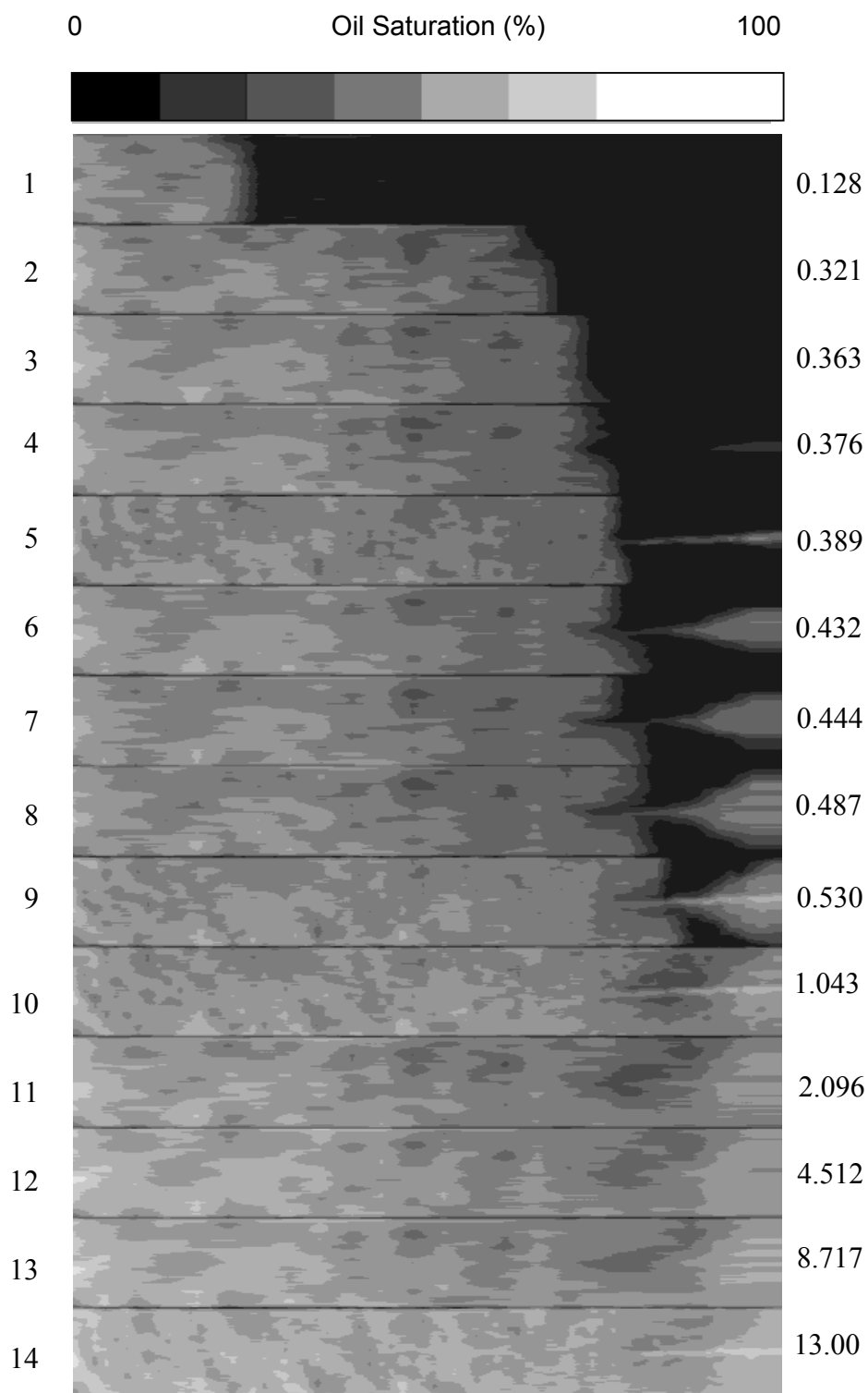


Figure 4.13: Axial oil saturation maps of the second experiment at different pore volume injected.

oil injected for the first and the second experiments, respectively. The conversion of CT numbers to saturation values was done using a linear correlation that was based upon the average CT number for the core and the corresponding average saturation in the core for wet condition ($S_w=100\%$), and after the benzyl alcohol flood ($S_w=32\%$), summarized by Equations 3.5 and 3.5.

$$\overline{CT}_{wet} - \overline{CT}_{oil} = \Delta \overline{CT}_{w-o} \quad (3.5)$$

$$S_o^{\#} = \frac{CT_{wet}^{\#} - CT_{oil}^{\#}}{\Delta \overline{CT}_{w-o}} \frac{\overline{\phi}_{mb}}{\overline{\phi}^{\#}} \overline{S}_{o_{mb}} \quad (3.6)$$

These axial maps present the net oil in the core. Each stage of injection was subtracted from the 100% water saturated condition. Since the fracture had a very high permeability, it captured most of the injected oil at early time, as shown by the first reconstruction at 0.051 POVI. The oil then was transported through the fracture to the downstream tip of the fracture displacing water. At the downstream tip, the oil started to diverge out from the fracture to the matrix. When the oil diverged, it formed a sharp front which moved along the core until oil breakthrough. The sharp front is clearly seen in reconstructions 3, 4, and 5. At 250 mm, the tip of the fracture was identified by the sudden change in saturation values, the location where the fluid started to diverge. At the end of the oil flood, the oil saturation was 68% and the water residual saturation was 32%.

The movement of the oil front away from the fracture was not as fast as the movement of the oil in the fracture due to the high permeability of the fracture. The differences in velocity forced the oil in the fracture to by-pass the middle regions around the fracture. Figure 4.14 shows two plates of images where the oil advances in the high

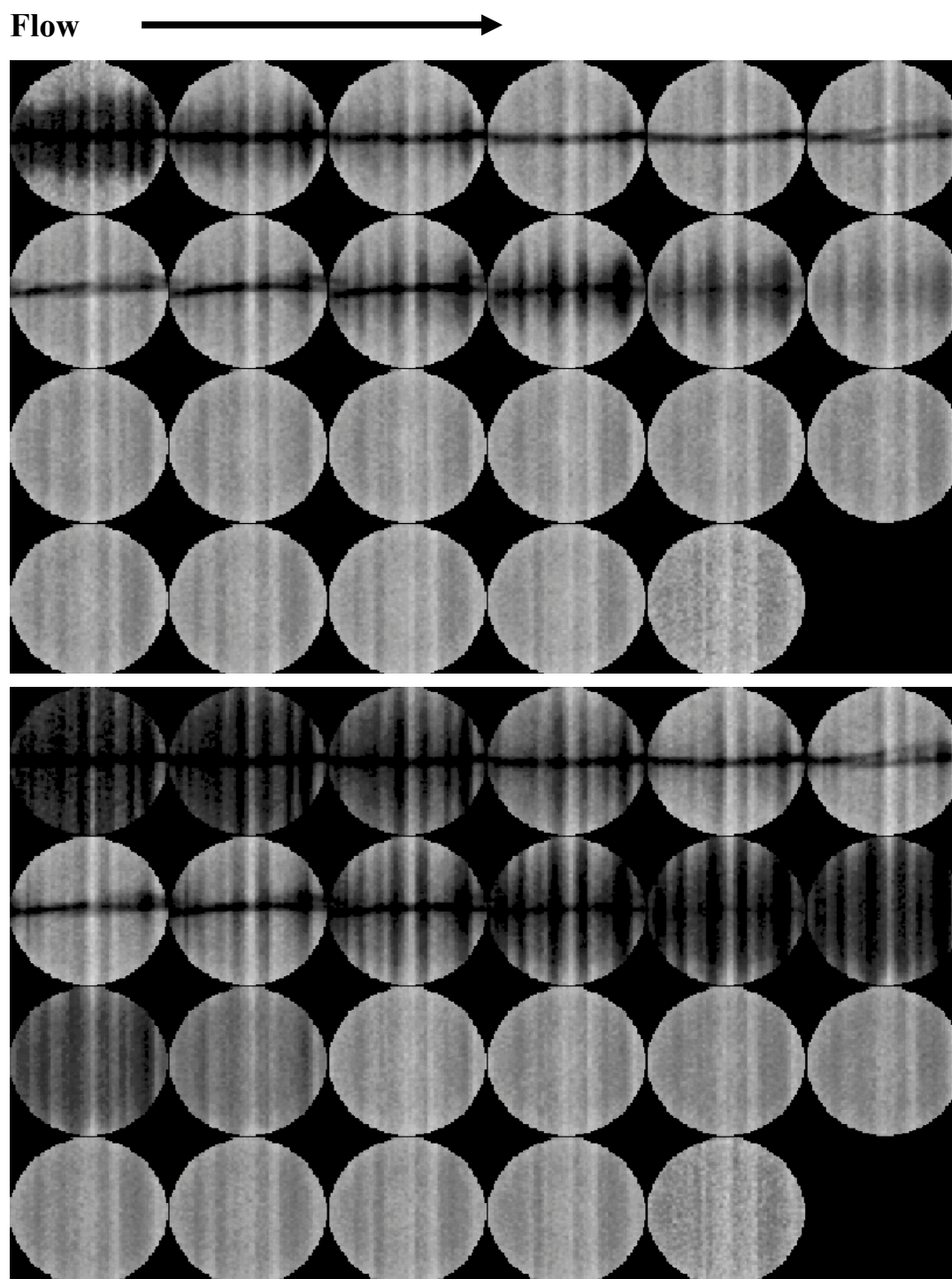


Figure 4.14: Two plates of images at two stages of the oil injection process.
Top: at 0.051 PVOI. Bottom: at 0.143 PVOI.

permeability and porosity layers more than other layers. At later time, as more oil was injected, most of the by-passed water was displaced.

4.4.4 Oil Flood Flow Patterns Caused by Permeability and Porosity Variations

The high permeability/porosity layers were flooded first in the core. Figure 4.15 presents a vertical axial slice of the core and three locations of interest to study the displacement process in individual layers in the presence of the fracture. Three images are shown above the axial slice denoting locations A, B, and C. A horizontal profile line is highlighted in each image, 14 mm (36 pixels) away from the center of the core.

Fracture Region (A): When the core was flooded with oil, the fractured region was bypassed at early time since most of the injected oil was captured by the fracture. Figure 4.16 presents oil saturation profiles as a function of pore volumes of oil injected. The profiles were taken 14 mm above the fracture of an image located at position A in Figure 4.15 (200 mm from the injection end of the core). The profiles illustrate a strongly layered system. The middle layer has lower oil saturation than the two adjacent layers. The high permeability/porosity layers were saturated with oil faster than the low permeability layers. At late time, the low permeability/porosity layers were displaced by oil. It appears that the residual water saturation in the low porosity layers is higher than in the high porosity layers. Can this observation be quantified for this particular lithology? The various saturation profiles are not equally spaced. Can the variable dynamic response be related to permeability contrast, relative permeabilities, and capillary pressures?

Fracture Tip (B): The oil that reached the tip of the fracture early was forced to diverge into the matrix. Figure 4.17 presents oil saturation profiles as a function of pore volumes

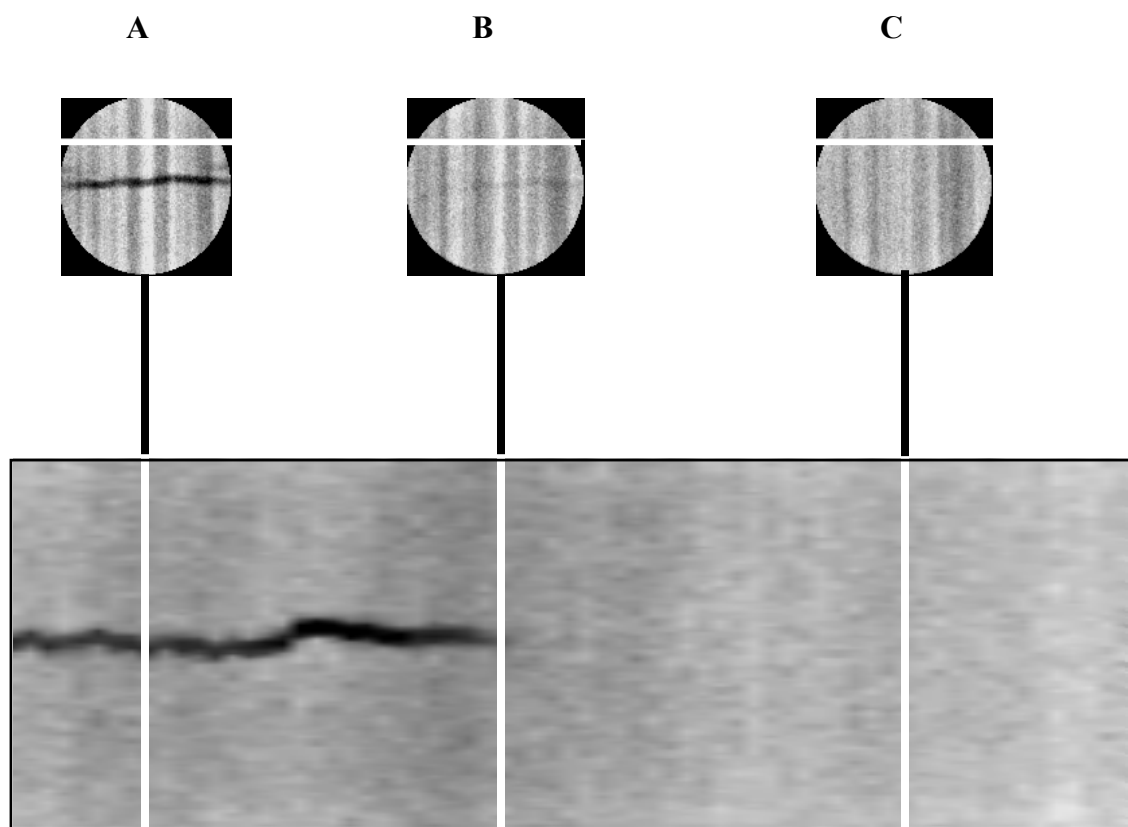


Figure 4.15: Axial slice of the dry core showing the three investigated areas.

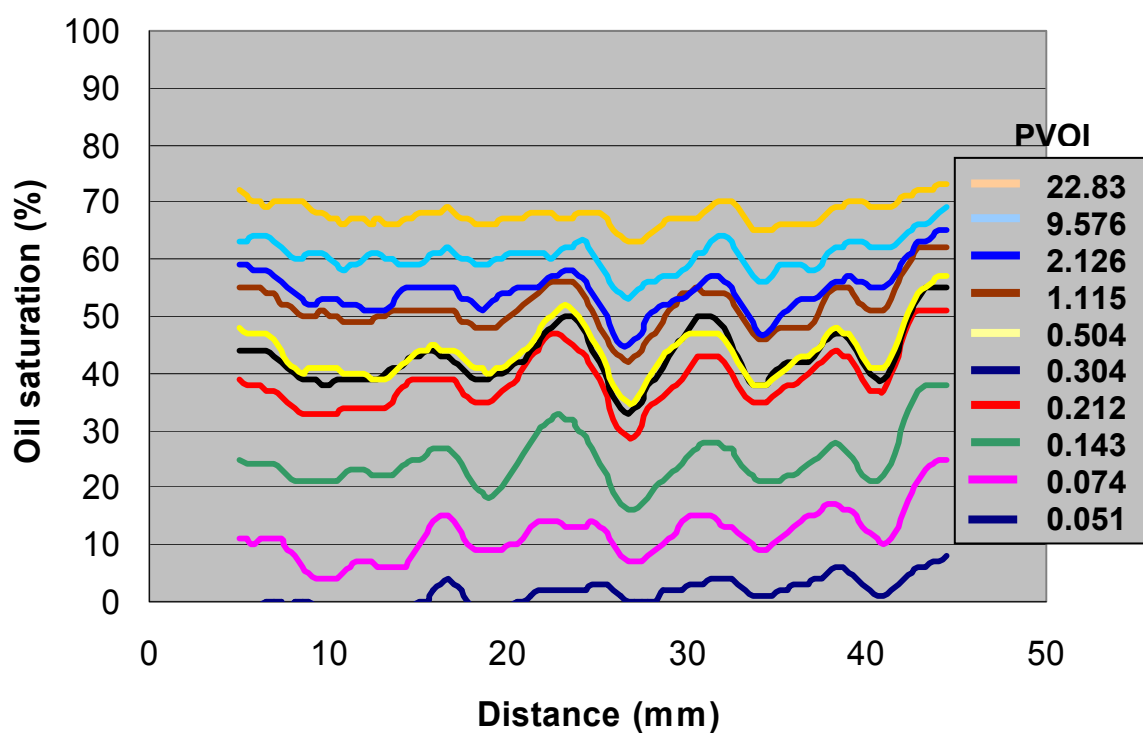


Figure 4.16: Oil saturation profiles at inlet side of core, position A in Figure 4.15.

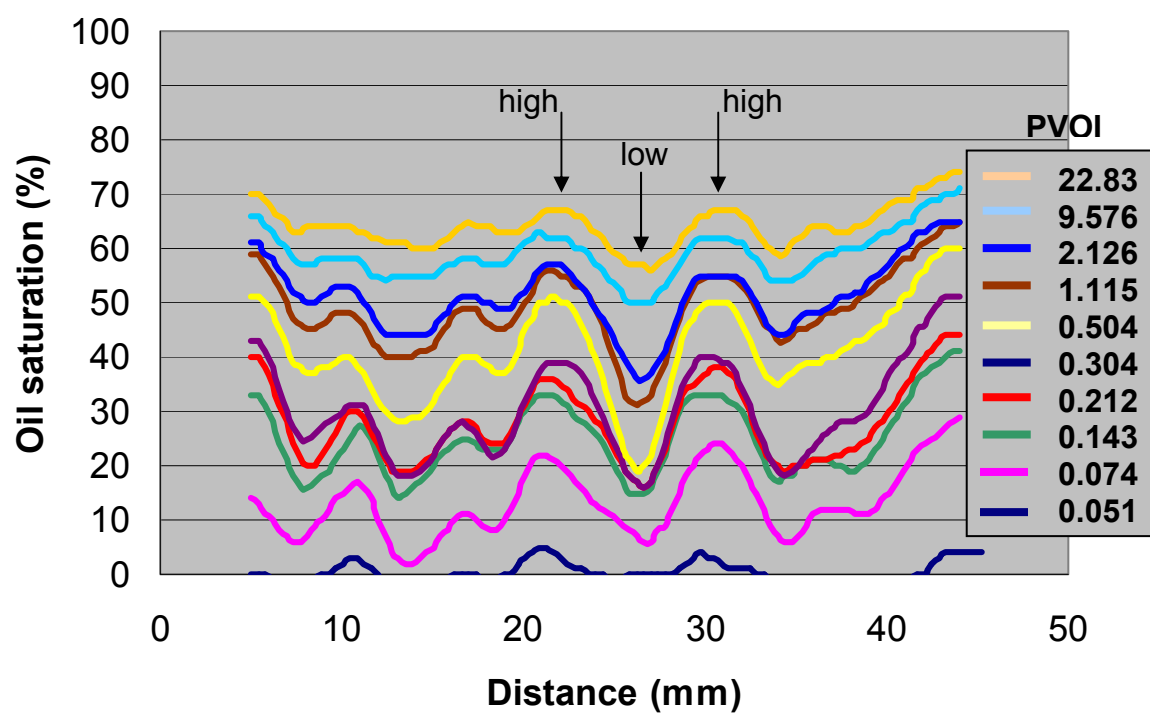


Figure 4.17: Oil saturation profiles at fracture tip, position B in Figure 4.14.

of oil injected. The profiles were taken 14 mm above the fracture of an image located at position B in Figure 4.15 (254 mm from the injection end of the core). The profiles illustrate that at the tip of the fracture the oil saturation increased rapidly at early times, in comparison with position A. Figure 4.18 illustrates the oil saturation stages as a function of pore volume of oil injected (PVOI) in the two high and low k and ϕ layers. It shows that at early time the saturations are close to each other since the oil filled the fracture adjacent to both layers. Then, the high k and ϕ layers were preferentially flooded. At late time, all layers reached a steady difference of residual oil saturation.

Non-Fractured Region(C): In the region that was not fractured, the contrast of the oil saturation values between the layers was small. Figure 4.19 presents oil saturation profiles as a function of pore volumes of oil injected. The profile was taken 14 mm above the center of the core of an image located at position C in Figure 4.15 (460 mm from the injection end of the core). The profiles increase in a similar fashion over the entire width of the sample. For example, between 2.16 and 22.83 PVI, the oil saturation increased by about 10%. The saturation spacing between the two profiles is almost constant, indicating a different flow pattern than in positions A and B. The profiles illustrate that the sample is flooded mainly in the longitudinal or axial direction.

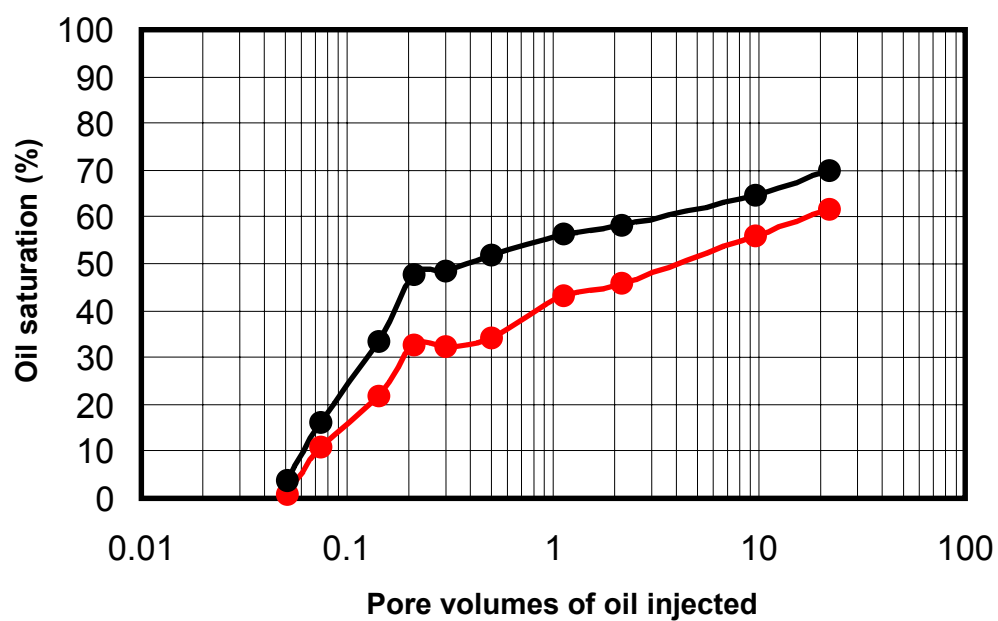


Figure 4.18: Average oil saturation as a function of pore volumes of oil injected.

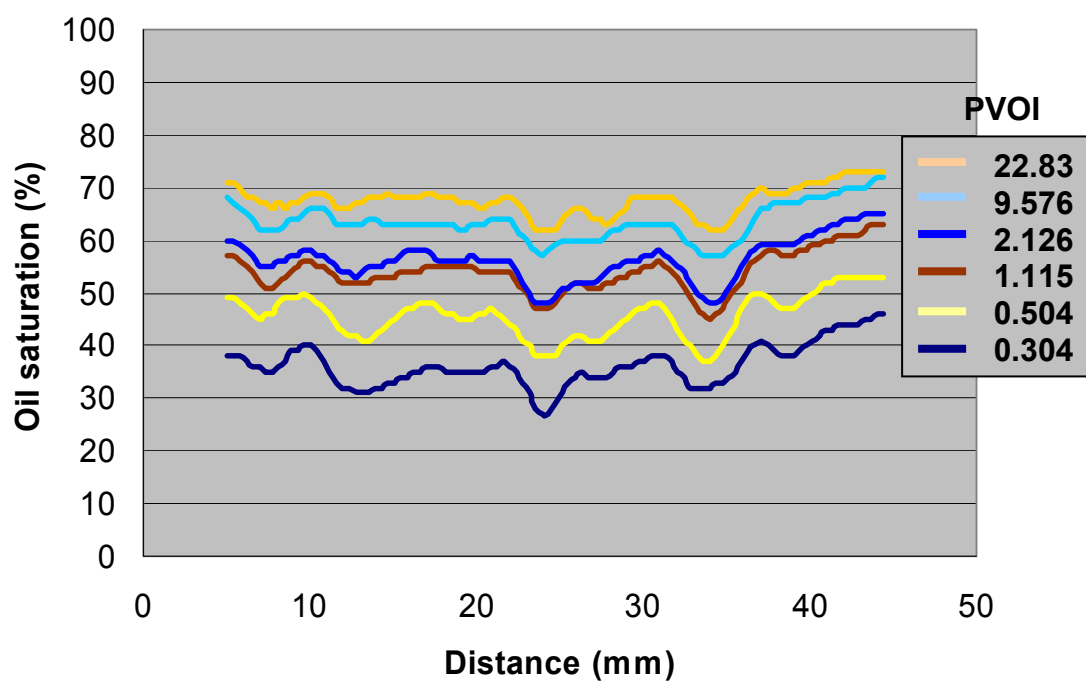


Figure 4.19: Oil saturation profiles at away from the fracture tip, position C in Figure 4.14.

4.4.5 Water Injection

At the end of the oil flood the water saturation was 32% in the first experiment. Various pore volumes of water were injected and the sample was scanned after each stage of injection. Figure 4.20 shows axial slices of a high permeability and porosity layer at different values of pore volumes of water injected. Figure 4.21 shows profiles of water saturation across the layers at the tip of the fracture. Figure 4.22 shows profiles of water saturation across the layers ahead of the fracture tip. These two figures show that the layers were flooded at the same rate. This contrasts with the oil flood where the high permeability /porosity layers were flooded much faster than the low permeability/porosity ones. The factors influenced the water flood are the viscosity difference and capillary forces. The viscosity ratio was 1:5 during water flood while it was 5:1 during the oil flood. After injecting 1.2 pore volumes of water, the average oil saturation in the core was reduced from 68% to 32.0%. More details of the experimental setup are given by *Alajmi (1999)*. Figure 4.23 shows water saturation maps of the second experiment. An axial slice was taken in the middle of core illustrating the development of the water flood at different values of pore volumes injected.

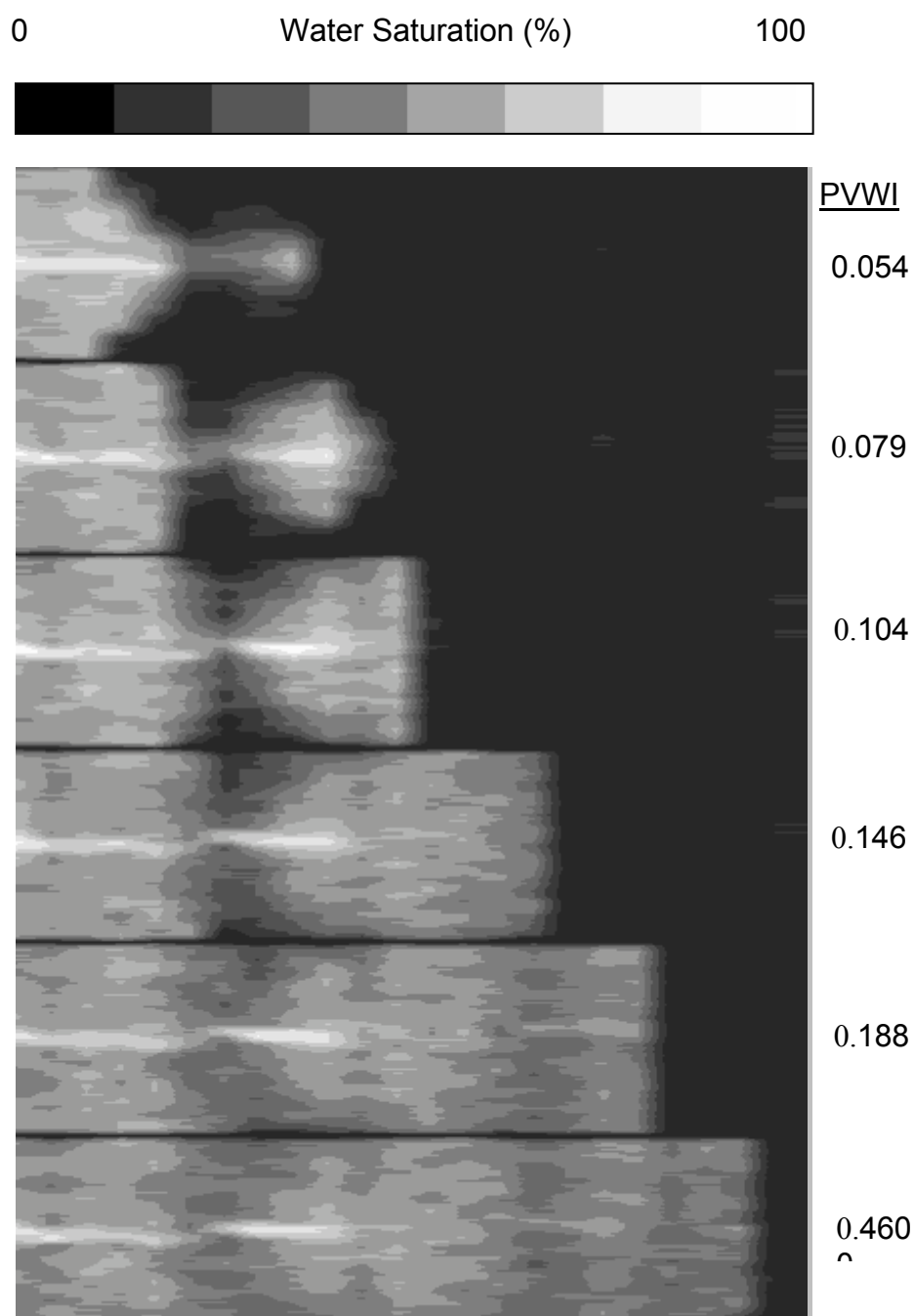


Figure 4.20: Axial slices during the water flood at different values of pore volumes injected, prior to breakthrough.

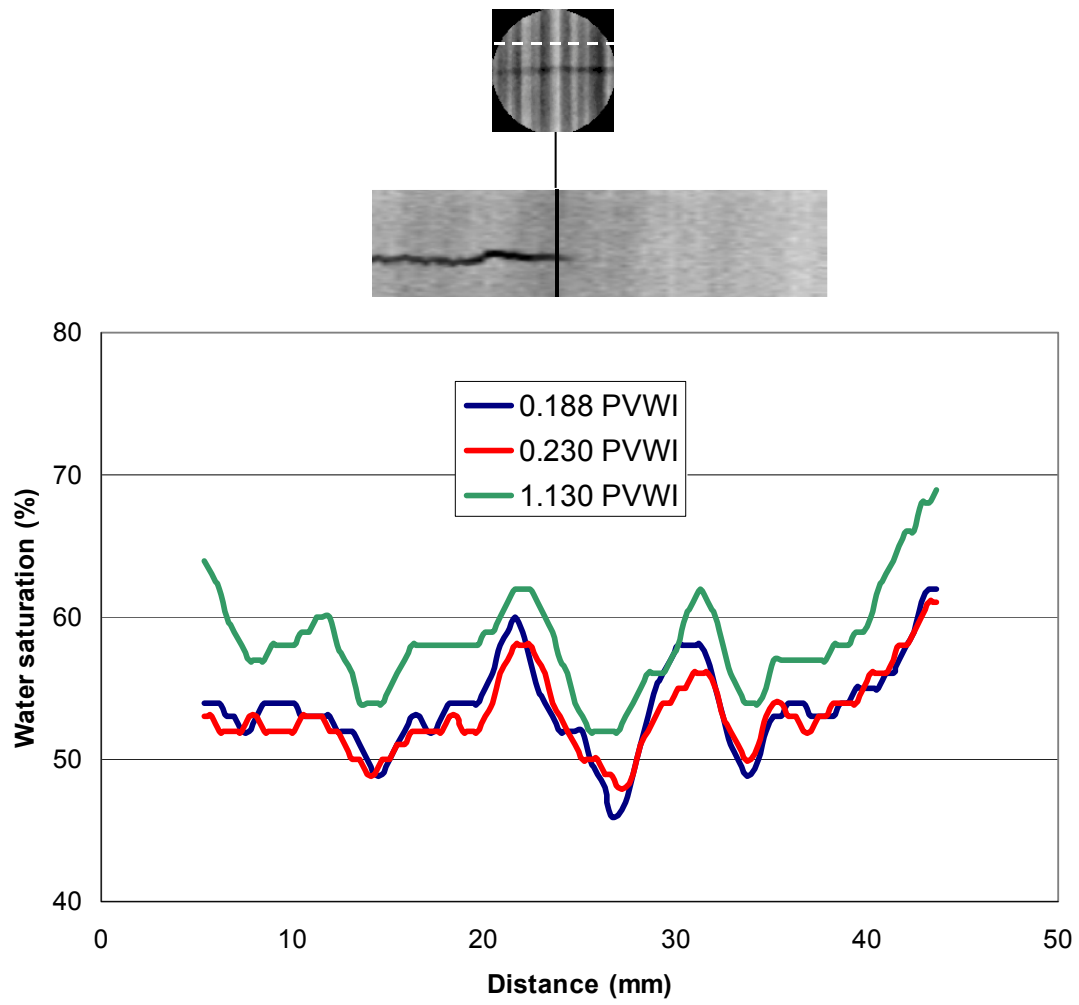


Figure 4.21: Water saturation profiles across the layers at the fracture tip.

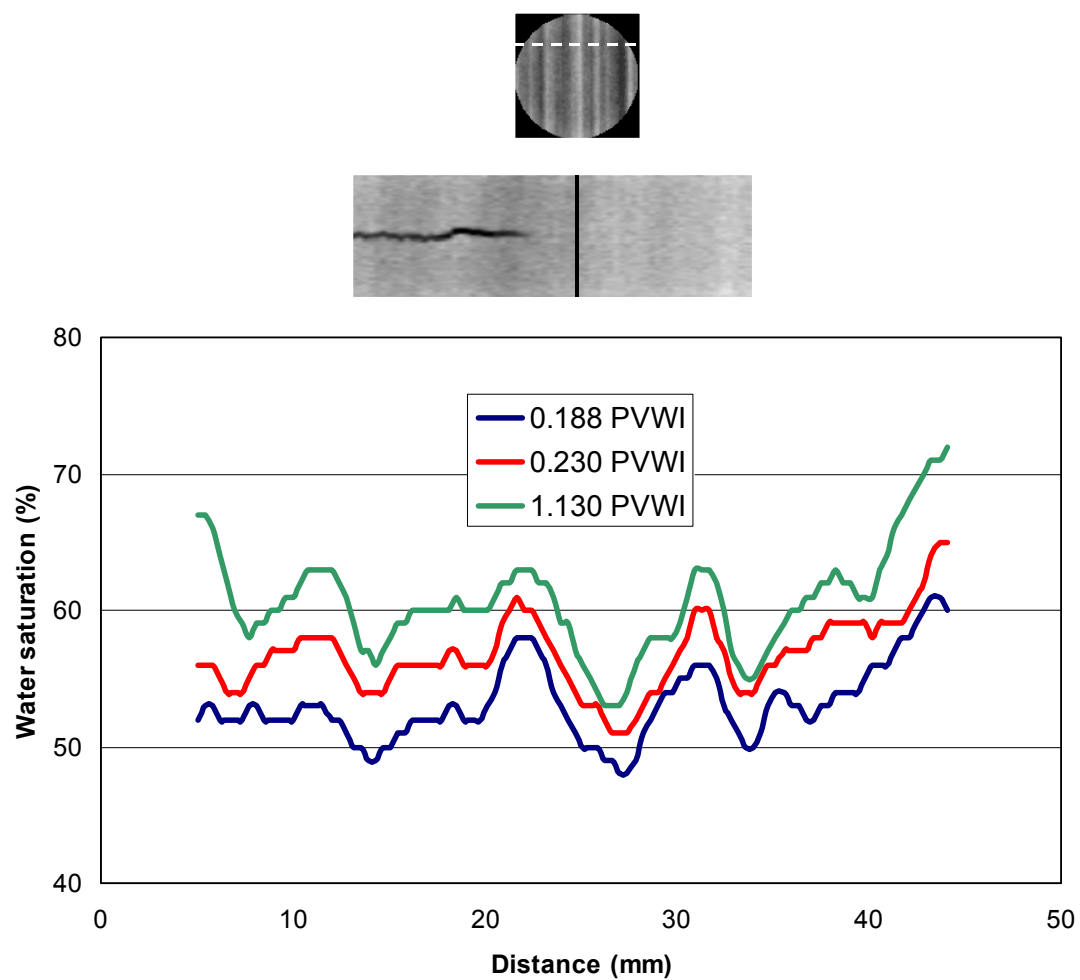


Figure 4.22: Water saturation profiles across layers away from the fracture tip.

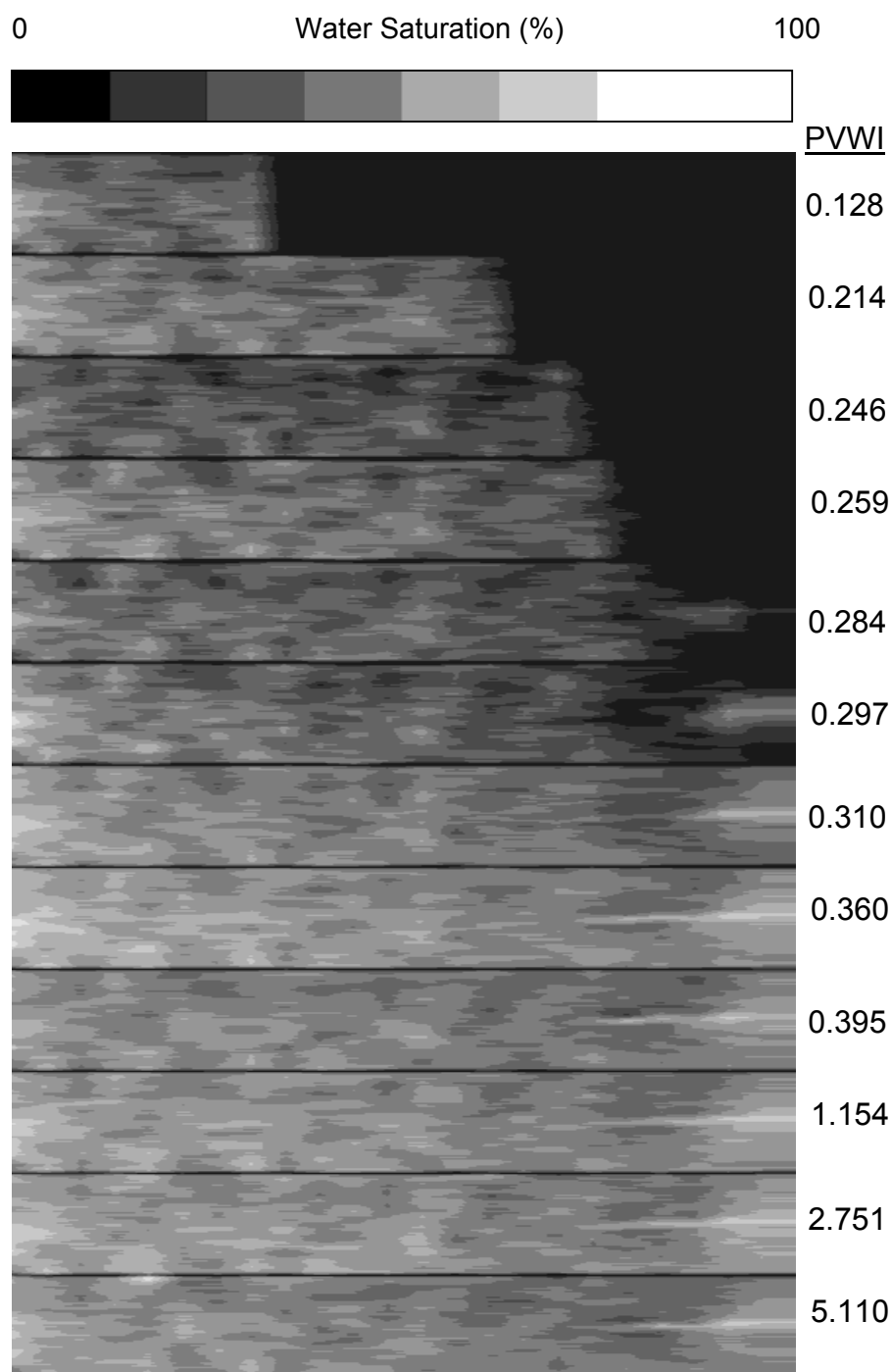


Figure 4.23: Axial slice of water flood at different pore volume injected for the second experiment.

Chapter 5

MODELING

5.1 Introduction

The main goal of modeling the experimental data presented in this research is to prove the hypotheses mentioned in Chapter 3. This work will also determine the influence of the fracture tip on multi-phase flow, how it accentuates the permeability contrast between the layers, and to study the transport properties of heterogeneous fractured rocks, and the relative efficiencies of recovery processes. The modeling structure consists of a three-dimensional numerical simulator and a history matching technique to simulate the existing experimental data. The chapter consists of the following three stages:

- a. Two-dimensional construction of a model of a single layer with a fracture.
- b. Constructions of a three-dimensional model of the entire experimental system.
- c. Investigation of the influence of the fracture tip on the displacement processes.

The three-dimensional numerical simulator used is ECLIPSE100[®], a simulator made by Geoquest.

5.2 Simulator input requirements

The numerical simulator is provided with the following parameters:

1. External boundary conditions that drive the experiments
2. Densities and viscosities of water and benzyl alcohol (oil)
3. Absolute permeability and porosity
4. Relative permeabilities and capillary pressures

5. Grid system, and
6. Initial fluid saturations and pressures.

5.3 History Matching Method

A history matching technique, coupled with the numerical simulator, was used in this research to inversely obtain the experimental parameters. The parameters are relative permeabilities, absolute permeability, and capillary premeability. This history matching procedure requires an efficient optimization algorithm to minimize the least-squares objective function. The Levenberg-Marquardt algorithm was used in this research. For our type of experimental data this method was stable and fast. The history matching steps are illustrated below (see Figure 5.1). The batch file, shown in Appendix C, follows these steps:

5.3.1 Step One

A batch file was built, and it consisted of a commercial simulator Eclipse 100 and sets of Fortran programs. The Fortran programs provide the calculated relative permeability sets as input to the simulator. Other Fortran programs are used to analyze the output of the simulator with the existing experimental data.

The fluids used in this research were water and oil. The relative permeability curves are the simulator parameter that is the subject of history matching. The porosity and absolute permeability were measured in the lab and the effect of the capillary forces was minimal for the oil flood. There are different representations for relative permeability curves and the most commonly used is the Corey's form where the relative permeability of each phase is a function of its own saturation as describes below:

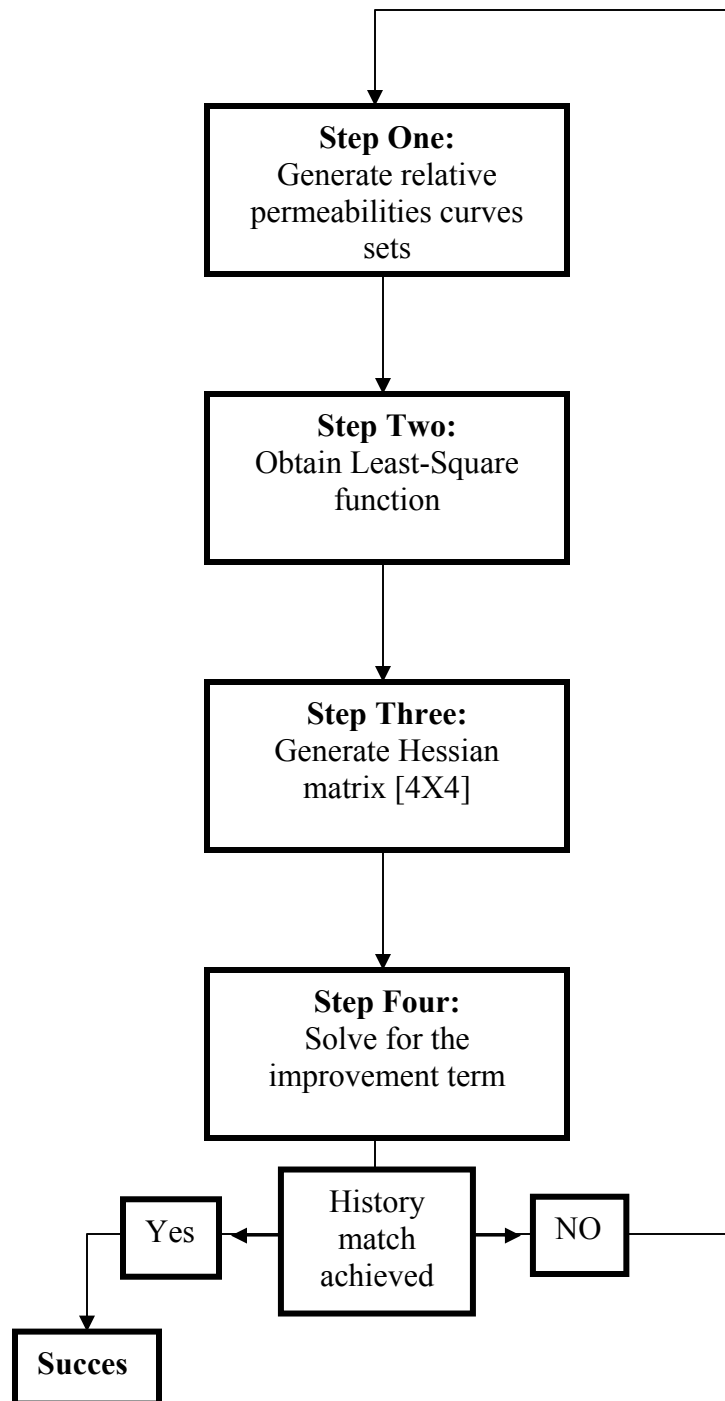


Figure 5.1: Schematic chart of the history match technique.

$$k_{rw} = a \left[\frac{s_w - s_{wr}}{1 - s_{wr}} \right]^b \quad (5.1)$$

$$k_{ro} = c \left[\frac{s_o - s_{or}}{1 - s_{or}} \right]^d \quad (5.2)$$

where k_{rw} is the water relative permeability, k_{ro} is the oil relative permeability, s_w is the water saturation, s_{wr} is the residual water saturation, s_o is the oil saturation, s_{or} is the residual oil saturation, and a , b , c , and d are the parameters that are adjusted in order to achieve an acceptable history match.

5.3.2 Step Two

The end points of water and oil saturations are determined by the experiment. Equations 5.1 and 5.2 are given an initial value of the controlling parameters (a , b , c , and d) to construct the first set of relative permeability curves as a function of saturation. After constructing the relative permeability curves, all the parameters, which are the input to the simulator, are completed. The specified output of the simulator is the saturation map of the system. This map is used to obtain the least-square function, J :

$$J = \sum_{i=1}^N (S_i^{\text{exp}} - S_i^{\text{cal}})^2 \quad (5.3)$$

where S^{cal} is the calculated saturation from the simulation, S^{exp} is the experimental saturation, and N is the total number of grid elements.

5.3.3 Step Three

This step is similar to Step Two. The parameter “ a ” is modified by the magnitude of ε ($\varepsilon=0.0001$). A modified set of relative permeability curves is produced and used by the simulator. A new saturation map is calculated and a new least-square function, Ja , is

calculated. The subscript “a” is indication of controlling parameter “a”. The first input of the right hand side of the Levenberg-Marquardt algorithm is then calculated:

$$\nabla J_a = \frac{J_a - J}{\varepsilon} \quad (5.4)$$

In this step, the sensitivity coefficient matrix, G , is also calculated as :

$$G_a = \frac{(S^{\text{exp}} - S^{\text{cal}})}{\varepsilon} \quad (5.5)$$

G_a is the first row entry of the G matrix. For example, if we have 460 experimental matching points, the G matrix will be [460X4]. Twenty-three is the number of history matching points and the four rows are the four parameters (a, b, c, and d). Thus, G_a contains the first 460 elements of the matrix. The first part of the left hand side of the Levenberg-Marquardt algorithm is the Hessian matrix which is:

$$H(X) = G^T G \quad (5.6)$$

G^T is the transpose of the G matrix, and it has a dimension of [4X460]. The Hessian Matrix is [4X4].

5.3.4 Step Four

A similar procedure of Step Three is done here for parameters b, c, and d, until the matrices $G^T G$ are complete.

5.3.5 Step Five

Now, the left and right hand sides of the Levenberg-Marquardt algorithm are obtained.

The algorithm then solves for the improvement term, ΔX_k :

$$(H(X_k) + \lambda I) \Delta X_k = -\nabla J(X_k) \quad (5.7)$$

where λ is a stability factor. The term ΔX_k is used in Equation 5.8 to update the model parameters.

$$X_{k+1} = X_k + \alpha \Delta X_k \quad (5.8)$$

where α is the step size.

Steps one to five are repeated until ΔX_k is very small and the history matching is achieved.

5.3.6 Algorithm Verification

To test and validate the history matching technique, a 2-D system was built to form a single two-dimensional layer. The system contained a fracture with the fracture tip. This layer was given specific properties. Then the simulator output was the saturation distribution along the layer. The relative permeabilities were changed and the first set was used as the target set. To test the model, a batch file was created to include the Eclipse simulator and the optimization codes. Then the batch file was switched-on to iterate on the relative permeability values until the target set was reached. Figure 5.2 illustrates the three relative permeability curves, target curve, initial set, and final set. The target and final sets show an excellent match confirming that the model is working well. Figure 5.3 shows the reduction of the error percentage, of the experimental and simulation saturation subtraction, with iteration number. Figure 5.4 illustrates the oil saturation profiles for the verification stage.

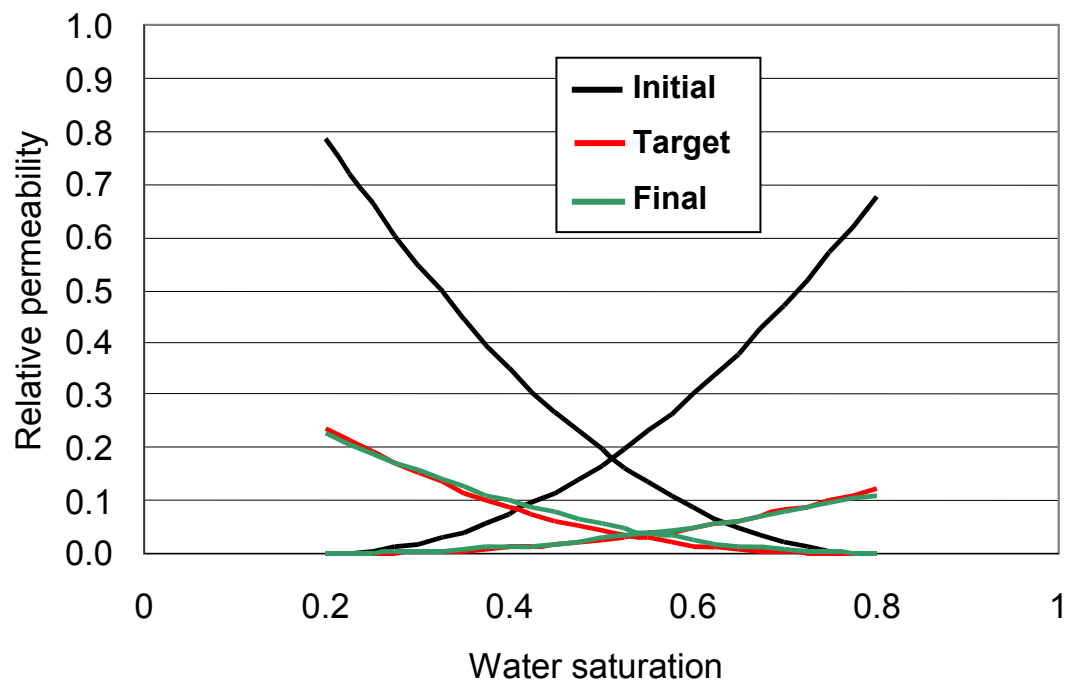


Figure 5.2: Verification of optimization algorithm using the relative permeability curves.

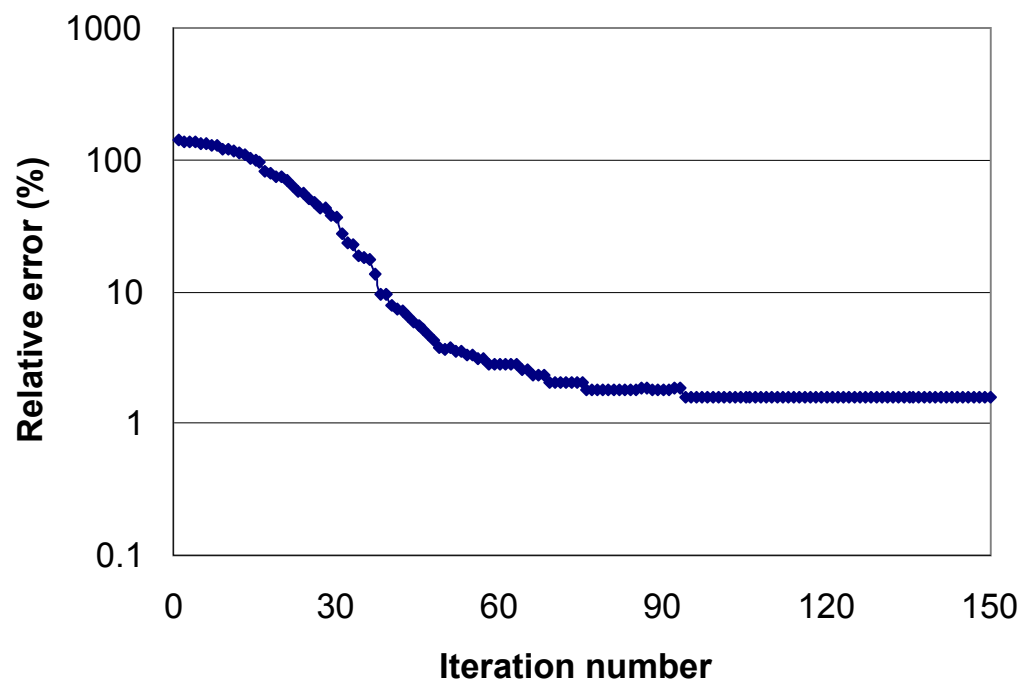


Figure 5.3: Reduction of error in the verification stage.

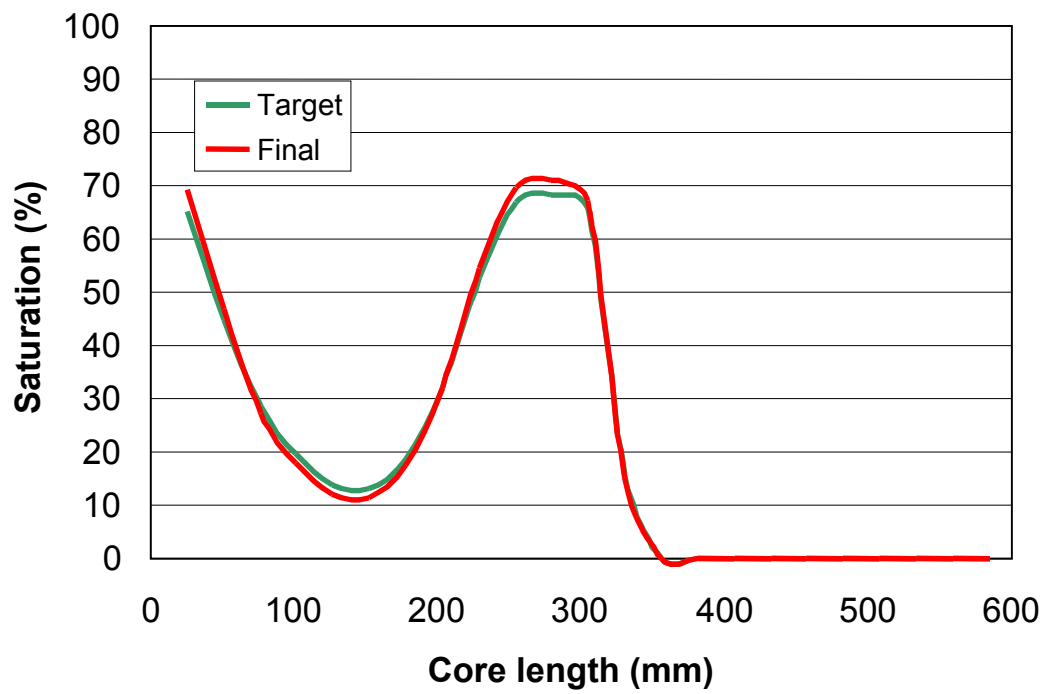


Figure 5.4: Simulated average saturation along the sample used for verification of the optimization algorithm.

5.4 The Two-Dimensional Model

The first step in this research is to develop a 2-D system to reduce the complexity of the problem and the simulation time. The fracture is introduced as high permeability/porosity blocks located at the center of the core at the inlet end. The simulator inputs are tailored to match the experimental data. Since the dimension of the core was 610 mm long and 51 mm in diameter, the 2-D model grid is developed as illustrated in Figure 5.5. The 2-D system is described in the y-z coordinates, with 610 blocks in the y-direction and 51 blocks in the z-direction (31,110 block system). The dimensions of a single block were 1 X 1 X 1 mm and the fracture aperture was represented by a 1 mm layer of grid blocks. The Eclipse file is in Appendix A.

The simulator was given the following experimental input values:

Absolute Permeability (in all directions) = 64 md

Average Porosity = 17.5%

Density of Oil = 1.0225 g/cm³

Density of Water = 1.0377 g/m³

Inlet Pressure = 2.0 atm

Outlet Pressure = 1.0 atm

Constant pressure was assigned at the inlet face.

A constant pressure production well was assigned at the outlet (one vertical well).

5.4.1 Preliminary Results

The initial tests simulated oil injection into a water-filled sample. One of the three distinguished middle layers of the core was chosen as the 2-D simulation base. The porosity was

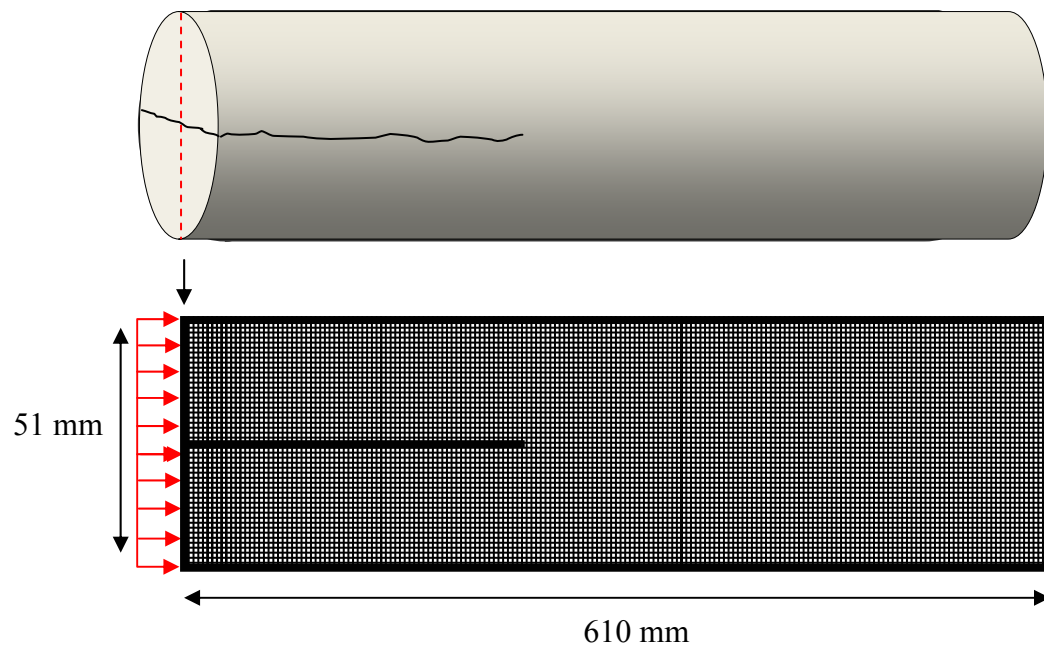


Figure 5.5: Simulation grid for the two-dimensional system.

measured for each block from the CT data. The absolute permeability was calculated by Timur's correlation presented in Chapter 4. The first simulation results of the 2-D system exhibited similar behavior to what was observed in the experiments (Figure 4.5). The oil moved in the fracture and then diverged into the matrix at the tip of the fracture. The starting set of relative permeabilities was obtained from the literature. These data were used as the basis of the history matching process. Figure 5.6 shows the axial simulated oil saturation maps along the layer. The simulated oil saturation maps are similar to the experimental results shown in Figure 5.7. In Figure 5.8, three major layers are highlighted. Now, the simulation is focused on one of these three middle layers. This layer has high permeability and porosity values. Figure 5.9 illustrates the average oil saturation profiles for layer 8 of the simulation and the corresponding locations in the experiment. These profiles are for different pore volumes injected and they show very good matches. Figure 5.10 illustrates the oil saturation profiles for the other two big layers (9 and 10) in the middle of the core, which are next to the layer in Figure 5.7. The match for the low permeability and porosity layer (number 9) is not as good as the match for the high permeability and porosity layers (8 and 10). The quality of this match was improved using the three-dimensional modeling, and will be discussed later. The advantage of using the two-dimensional model was to allow us to get initial estimates of simulation parameters and reduce the degrees of freedom of reservoir properties to be used in the three-dimensional model.

The 2-D model was used to simulate the water flood. It was difficult to simulate the water flood because of the equilibrium of the viscous and capillary forces between the matrix and fracture. Figure 5.11 illustrates the simulated water saturation maps during the

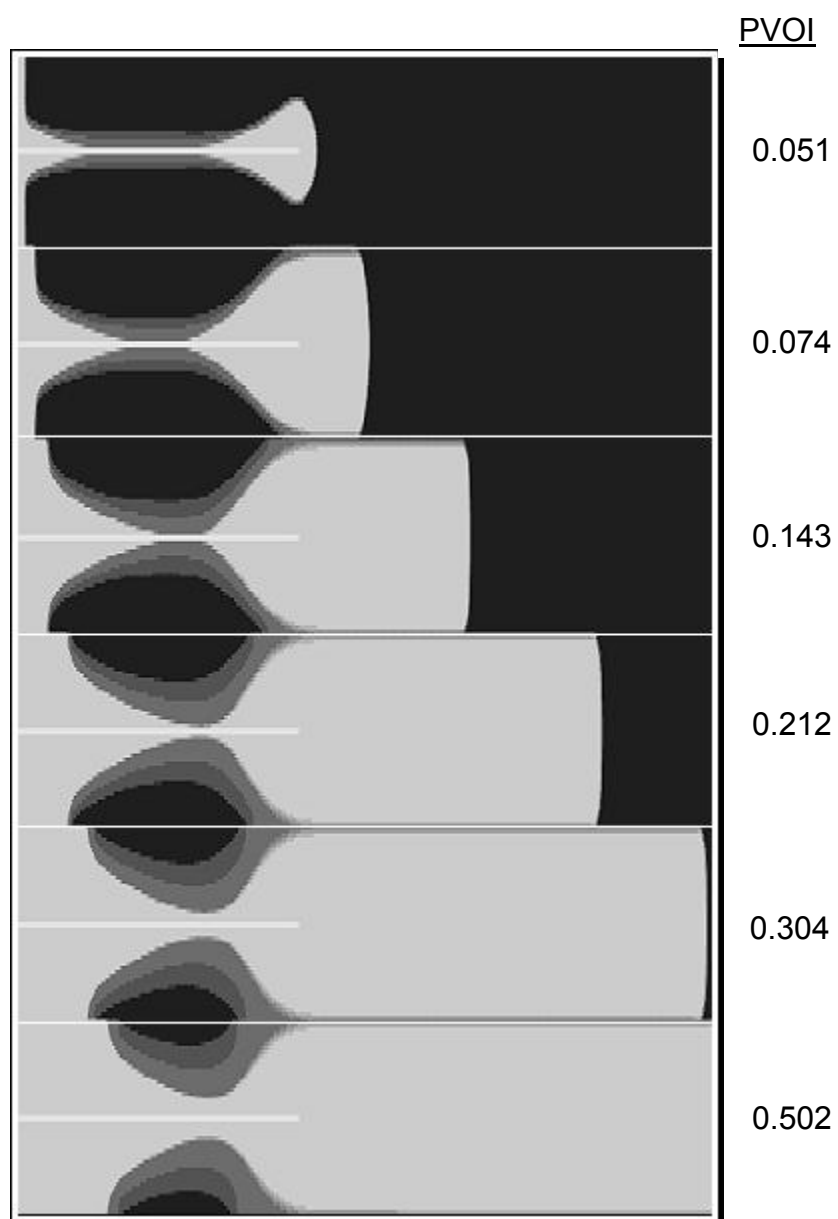


Figure 5.6: Simulated oil saturation for the two-dimensional single-layer case.

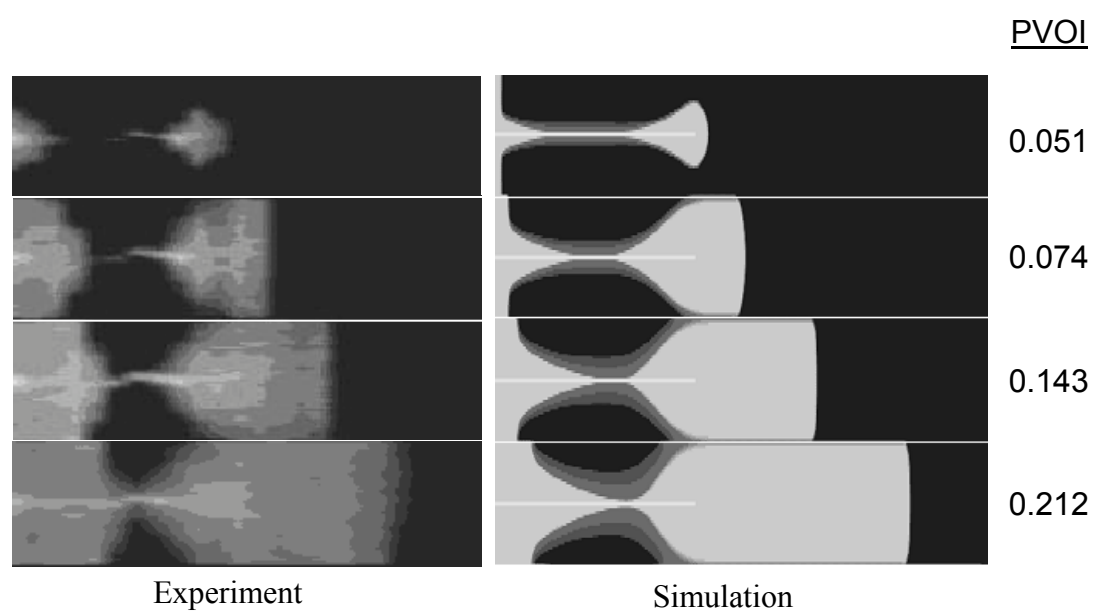


Figure 5.7: Experimental and simulated oil saturation maps for the two-dimensional system.

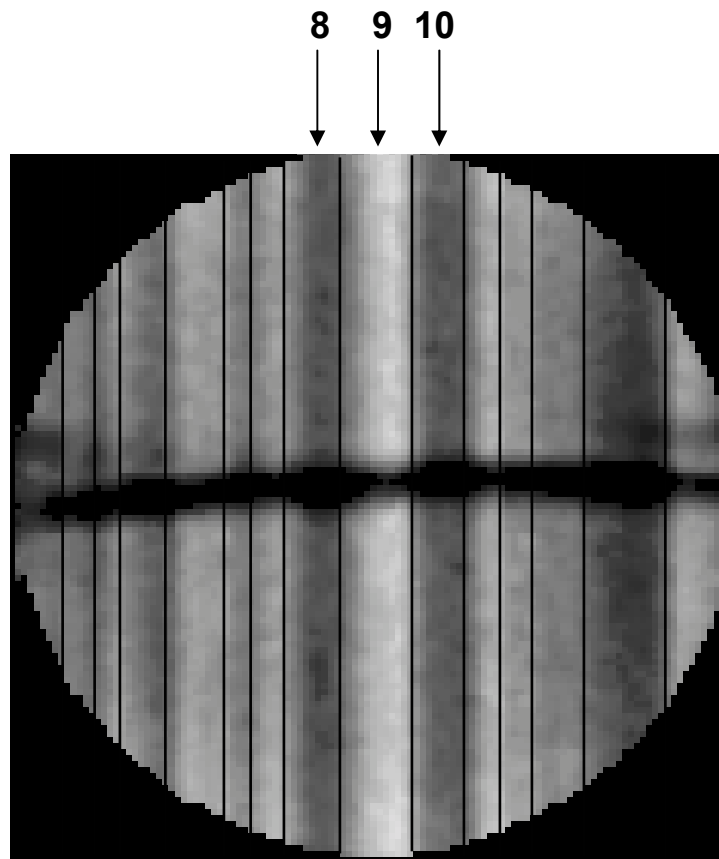


Figure 5.8: The major three layers in the core.

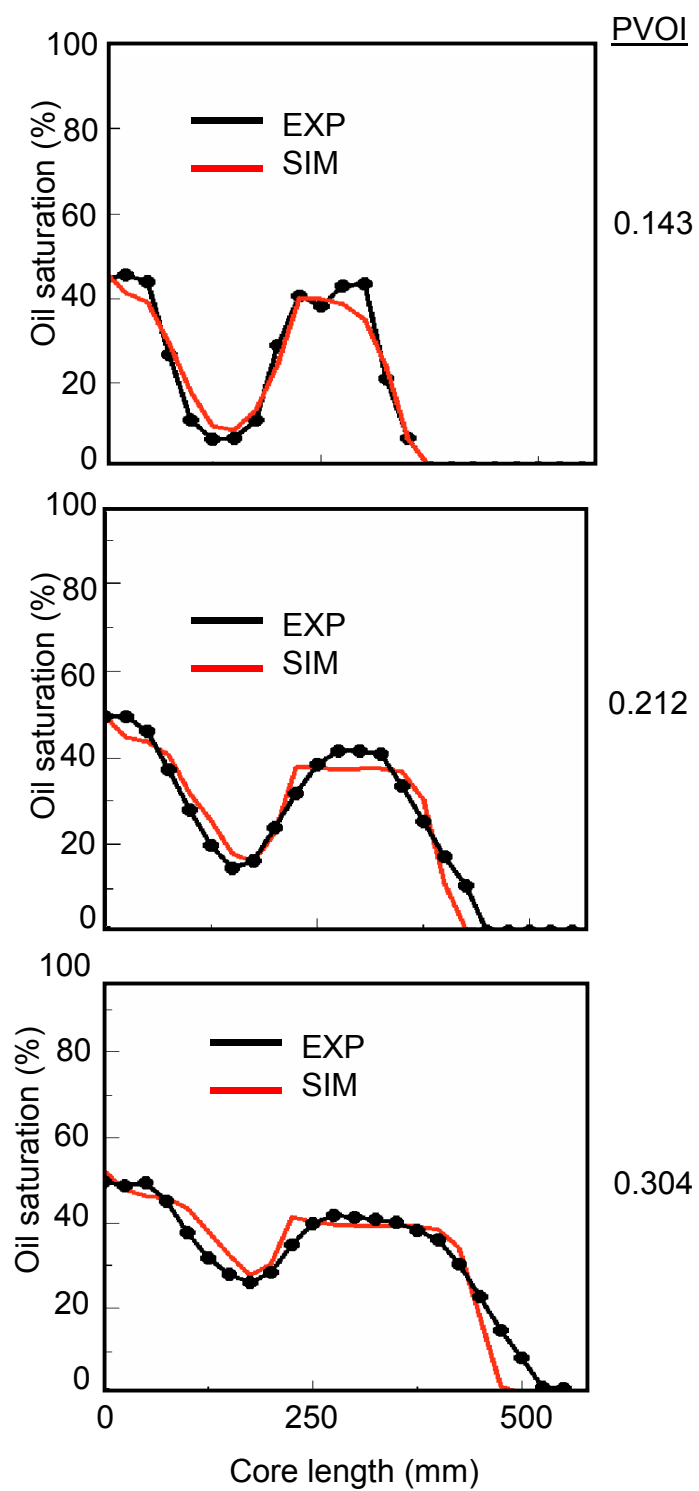


Figure 5.9: Simulated and experimental oil profiles of layer 8 at different pore volume.

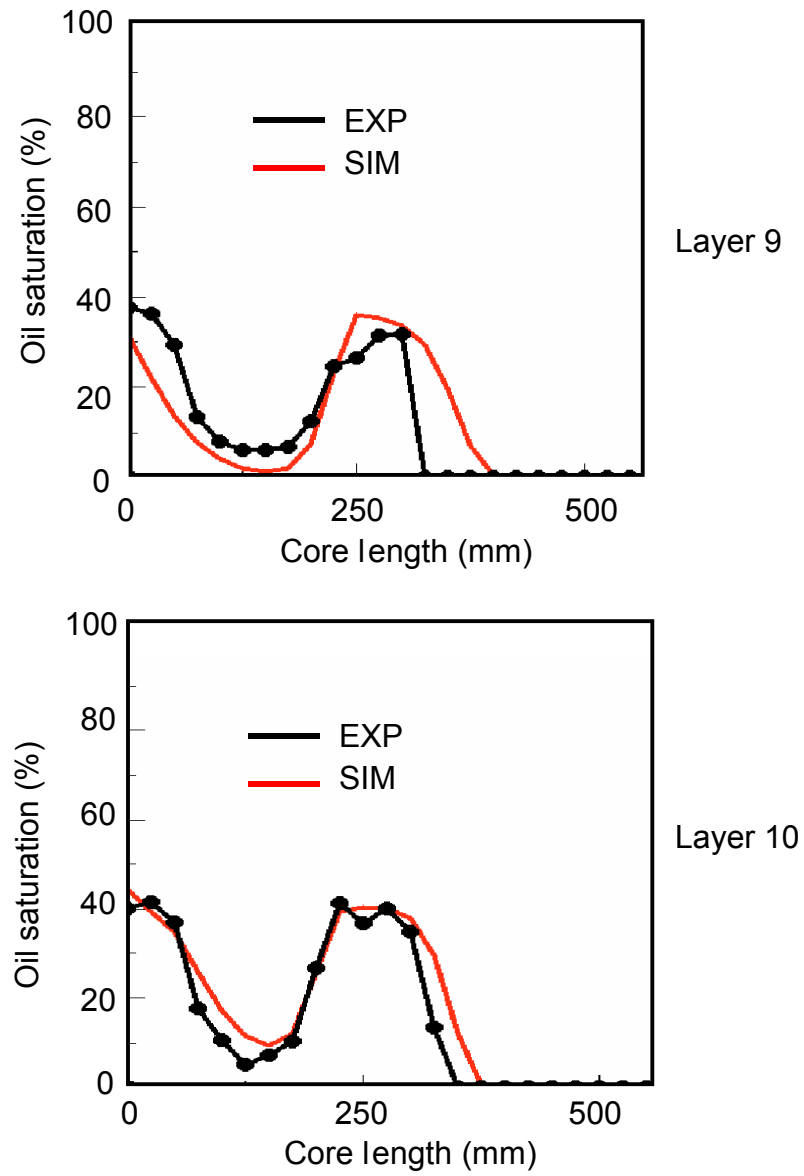


Figure 5.10: Simulated and experimental oil saturation for layers 9 and 10 at 0.143 PVOI.

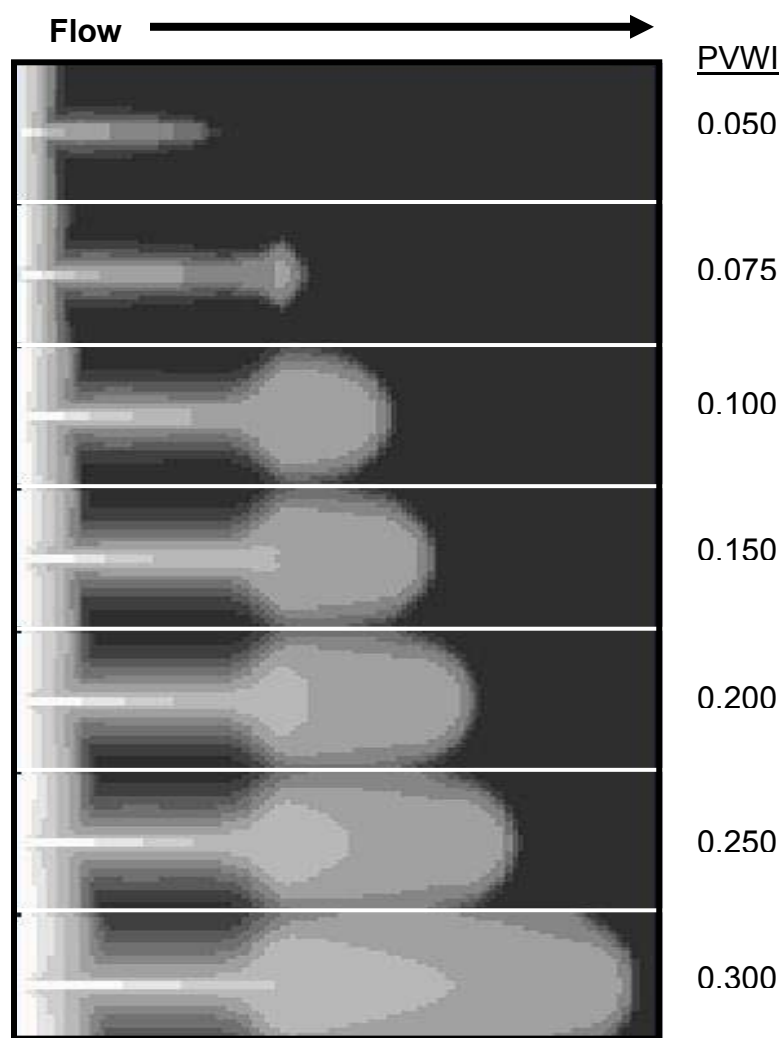


Figure 5.11: An axial slice of the simulated water flood for the two-dimensional model.

water flood process. The analysis of the 2-D oil and water flood results are discussed in the next chapter.

5.5 Three-dimensional Model

To test the three-dimensional model the oil flood was simulated and the relative permeabilities were slightly modified until the best history match was obtained. Figure 5.14 shows simulated and experimental axial oil saturation maps at different values of the pore volumes of oil injected. Figure 5.15 shows the simulation results of the axial average saturation along the core for layers 8, 9, and 10, respectively. The simulation results are improved in comparison to the two-dimensional simulation, especially in the low permeability and porosity layer number 9. In order to reduce the number of blocks in the simulator, the two-dimensional slices were divided into 15 vertical layers (15 blocks in the x direction, Figure 5.13). The z direction remained at 51 blocks. The axial direction, y, was reduced to 460 from 610 as in two-dimensional case. There were 460 CT slices along the axial direction and each slice represented 25 mm of the core. Each slice was divided into 20 blocks yielding a total of 460 axial blocks. In summary, the size of simulator grid was 15x51x460, giving a total number of blocks of 351,900. The Eclipse file is included in Appendix B.

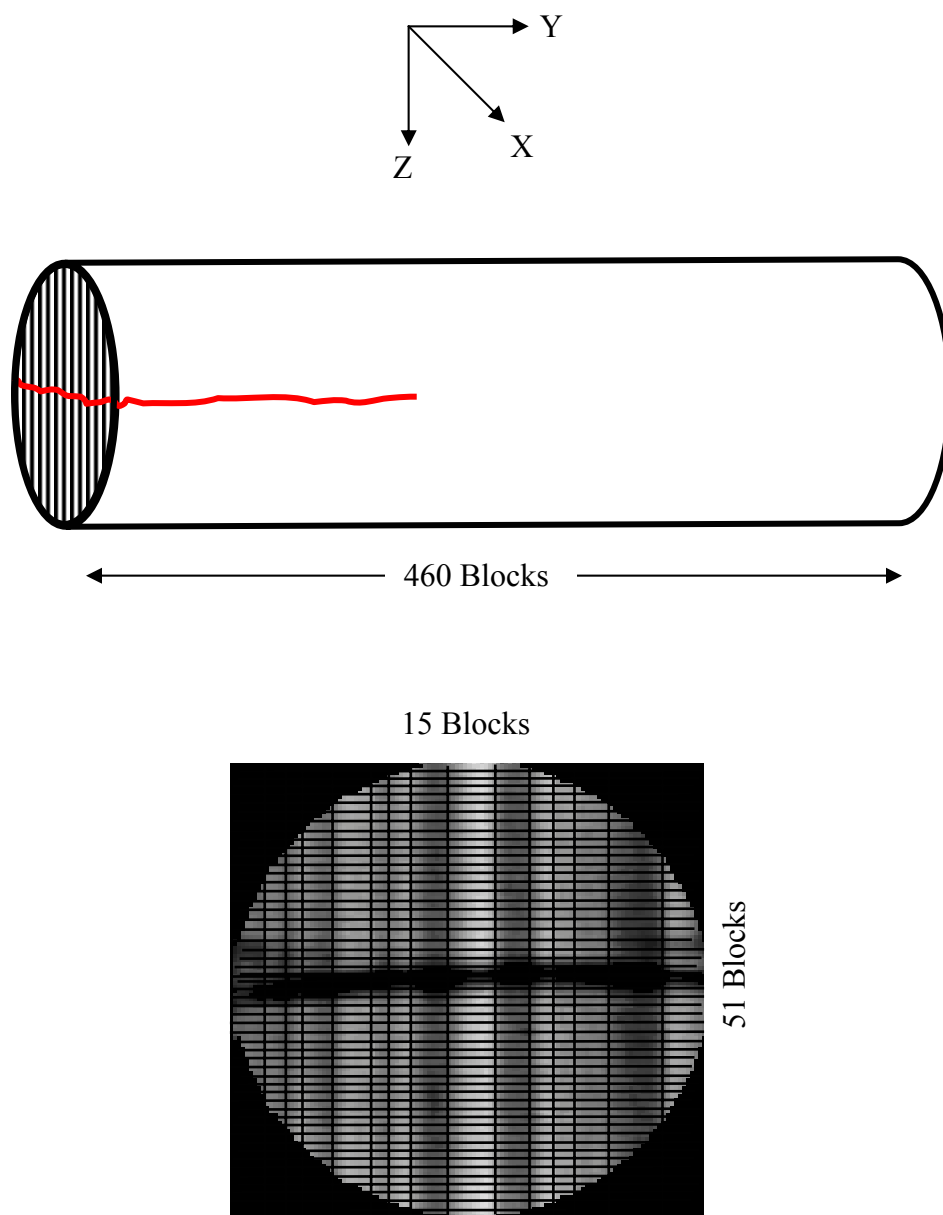


Figure 5.13: Three Dimensional layout of the system.

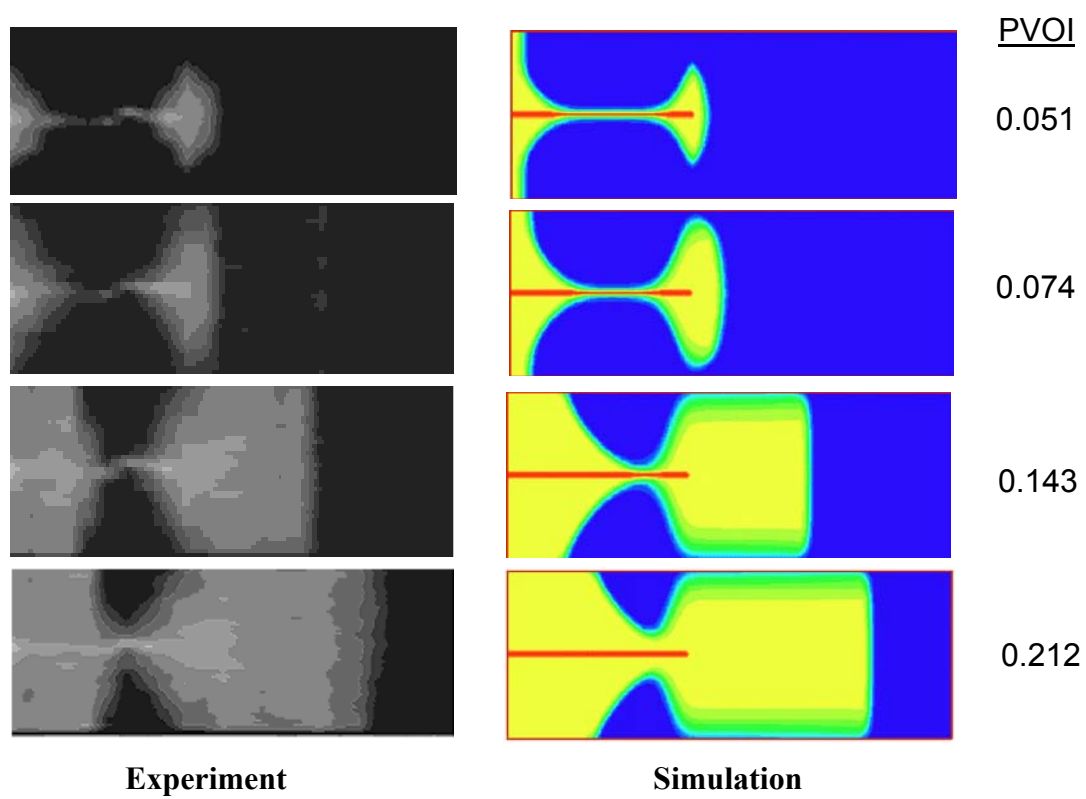


Figure 5.14: Simulated and experimental axial oil saturation maps for layer 8.

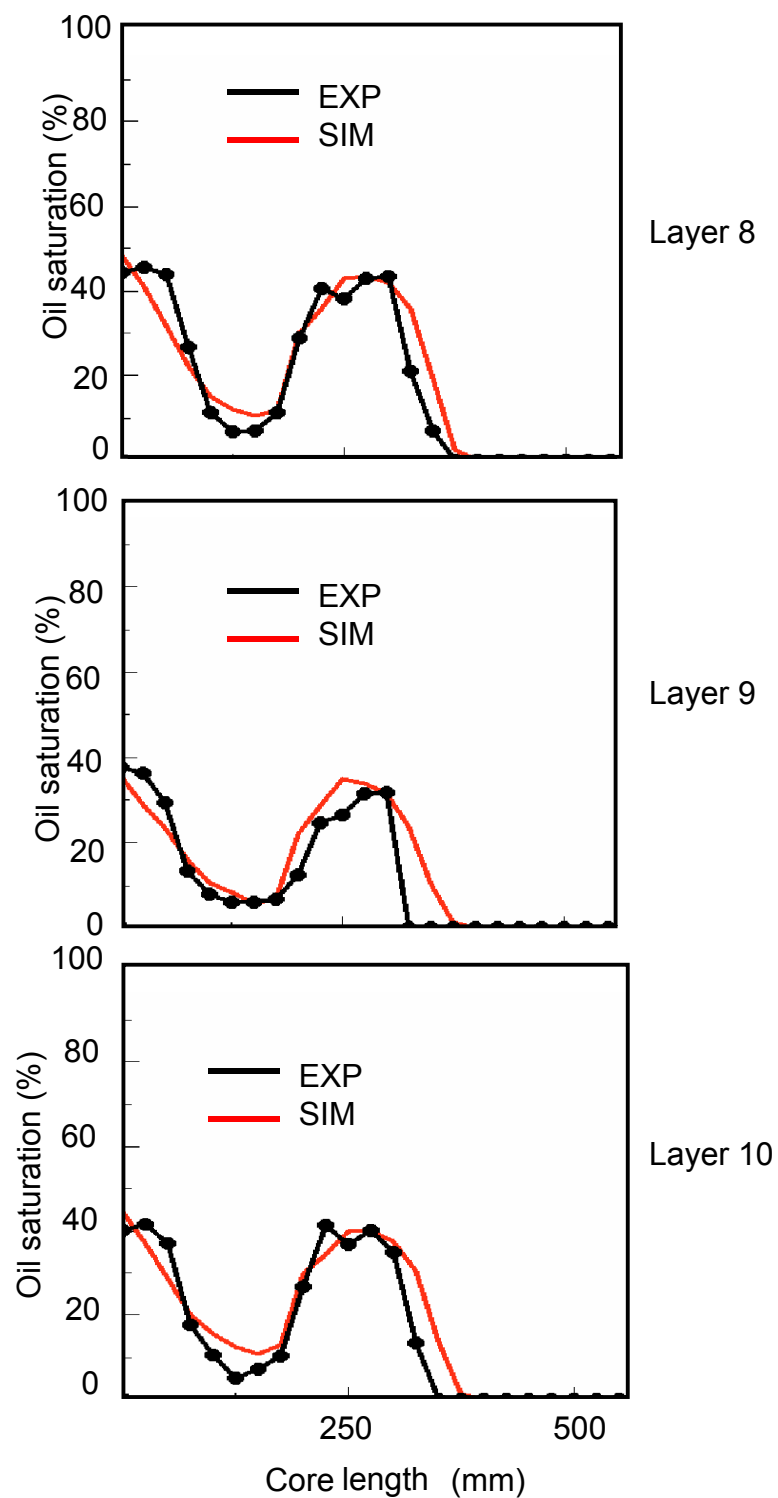


Figure 5.15: Simulated and experimental oil saturation at 0.143 PVOI.

Chapter 6

RESULTS AND DISCUSSION

In this chapter, we address the following questions: to where does the displaced fluid (trapped) above and below the fracture flow? How does the fluid, which is injected along the entire face of the core at the inlet end side, react to the presence of the fracture? Does the fluid converge to the fracture then diverge at the fracture tip to the matrix or does the fluid flow away from the fracture? Does the fracture tip accentuate the contrast between the layers? The answers to these questions are essential in order to understand fluid transport phenomena influenced by a fracture tip.

6.1 Oil Flood

The optimized parameters were used to simulate in three dimensions the oil flood processes. Streamlines during the oil flooding process at 0.212 PVOI are shown in Figure 6.1. The first map (Figure 6.1a) is the oil saturation contour map. The second map (Figure 6.1b) is the oil (displacing fluid) streamline flow vectors. The third map (Figure 6.1c) is the water (displaced fluid) streamline flow vectors. The fourth map (Figure 6.1d) is a combination of oil and water streamline flow vectors. Figure 6.1 demonstrates that for this specific experiment, the fluid flow is diverging to the matrix along the entire length of the fracture. These maps show the arrows of the flow patterns around the fracture. It also shows that the displaced fluid flows away from the fracture and establishes a path next to the edge of the sample, away from the fracture. These maps are a core achievement from modeling the experimental data. Initial analysis of the experimental results concluded that the fluid at the injection side was converging to the

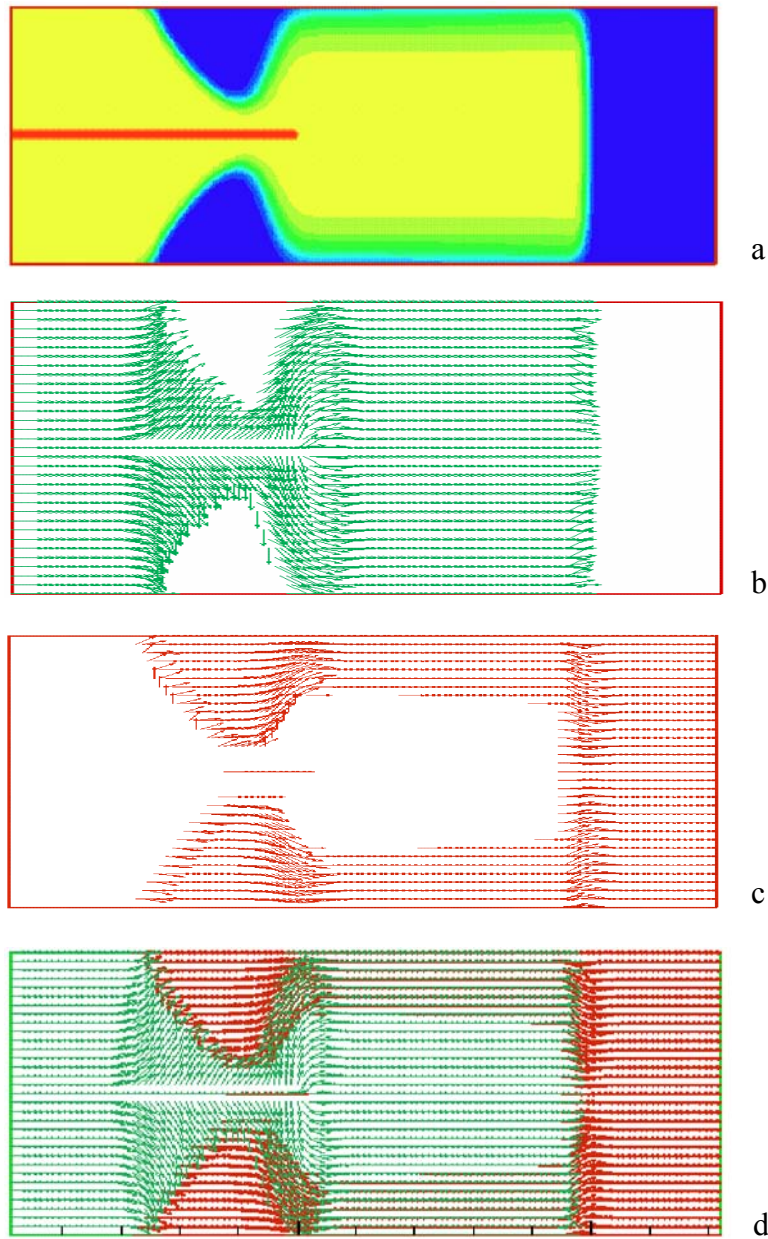


Figure 6.1: Four maps showing streamline of two fluids at 0.212 PVOI.

- a: Oil saturation map.
- b: Injected fluid streamline map.
- c: Displaced fluid streamline map.
- d: Injected and displaced fluids streamline map.

fracture. Figure 6.2a highlights the flow streamlines of the displacing phase and Figure 6.2b presents the combined streamlines in the actual proportions of the core. It was not clear if the displaced fluid above and below of the fracture would flow through the fracture then diverge at the fracture tip as more of the displacing fluid was being injected. It was also not clear if the fracture tip was a point of divergence for both phases behind the displacement front.

Figure 6.1 shows the influence of the fracture tip on the fluid flow streamlines. When the fracture is filled with the displacing fluid, the entire fracture acts as a feeder to the matrix. Thus, the displaced fluid can not flow toward the fracture but instead, flows away from fracture and finds its path at the edges of the core. The fracture tip is a diverging point for the displacing fluid where large amounts of the displaced fluid are transported. This divergence causes the displaced fluid (trapped) in the matrix above and below the fracture to be pushed to the edges of the core, it is clear in the third streamline map as shown in Figure 6.1. Figure 6.3 illustrates sketches of the fluid flow interaction between the matrix and the fracture. In sketch A, the fluid flow at the wall of the fracture is expanded to show the flow paths from fracture to matrix. Also, the injection is through the entire face of the core. In sketch B, the fluid is injected only through the fracture, which causes the fluid to flow to the outer edges of the core, including the inlet face. In sketch C, there is no fracture, and the flow has little transverse component. In sketch D, the fluid is injected along the face of the core and the injected fluid is flowing out of the fracture and into the matrix all along the fracture. This sketch is the representation of the experiments studied in this research. After the success of the history matching of the

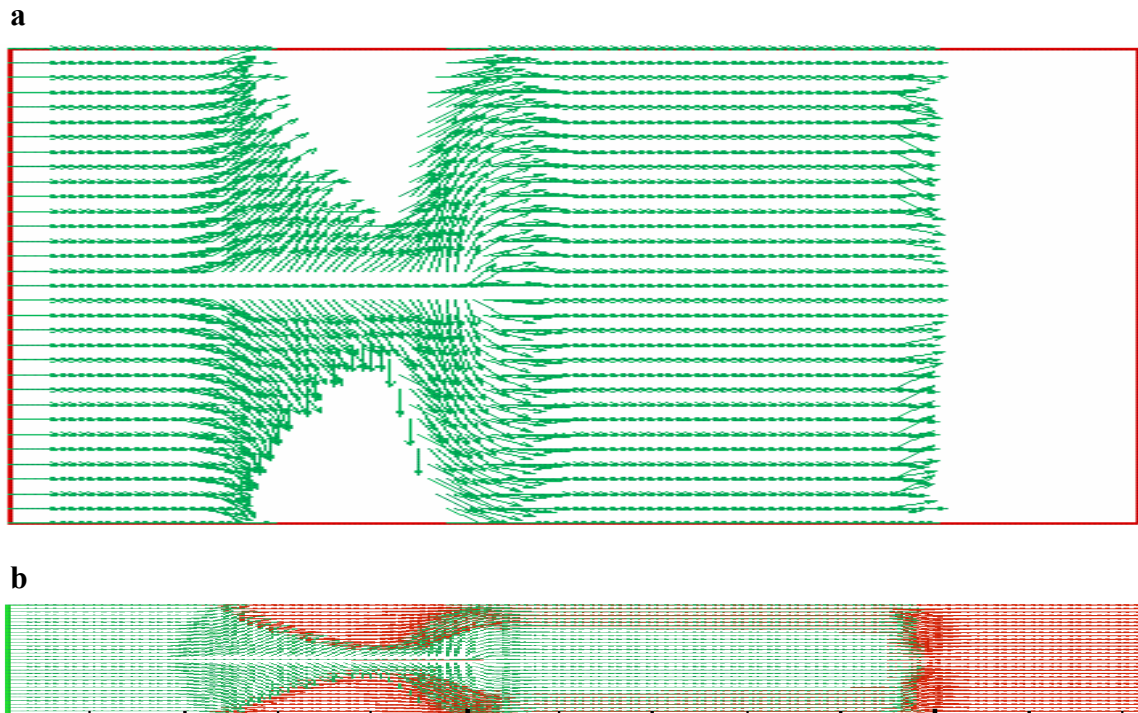


Figure 6.2: a) Expanded view of the oil streamlines during the oil flood.
b) Combined streamlines map shown at the actual proportions of the core.

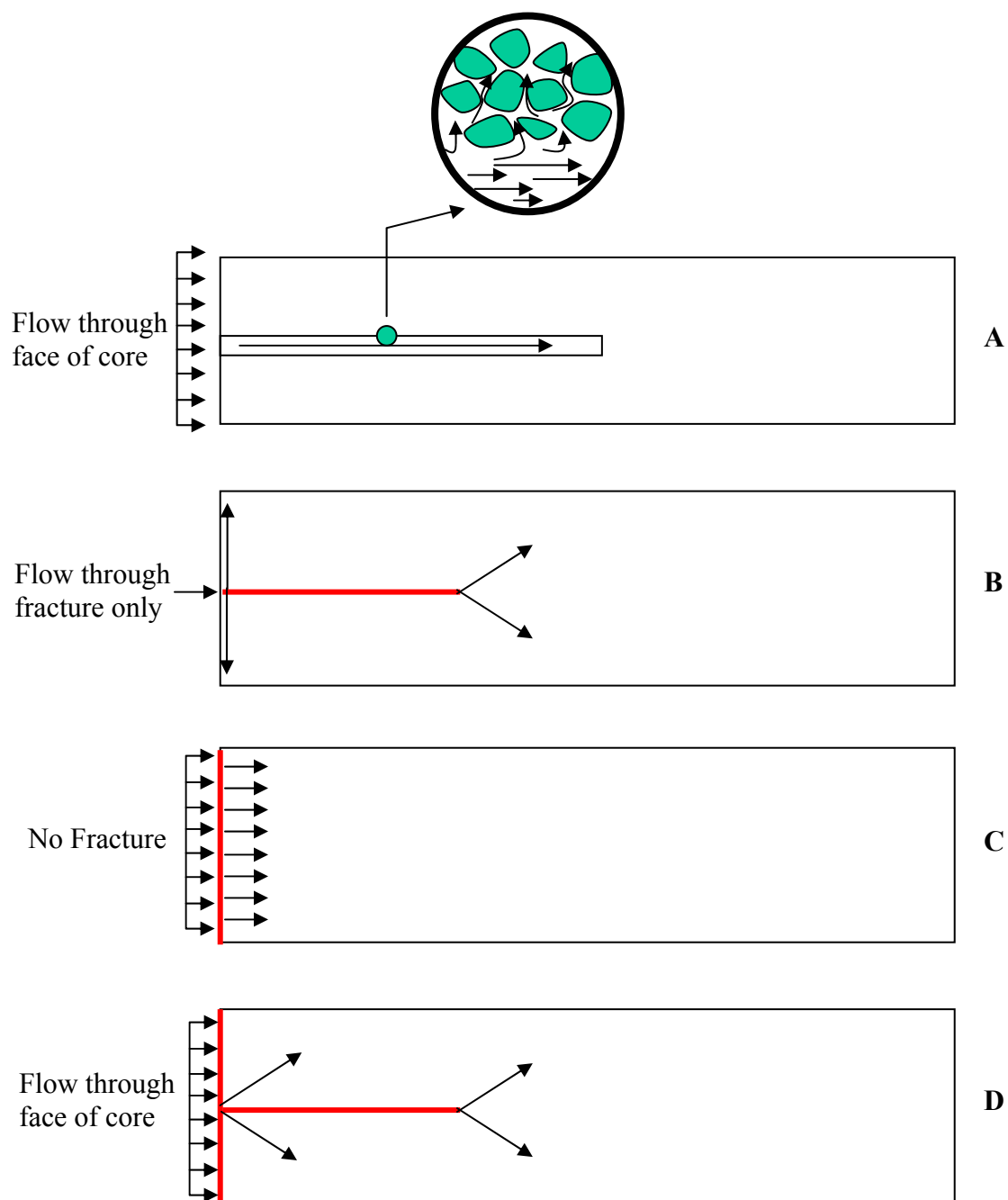


Figure 6.3: Sketches of fracture-matrix interaction during two-phase flow.

experimental data, a two layers' system is modeled to study inter-layer communication. One layer has high permeability and porosity values and the second layer has low permeability and porosity values, Figure 6.4. The dimensions and grid system for the two layers were similar to the 2-D system.

Figure 6.5 shows pressure and saturation profiles along the layers when they are completely isolated at different values of pore volumes injected. Both layers have the same constant pressure boundaries. These profiles allow us to investigate the fluid flow transport from one layer to the other. The fluid in the high k and ϕ layer was displaced ahead of the low k and ϕ layer. The high k and ϕ layer had higher fluid pressure than the low k and ϕ layer behind the front while the low k and ϕ layer had higher fluid pressure than the high k and ϕ layer ahead the front. This gives an idea of the fluid transport direction between the layers behind and ahead of the front. The fluid will tend to flow to the low k and ϕ layer behind the front and from low k and ϕ layer ahead of the front.

The two-layers model was test with completely isolating the two layers from each other and then increasing the communication between the layers by increasing the x-axis permeability (k_x). Figure 6.6 illustrates the average saturation of the low k and ϕ layer at different levels of inter-layer communication. Figure 6.7 illustrates similar saturation profiles for the high k and ϕ layer.

The layers in the core are connected by the fracture regardless of the level of inter-layer communication. When inter-layer communication is allowed, the overall amount of fluid entering the matrix at the inlet region of the sample is reduced. At the

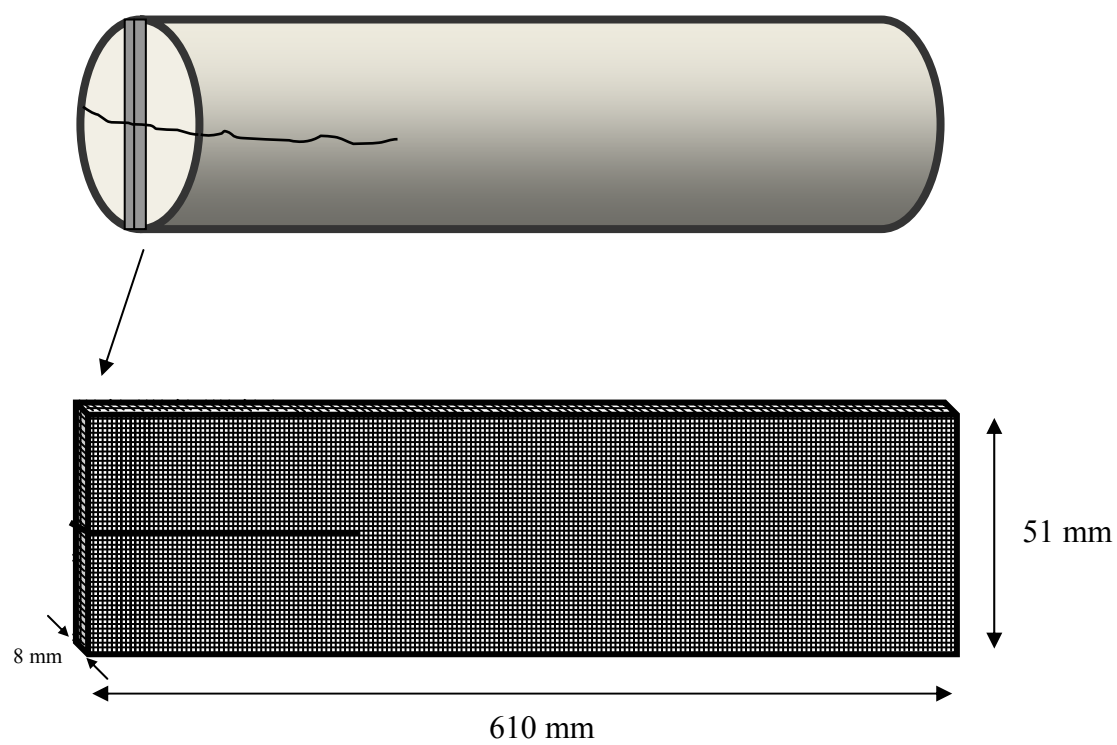


Figure 6.4: Simulation grid for a two layer system.

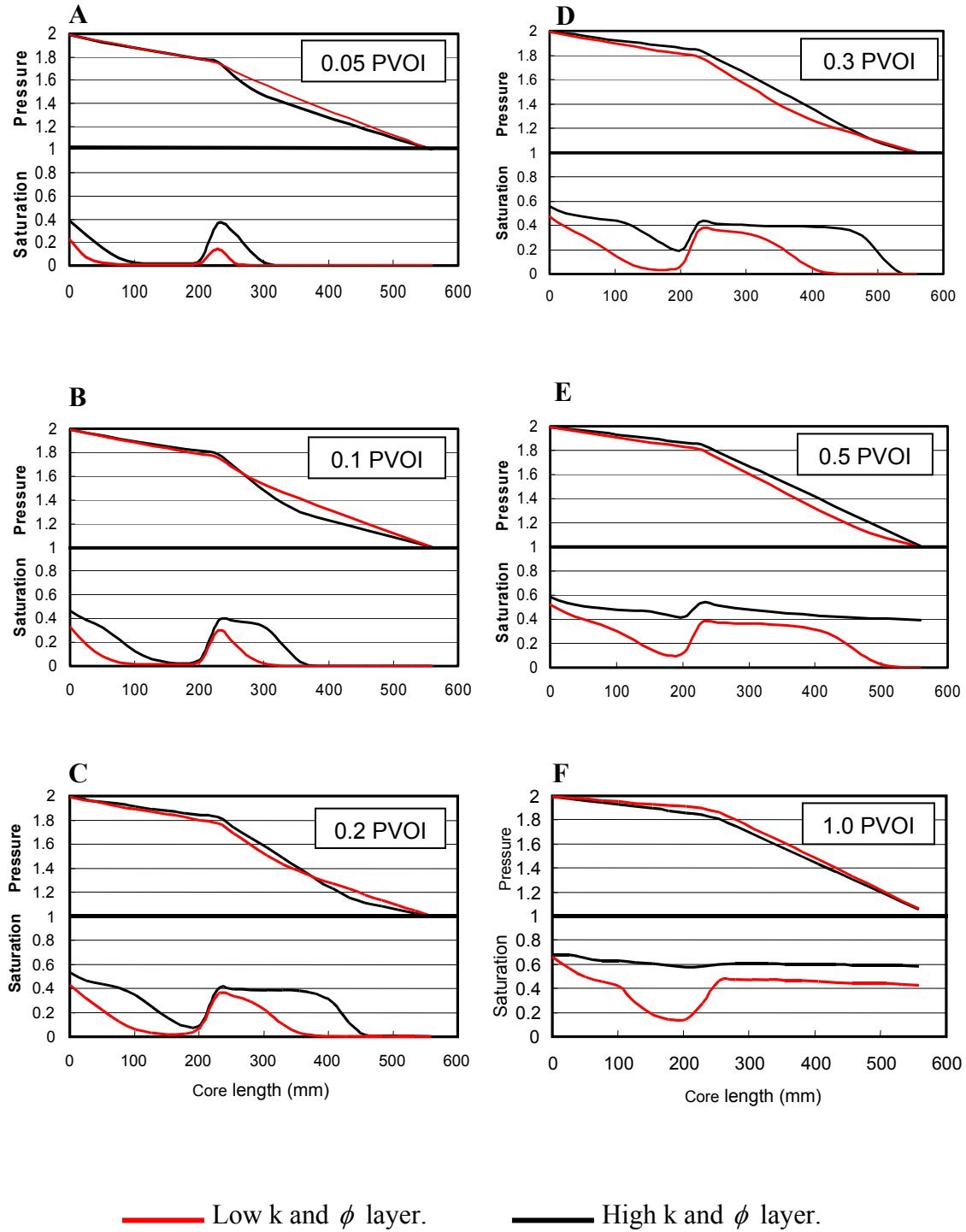


Figure 6.5: Saturation and pressure profiles for two isolated layers.

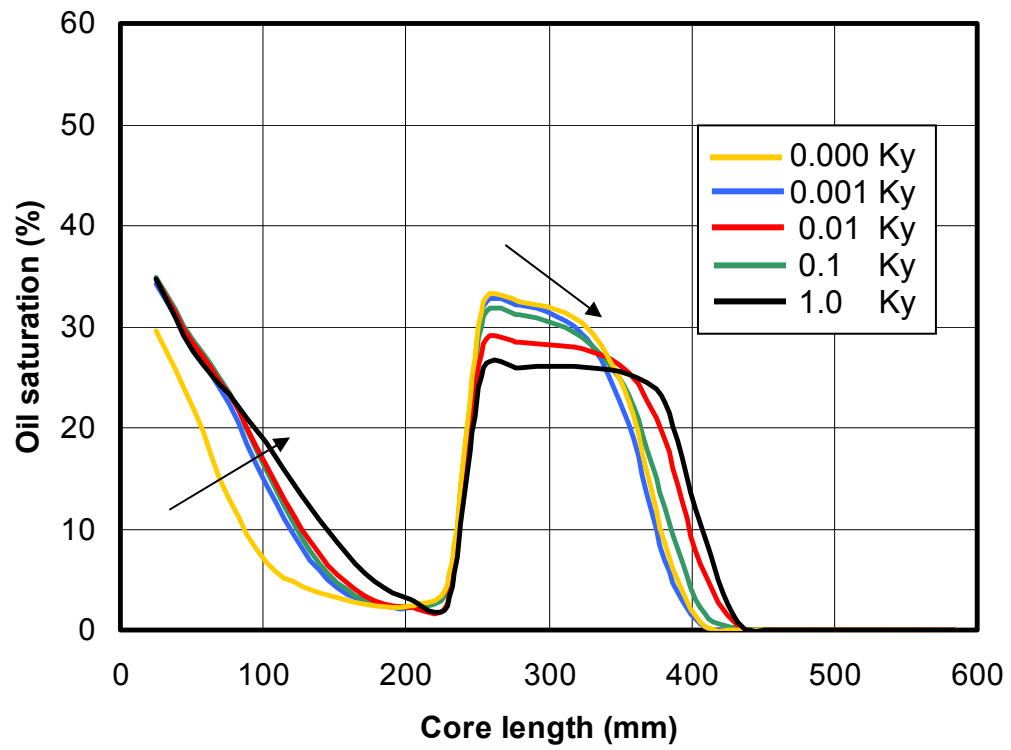


Figure 6.6: Oil saturation profiles for the low k and ϕ layer as a function of inter-layer communication.

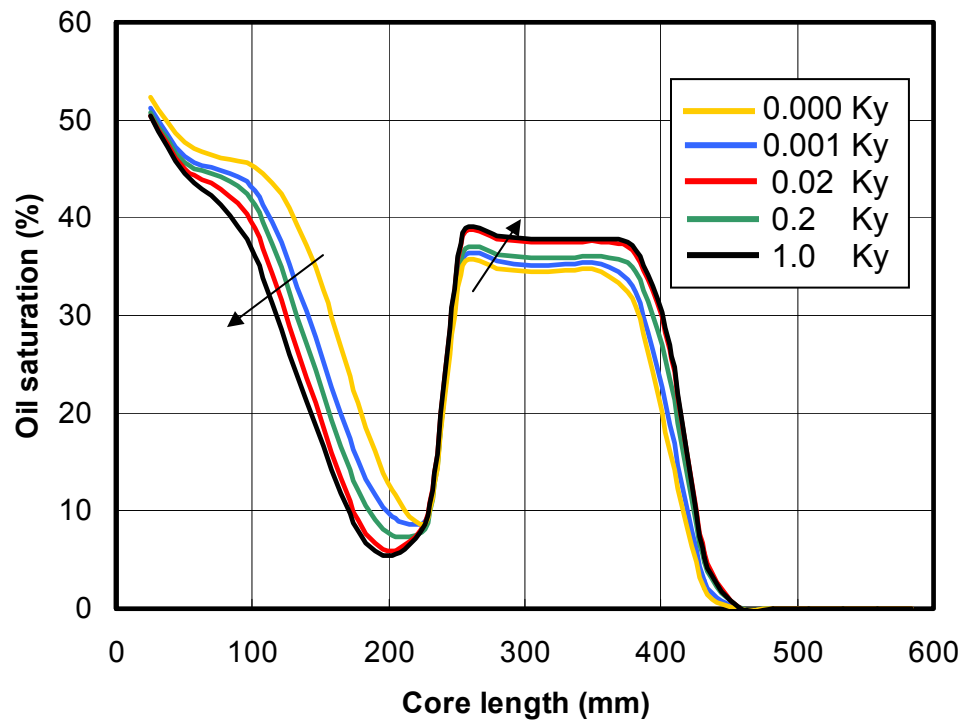


Figure 6.7: Oil saturation profiles for the high k and ϕ layer as a function of inter-layer communication.

same time, the graphs show that the fluid saturation increases at the inlet side in the low k and ϕ layer and decreases at the same location in the high k and ϕ layer.

Without inter-communication at the inlet part of the core, there is high oil saturation in the high k and ϕ layer next to a water saturated low k and ϕ layer. When inter-layer communication is introduced, water is extracted from low k and ϕ layers due to capillary forces, thus allowing oil to advance in low k and ϕ layers. Hence, the difference between the two fronts' positions in the inlet part of the core is reduced. The front in the high k and ϕ layer is retarded and the front in the low k and ϕ layer is advanced. Figure 6.8 presents overall saturation profiles of the two layers together, with and without inter-layer communication. When inter-layer communication is established, there is an increase in the overall oil saturation ahead of the tip and a decrease in oil saturation at the inlet of the high k and ϕ layer. The pressure at the inlet and the outlet ends of the sample are fixed. All the saturation profiles presented in Figures 6.6 through 6.8 have fixed pore volumes of oil injected. At the leading front part of the fractured region, inter-layer communication reduces the location differences between the fluid fronts. Since there is less oil at the inlet end of the core, both fronts advanced further into the core ahead of the fracture tip. Just past the fracture tip there is an increased separation between layers.

There is an increase in the oil saturation in the high k and ϕ layer and a reduction in the oil saturation in the low k and ϕ layer as communication is established. The explanation of the accentuation of the permeability contrast between the layers at the fracture tip is because of two processes. At the tip region, there is a strong vertical flow component that favors the high k and ϕ layer and flow rates are high.

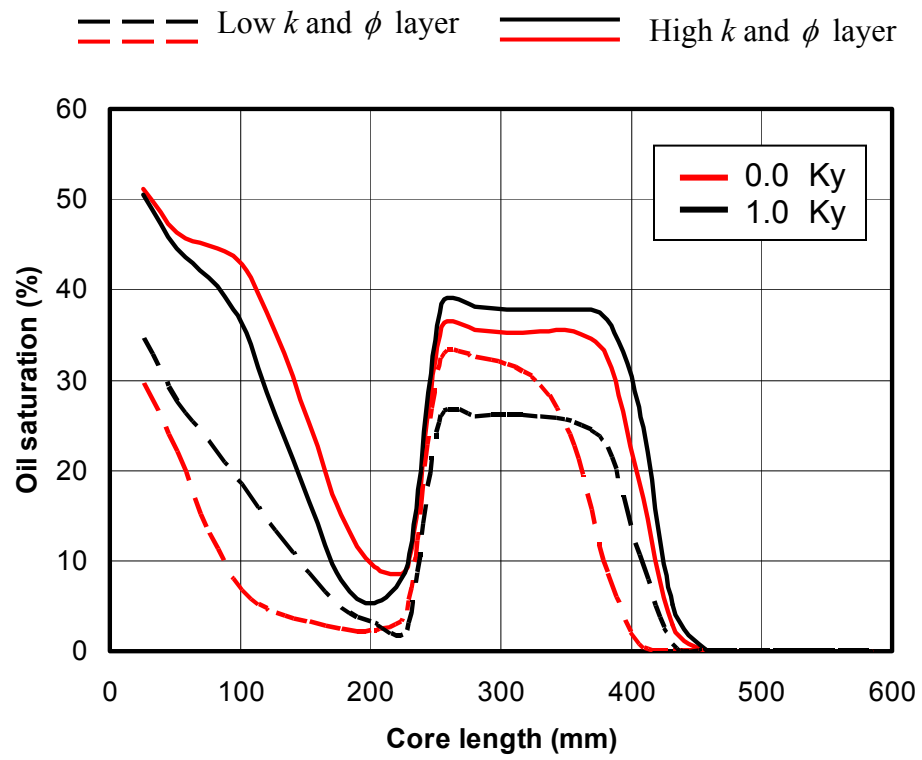


Figure 6.8: Average oil saturation profiles for the two-layered system, with and without inter-layer communication.

Since there is less overall water displacement at the inlet, there is less water flowing in the matrix in the region of the tip, thus, allowing more of the fluid in the high k and ϕ layer to be displaced immediately ahead of the fracture tip. The increased convective activity at the tip region favors the high k and ϕ layer and reduces the overall saturation in the low k and ϕ layer. Thus, the presence of the tip and inter-layer communication increase the fronts' location difference between the layers in the flooded area just past the tip of the fracture.

The transition of oil saturation between two adjacent layers is shown in Figure 6.9. The two layers (8, high k and ϕ layer, and 9, low k and ϕ layer) are mapped experimentally by 10 pixels in the non-axial dimension (X), as shown by the schematic inset in Figure 6.9. Consider ten consecutive vertical-axial planes (Y - Z) shown in the inset. The first plane is in the middle of layer 8 shown as the two-dimensional axial slice in Figure 6.9. The average saturations along each of the ten planes is shown in Figure 6.9 demonstrating the saturation transition between the layers. Behind the fracture tip, where the layers are well defined and continuous, there is a strong contrast between the layers even at a value of 0.504 PVOI, which is after oil breakthrough. Ahead of the fracture tip, the saturation difference is not as large as in the region that contains the fracture, indicating strong inter-layer communication.

A numerical study of the saturation distribution in two adjacent layers is shown in Figure 6.9. The two layers were simulated by ten axial layers (each layer in the Y - Z domain). Each layer was divided into five thin layers that matched the CT pixel resolution in the non-axial direction.

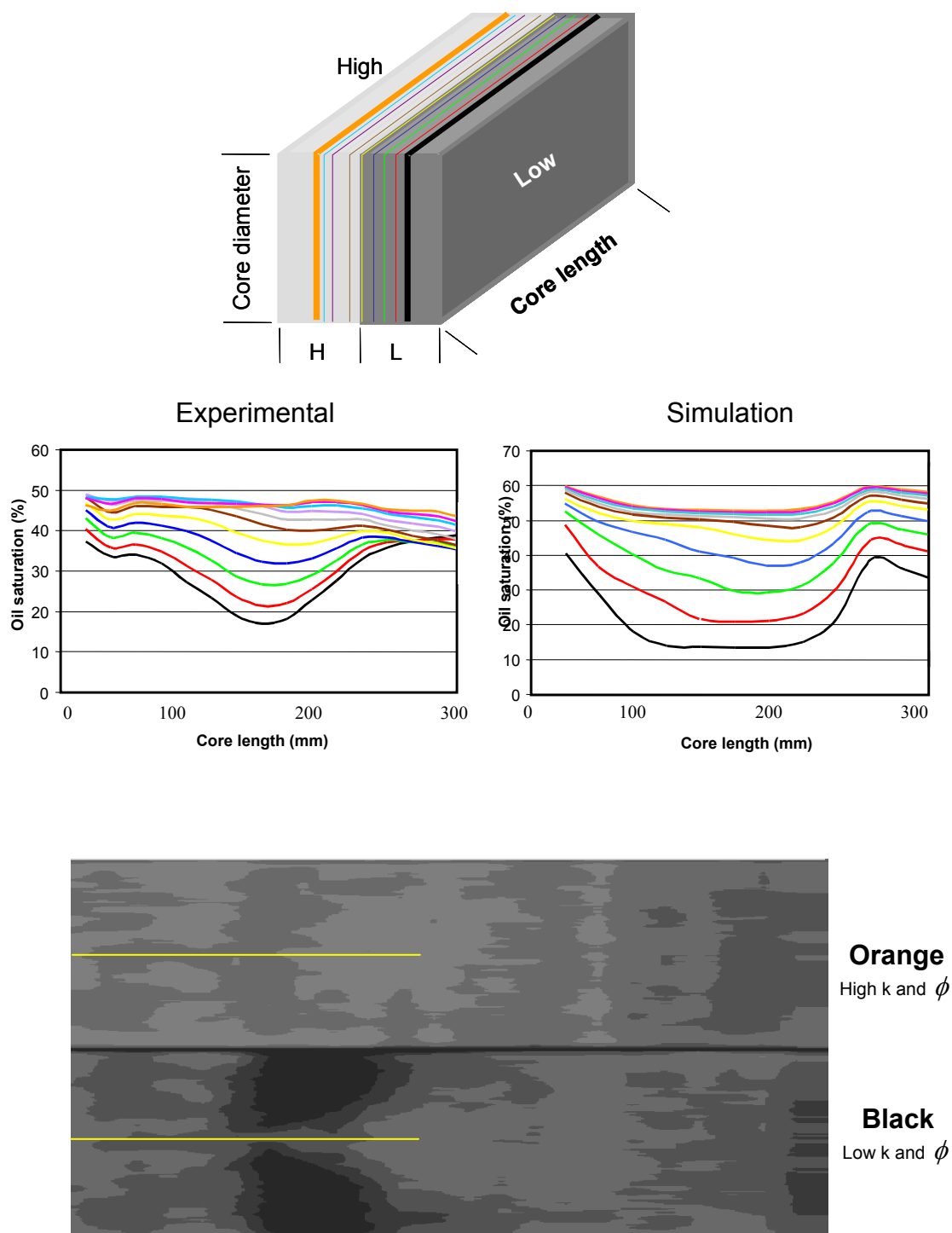


Figure 6.9: Oil saturation transition along the two layers (high and low).
A schematic of the ten layers is shown by the inset at the top of Figure 6.9.

The two CT axial slices shown at the bottom of Figure 6.9 denote the first and last layer in the simulation. The simulated transition of the saturation between the layers shows similarities to the experimental results. There is a large variation in saturation within the low k and ϕ layer, and a small variation in the high k and ϕ layer. The saturation profiles ahead of the tip are different because in the simulation the layers are continuous all along the simulated core but in the actual sample the layers are not continuous after the tip. Also, the simulation was done using only two distinct layers while the actual experiment contained many more layers.

Another way to consider the influence of the fracture tip on layers communication is presented in Figures 6.10 and 6.11. Figure 6.10 shows profiles of the layers' saturation above the fracture just behind the fracture tip. The two middle high k and ϕ layers were flooded first and more fluid was injected into them than the middle low k and ϕ layer (shown by the arrows between the red and the black curves). This is due to the strong vertical movement of the fluids. When the two high k and ϕ layers were at high oil saturation, the middle layer started to be flooded from the fracture. Figure 6.11 shows the saturation profiles at the same vertical location but just ahead of the fracture tip. The profiles are advancing at the same rate across the sample due to the strong horizontal component of flow.

Figure 6.12 shows simulated oil flow rate profiles at three locations along the core illustrating the influence of the fracture tip. The profiles are at 0.5 pore volumes injected. The profiles at the inlet side (Figure 6.12a) show a very high flow rate in the fracture and a low flow rate in the matrix.

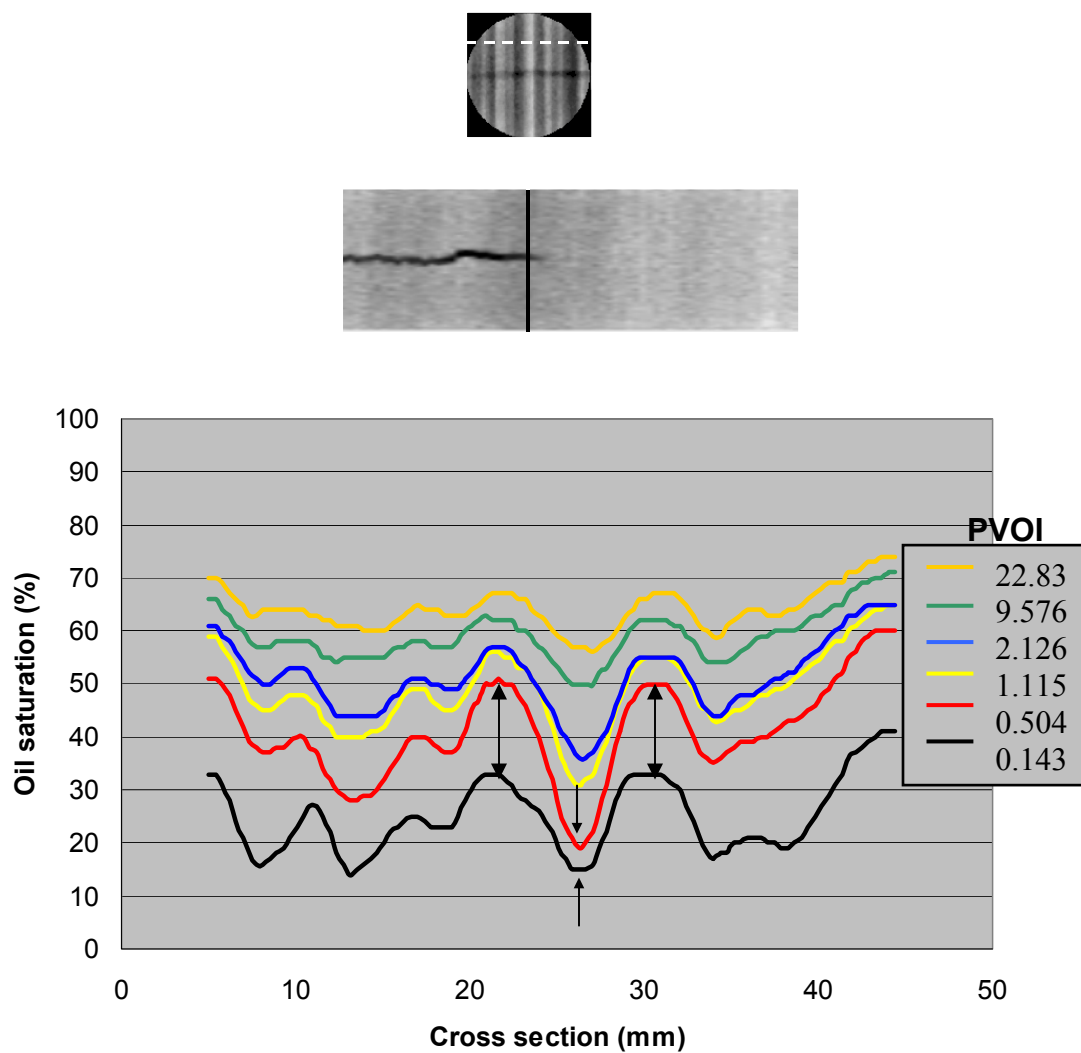


Figure 6.10: Oil saturation profiles across layers just before the fracture tip.

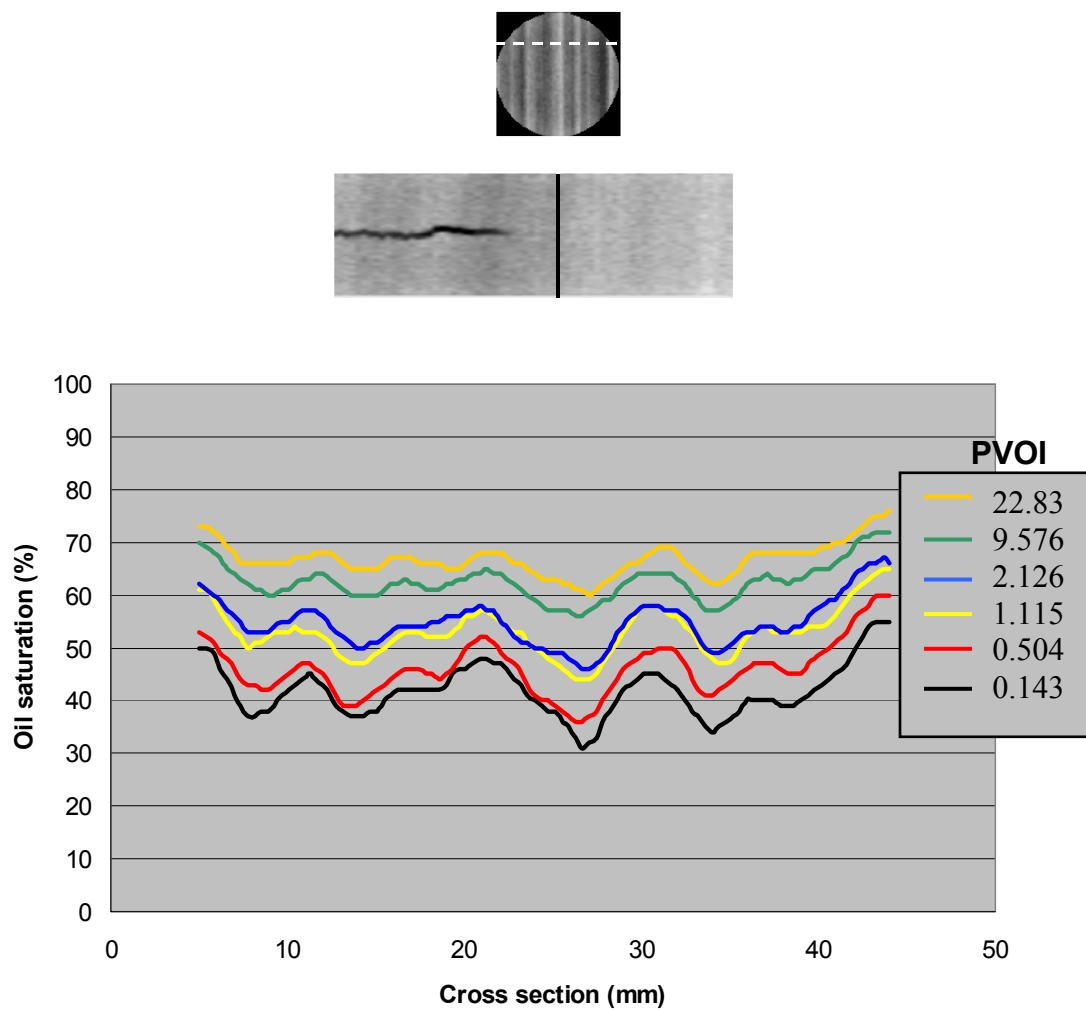


Figure 6.11: Oil saturation profiles across layers just ahead of the fracture tip.

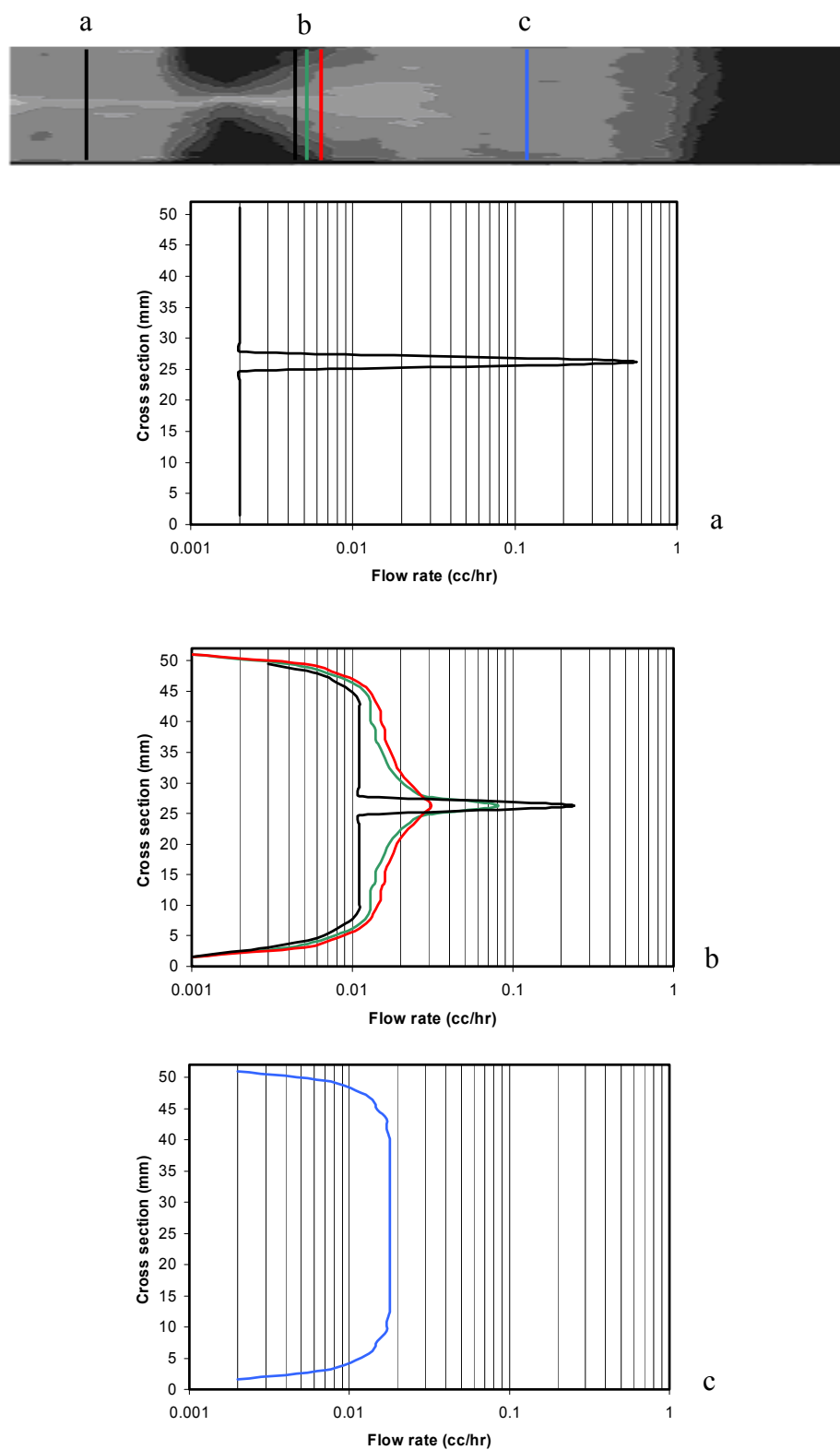


Figure 6.12: Tip influence on oil flow rate at different location of the core.

The profiles at the fracture tip (Figure 6.12b) show how the tip transforms the flow rate profiles by the vertical divergence of the flow away from the fracture. The flow rate profiles in the matrix, ahead of the fracture (Figure 6.12c) are higher than in the fracture region due to the flow diverging to the matrix. It also shows lower oil saturation at the edges of the core away from the fracture. The outer regions must accommodate the displacement of the trapped water in the matrix along the fractured region of the core.

6.2 Water Flood

The experimental data describing the water flood displacement, as seen in chapter 4, exhibits different behavior from the oil flood. The difference between the two flood processes is the viscosity ratio between the oil and the water. In the oil flood, the system is saturated with 1 cp water and the injected fluid had a viscosity of 5 cp. In the water flood, the system is saturated with 68% oil with viscosity of 5 cp and 32% water with viscosity of 1 cp. The capillarity forces and relative permeability were also different between the two floods, and will be presented in this chapter. In chapter 5, results of the water flood simulation are presented. In this chapter, a detailed discussion of the water flood processes and its simulation are analyzed.

Figure 6.13 shows axial slices of water saturation at different values of pore volumes injected. In each slice, two locations are highlighted, the water volume at the fractured region and at the non-fractured region. The analysis of this figure will help understand the forces affecting the fluid flow displacement. Figure 6.14 shows a plot of the volume of the water in each single layer highlighted in Figure 6.13. The water volume

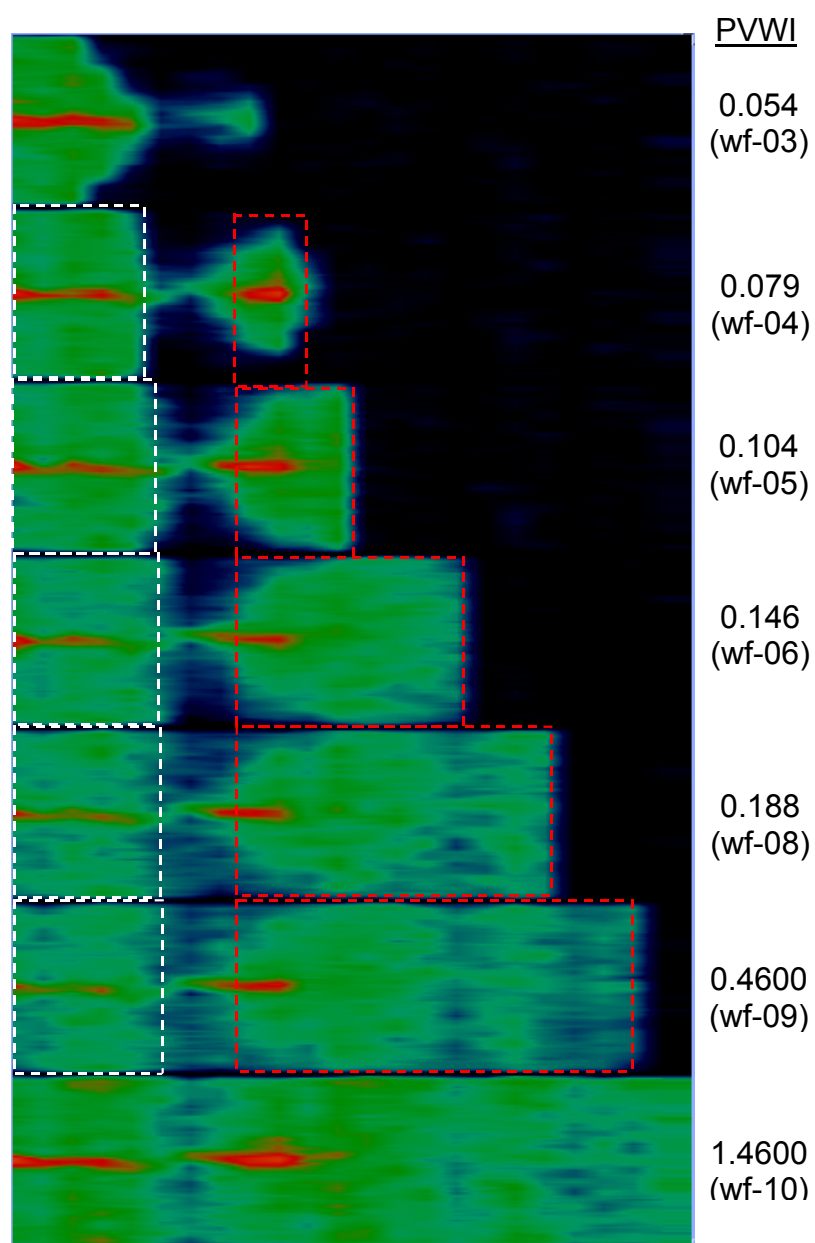


Figure 6.13: Axial slices showing water saturation during various stages of the water flood.

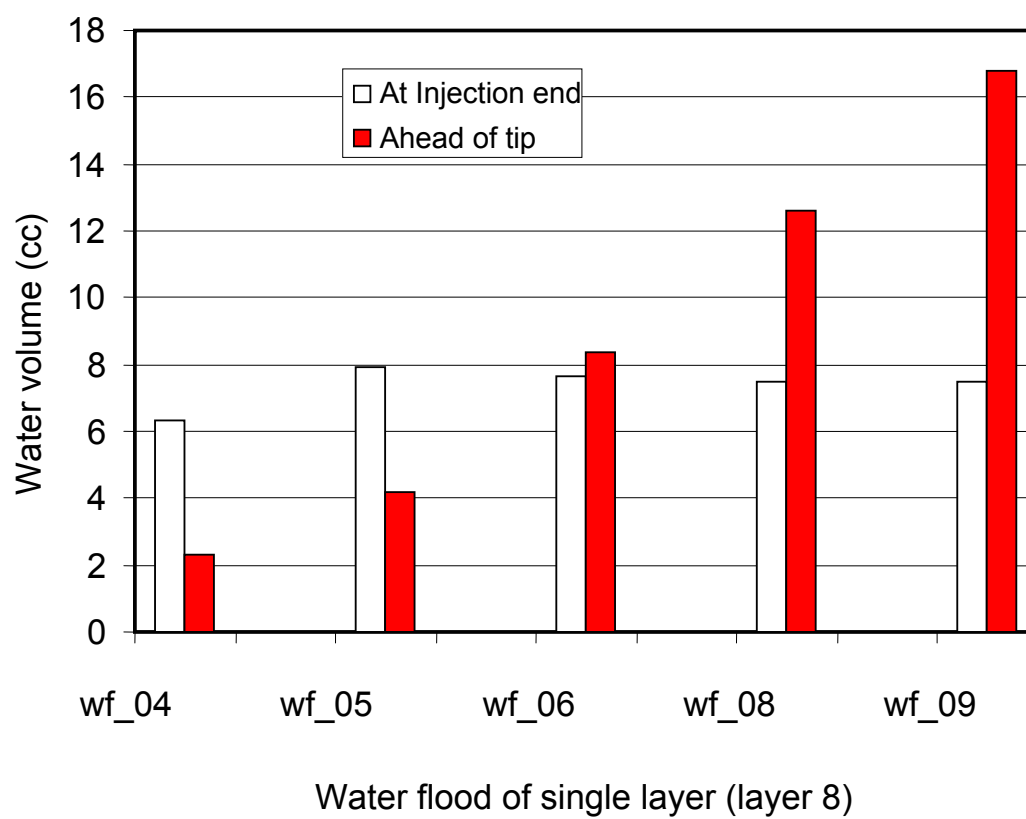


Figure 6.14: Illustration of water volume before and ahead of the fracture tip.

in the fractured region stayed almost fixed and the water volume in the non-fractured region kept growing. The capillary forces are the main factor controlling the observed behavior. A challenge in the water flood simulation is to obtain equilibrium between the capillary forces in the matrix and in the fracture. Different sets of capillary pressure curves for the matrix were tested, while the fracture capillary pressure curve was of low value with a flat appearance. The first capillary pressure set for the matrix was obtained from the literature, *Amyx et al.* (1961). Figure 6.15 shows three maps of axial slices of the water saturation. The first map had zero capillary pressure in the fracture. The second map had the fracture capillary pressure as the minimum value of the matrix capillary pressure curve. In the third map, the fracture capillary pressure is set as the matrix capillary pressure at 50% water saturation. Varying the value of the fracture capillary pressure had little impact on the resulting water distribution. There are three major flow regions. At the core inlet there is a displacement front that advances axially into the core. There is a water displacement front moving away from the fracture in the direction of the edges of the core. The fracture tip causes the flow to diverge vertically and create a low displacement “shadow” region at the tip of the fracture that persists over a long distance and time. The saturation “shadow” at the tip is caused by the sharpness of the matrix capillary pressure curve that has a sharp bend close to the residual saturation. This sharp bend and the strong convective flow component prevent the displacement of oil from the matrix block adjacent to the fracture in the axial direction.

Figure 6.16 shows the same three water saturation maps after the bend in the matrix capillary pressure curve was made less sharp than the curve shown in Figure 6.15.

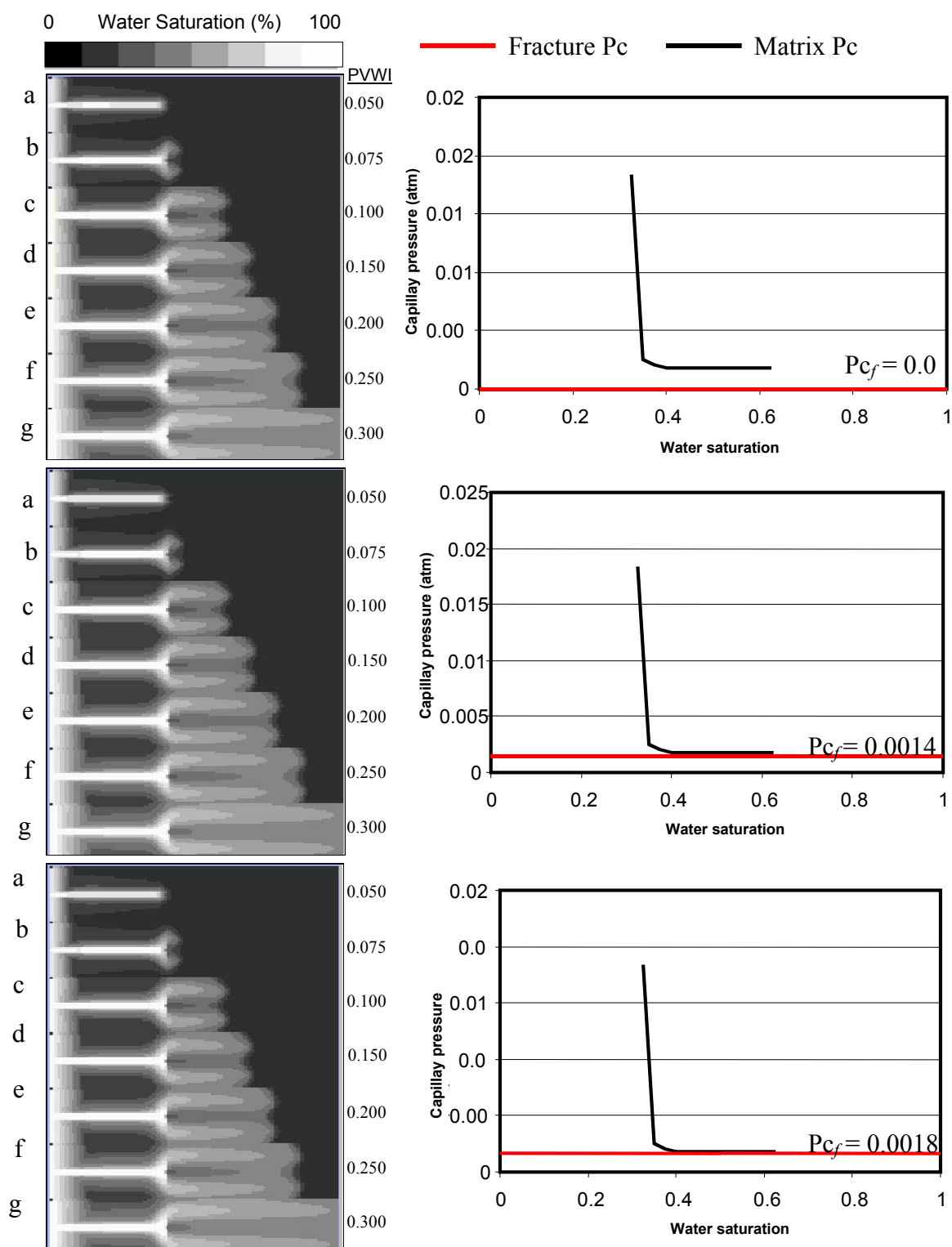


Figure 6.15: Illustration of first test of water saturation maps and capillary pressure curves.

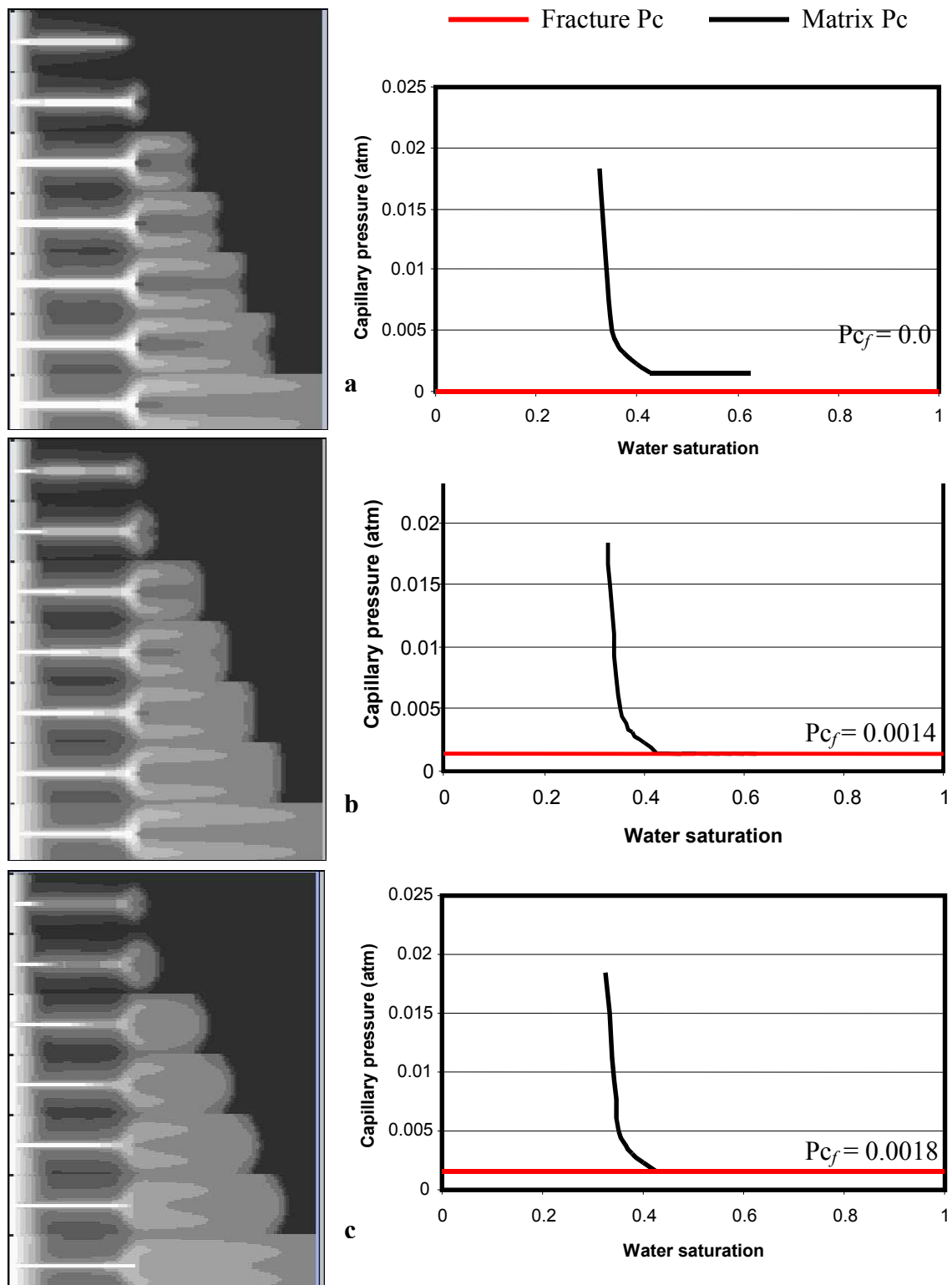


Figure 6.16: Illustration of second test water saturation maps and capillary pressure curves.

The saturation “shadow” at the fracture tip did not completely disappear, Figure 6.16 (a and b). However, the value of capillary pressure in the fracture has a significant effect on the displacement processes ahead of the fracture tip. As the capillary pressure of the fracture increased, the saturation “shadow” effect decreased, Figure 6.16c. The increase in the fracture capillary value is consistent with the vanishing nature of the fracture as the tip is approached.

Figure 6.17 shows a combination of one matrix capillary pressure curve and three fracture capillary pressure values. The matrix capillary pressure is more gradual than the ones used in Figure 6.15-16. The increase in the fracture capillary pressure value permitted axial flow at the tip of the fracture (Figure 6.17c) when it intersected the matrix capillary pressure curve. The high capillary pressure in the fracture causes the fracture to draw water into it from the matrix at the inlet end. The movement of water from the matrix to the fracture was not observed in the experiments. Figure 6.18 shows that a more gradual matrix capillary pressure curve than in Figures 6.15-17 could not avoid the “shadow” effect at the fracture tip. There is strong flow from the fracture to the matrix in the region along the fracture (Figure 6.18).

From the four tests presented in Figures 6.15-18, we conclude that the capillary forces play a major role in the water flood displacement and that the fracture capillary pressure should be smaller in value than the matrix. The matrix capillary pressure should not have a sharp bend close to the residual saturation. The next step in the capillary pressure adjustments was to modify sets number three and four (Figures 6.17-18) since they yielded results that were quite similar to the experimental results.

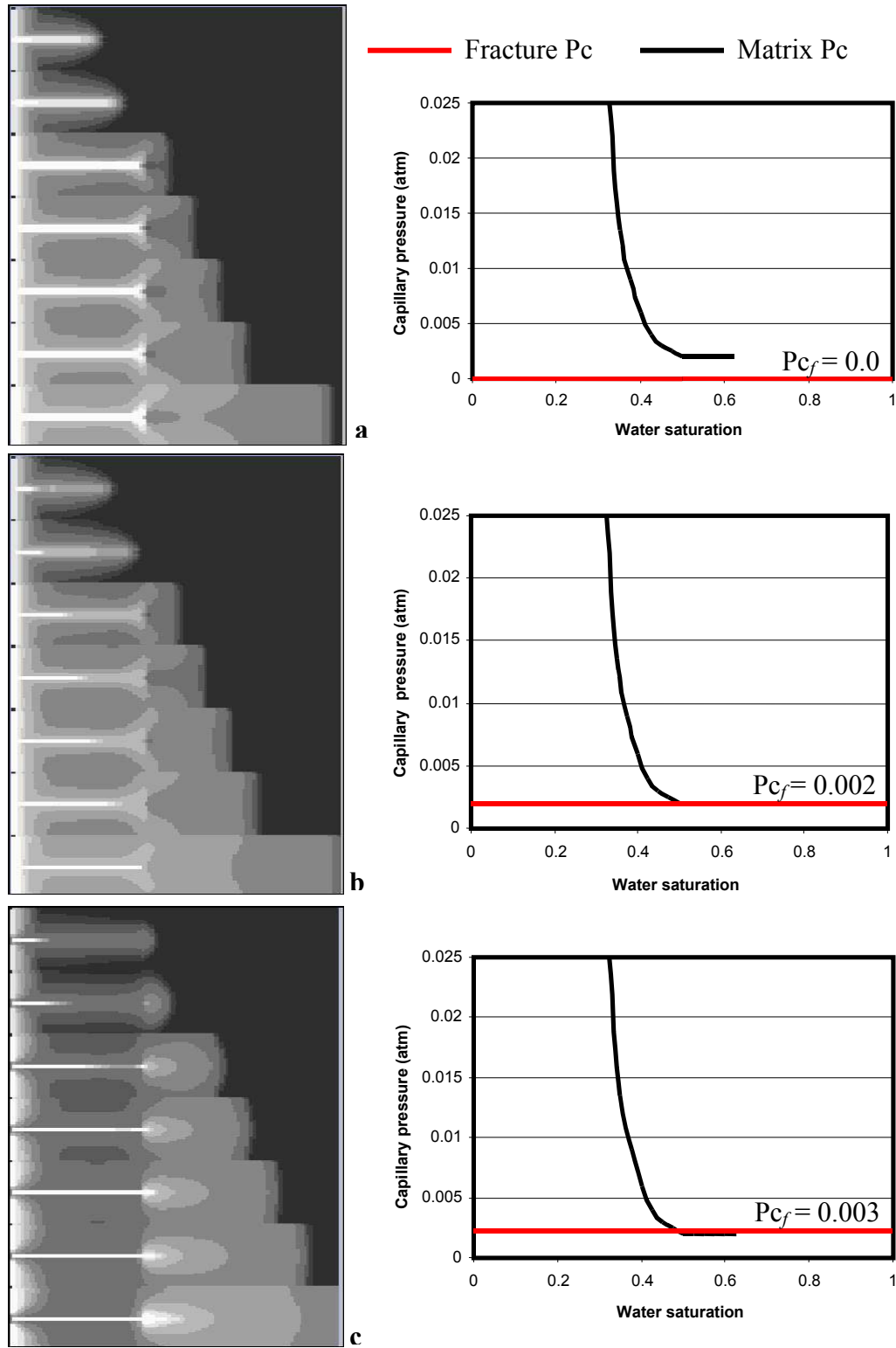


Figure 6.17: Illustration of third test of water saturation maps and capillary pressure curves.

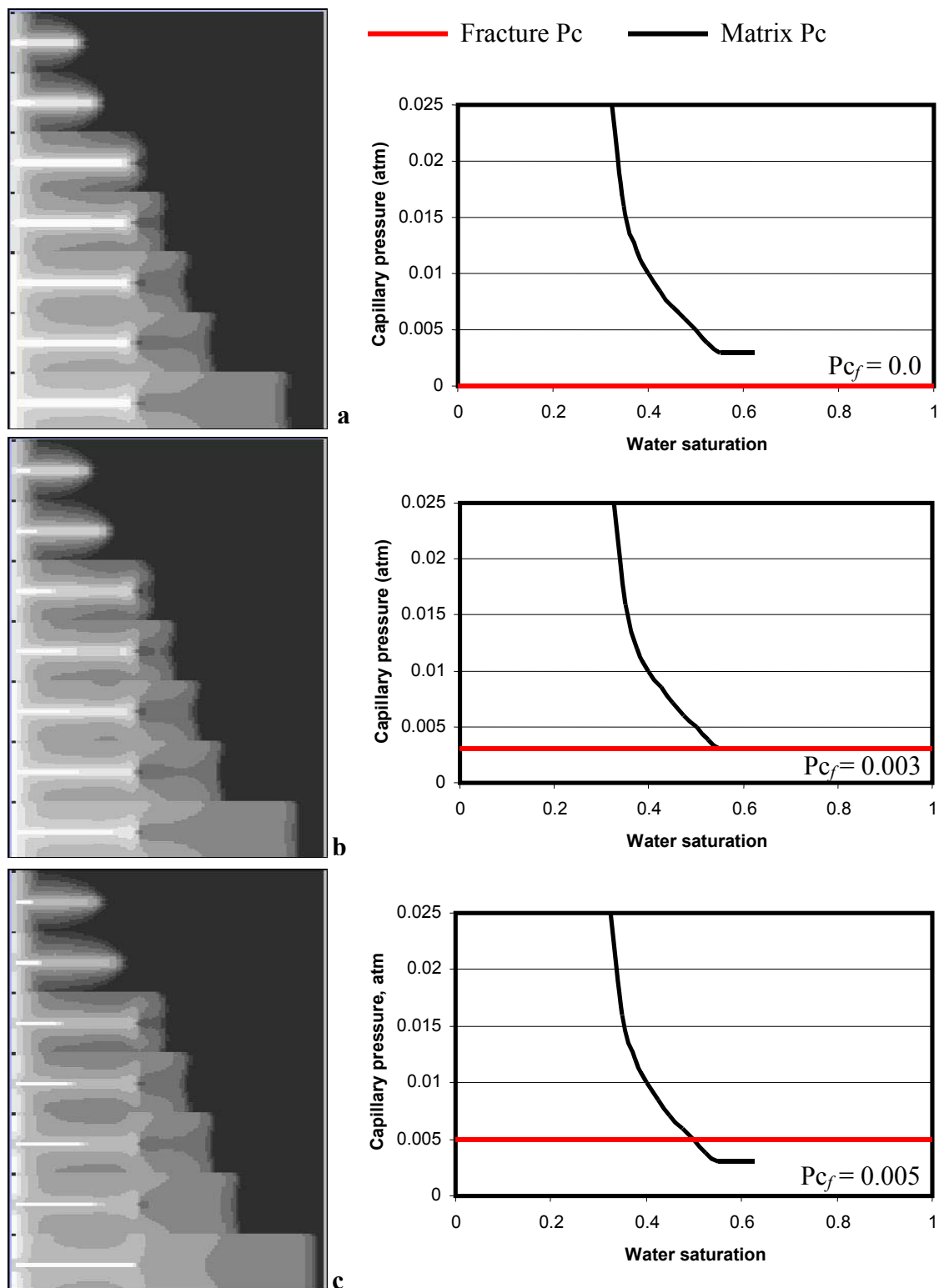


Figure 6.18: Illustration of fourth test of water saturation maps and capillary pressure curves.

Figure 6.19 shows the water saturation map of the modified matrix capillary pressure, which was reduced to establish a better sense of the capillarity between the fracture and the matrix. The saturation maps show no disturbance to the flow around the fracture tip region. To further improve the results, the capillary pressure curve of the fracture was slightly modified at low water saturations to reduce “leakage” from the fracture to the matrix in the central part of fracture. The relative permeability curves for the fracture were X-shaped in the mobile saturation range. Figure 6.20 shows the water saturation map and plots of the matrix and fracture capillary and relative permeability curves. The results are similar to the experimental data. It shows the oil being trapped in the fractured region and the water volume is not increasing near the injection end once the displacement at the tip spans most of the diameter of the core. At the same time, the water volume is increasing ahead of the fracture tip. When the water gets to the fracture tip and starts to form the waterfront, the injected water flows preferentially through the fracture to the tip where it diverges to flood the core ahead of the tip. The trapped oil in the matrix above and below the fracture was displaced away from the fracture at a low rate after water breakthrough.

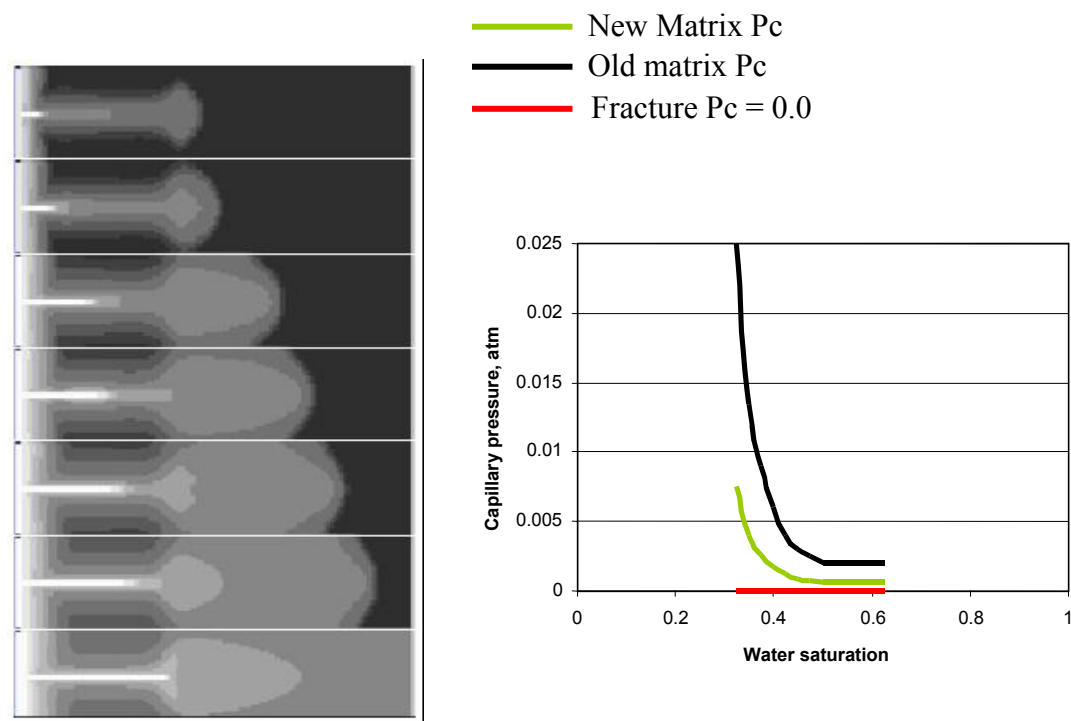


Figure 6.19: Illustration of water saturation map and capillary pressure curves after the improvement.

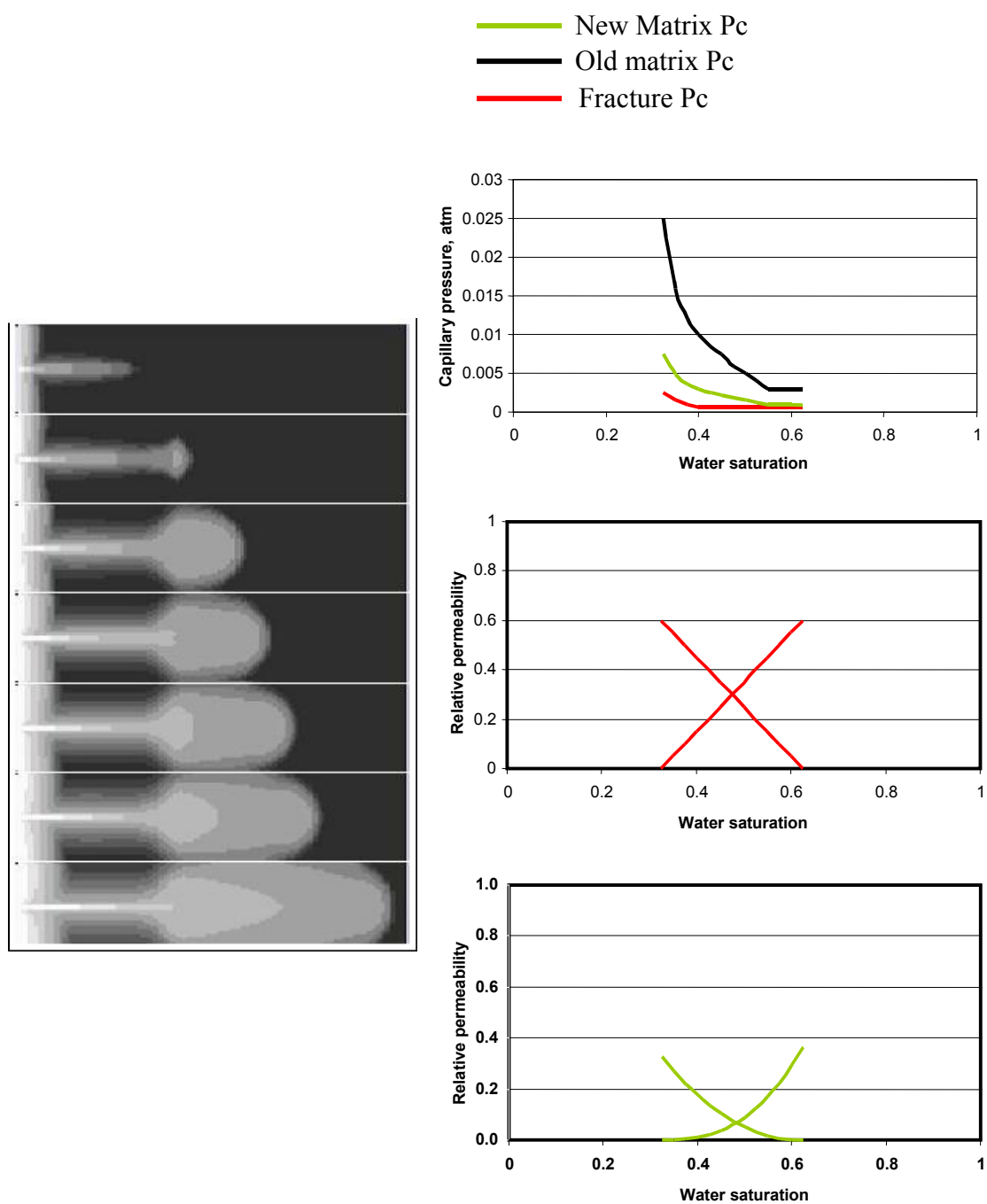


Figure 6.20: Illustration of water saturation map and capillary pressure and relative permeability curves for the matrix and fracture.

Chapter 7

CONCLUSIONS

Predicting the efficiency of fluid displacement processes in fractured rocks requires knowledge of capillary, gravity, and advective forces and the balance between these forces. This work quantifies the influence of a single fracture tip on fluid displacement processes in layered sandstone. Experimental and numerical data were evaluated. The sandstone layers provide a limited degree of heterogeneity to the system that is expressed through different values such as porosity, permeability, capillary pressure, and residual saturations. The superimposed extensional fracture adds a high-contrast preferential flow channel that changes the displacement process. The presented research provides a mechanistic understanding of the interaction between the flow in the matrix and the flow in the fracture. In addition, the presence of the fracture and its tip create a new opportunity to evaluate the contrast between the properties of the layers.

The conclusions are:

1. The displacing fluid flow pattern diverged away from the fracture along the entire length of the fracture due to the presence of the fracture tip at the down-stream end of the fracture. The presence of the fracture tip created significant vertical flow (perpendicular to the axis of the sample) which accentuated the contrast between the properties of the layers.

2. Inter-layer fluid transport in the matrix along the fracture was smaller than the inter-layer fluid transport in the matrix in the non-fractured region of the sample ahead of the fracture tip.
3. The fracture tip at the down-stream end of the fracture created an expanding two-phase flow region that diverged perpendicularly to the main axis of the sample that increased the resistance to flooding the matrix along the fracture. This increase in resistance to flow coupled with low capillary pressure in the fracture (in comparison to the matrix) forced the fluid to flow away from the fracture along the entire length of the fracture, thus, delaying the movement of the trapped phase. The divergence of the flow away from the fracture is not dependent on the finite size of the sample.
4. Capillary forces play different roles during the oil and the water displacement processes. During the initial oil flood, the early time displacement in the high k and ϕ layers (accentuated by the presence of the fracture tip) created capillary flow from the low k and ϕ layers to the high k and ϕ layers. During the water displacement process, the capillary-driven flow was from the high k and ϕ layers to the low k and ϕ layers (the opposite of what occurred in the oil flood).

Simulations with high values of fracture capillary pressure (in comparison to the matrix capillary pressure values) yielded converging fluid flow patterns that did not match the experimental results. The low Capillary pressure in the fracture in comparison to the capillary pressure in the matrix did not allow water to converge to the fracture from the matrix even close to the injection end of the sample, confirming the experimental observations.

Appendix D includes the references of the publications that the author published during the achievement of this work.

REFERENCES

Abdallah, G., Thoraval, A., Sfier, A., and Piguet, J. P. Thermal Convection of Fluid in Fractures Media. *Int. J. of Rock Mechanics and Mining Sciences*, 32 (5), 481-490,1995.

Akin, S., and B. Demiral, M. R. Effect of Flow Rate on Imbibition Three-Phase Relative Permeability and Capillary Pressures, SPE 38897 Proceedings of the SPE Annual Technical Conference and Exhibition, San Antonio, Texas, 5-9 October 1997.

Akin, S., and Kovscek, A. R. Imbibition Studies of Low Permeability Porous Media, SPE 54590, Proceedings of SPE Western Regional Meeting, Anchorage, Alaska, 26-27 May 1999.

Alajmi, A. F. Analysis of Fracture-Matrix Fluid Flow Interaction Using X-Ray CT. MS Thesis, The Pennsylvania State University, University park, Pennsylvania, 1999.

Al-Wadhahi, M. A. Interfacial Tension Behavior of Water, n-Decane and Benzyl Alcohol Mixtures. MS Thesis, The Pennsylvania State University, University park, Pennsylvania, 1994.

Amyx, J. W., Bass, D. M., Whiting, R. L. Petroleum Reservoir Engineering. Physical Properties, 1960.

Archer, J. S., and Wong, S.W. Use of a Reservoir Simulator to Interpret Laboratory Water Flood Data. *Soc. Pet. Eng. J* , 343-347, December. 1973.

Chardaire-Riviere, C., Chavent, G., Jaffre, J., and Liu, J. Multiscale Representation for Simultaneous Estimation of the Relative Permeabilities and Capillary Pressure. SPE 20501, Preceedings of the 25th Annual Technical Conference and Exhibition of the Society of Petroleum Engineers, New Orleans, LA, 23-26 September, 1990.

Chardaire-Riviere, C., Chavent, G., Jaffre, J., Liu, J., and Bourblaux, B. J. Simultaneous Estimation of the Relative Permeabilities and Capillary Pressure. *SPE Formation Evaluation* , 283-289, December 1992.

Grader, A. S., Balzarini, M., Radaelli, F., Capasso, G., Pellegrino, A. Fracture-Matrix Flow: Quantification and Visualization Using X-ray Computer Tomography. AGU Monograph 122, 157-168, October 2000.

Kerig, P. D., and Watson A. T. A New Algorithm for Estimating Relative Permeabilities From the Displacement Experiments. *SPE Reservoir Engineering*, 103-112, February 1987.

Kruger, W. D. Determining Areal Permeability Distribution by Calculations. *J. Pet. Tech.* 691-696, June 1961.

Kulkarni R. N., and Datta-Gupta A. Estimating Relative Permeability from production Data: A streamline Approach. SPE 56751, Proceedings of the SPE Annual Technical Conference and Exhibition, Houston, Texas, 3-6 October 1999.

Nordtvedt, J. E., Mejia, G., Yang, P. H., and Watson, A. T. Estimation of Capillary Pressure and Relative Permeability Functions from Centrifuge Experiments. *SPE Reservoir Engineering*, 292-298, November 1993.

Nordtvedt, J. E., Ebeltoft, E., Iversen, J. E., Sylte, A., Urkedal, H., Vantne, K. O., and Watson, A. T. Determination of Three-Phase Relative Permeabilities from the Displacement Experiments. SPE 32683, Proceedings of the SPE Annual Technical Conference and Exhibition, Denver, Colorado, U.S.A., 6-9 October 1996.

Savioli G. B., Grattoni C. A., and Bidner M. S. On the Inverse Problem Application to Reservoir Characterization. SPE 25522, UNSOLICITED 1992.

Sigmund, P. M., and McCaffery, F. G. An Improved Unsteady State Procedure for Determining the Relative-Permeability Characteristics of Heterogeneous Porous Media. *Soc. Pet. Eng. J.*, 15-28, February 1979.

Waite, M. E., Ge, S., and Spetzler, H. A new Conceptual Model for Fluid Flow in Discrete Fractures: An Experimental and Numerical Study. *J. of Geophysical Res.* Vol. 104, No. B6, 13049-13059, June 10, 1999.

Walsh, J. B. Effect of Pore Pressure and confining Pressure on Fracture Permeability. *Int. J. Rock Mechanics*, 18, 429-435, 1981.

Watson, A. T., Seinfeld, J. H., Gavalas, G. R., and Woo, P. T. History Matching in Two-Phase Petroleum Reservoirs. *Soc. Pet. Eng. J.*, 521-532, 1980.

Watson, A. T., Herig, P. D., Richmond, P. C., and Tao, T. M. An Improved Method for Estimating Relative Permeability from the Displacement Experiments. SPE 15064, Proceedings of the 56th California Regional Meeting of the Society of Petroleum Engineering, Oakland, CA, 2-4 April 1986.

Yang, P. H., and Watson, A. T. A Bayesian Methodology for Estimating Relative Permeability Curves. *SPE Reservoir Engineering*, 259-225, May. 1991.


```

INCLUDE                                LAB  13:25 24 MAR 01
  'data_11'  /

INCLUDE                                LAB  10:58 24 MAR 01
  'data_266' /

INCLUDE                                LAB  10:59 24 MAR 01
  'data_33'  /

INCLUDE                                LAB  11:00 24 MAR 01
  'data_44'  /

INCLUDE                                LAB  11:00 24 MAR 01
  'data_888' /

INCLUDE                                LAB  11:00 24 MAR 01
  'data_999' /

OLDTRANR

INIT

SAVE                                LAB  15:21 20 MAR 01
  'UNFORMATTED ' /

PROPS

DENSITY      1 TABLES    20 P NODES    20 R NODES    LAB  18:45 17 MAR 01
  1.02740    1.04240    0.00000  /

PVDO          1 TABLES    20 P NODES    20 R NODES    LAB  18:46 17 MAR 01
  2.2000 1.00000 5.16100
  2.2110 0.99999 5.12500
  2.2220 0.99998 5.17200
  2.46030 0.99997 5.17600
  2.2440 0.99996 5.18000
  2.4550 0.99995 5.18500
  2.6060 0.99994 5.19000
  2.8070 0.99993 5.19500
/

PVTW          1 TABLES    20 P NODES    20 R NODES    LAB  18:48 17 MAR 01
  2.4050    1.00000    0.0000000    1.04400    0.00E+00 /

INCLUDE                                LAB  18:46 29 MAR 01
  'krs.data'                        '  /

ROCK          1 TABLES    20 P NODES    20 R NODES    LAB  10:45 26 MAR 01
  2.4050          5.9E-06  /

REGIONS

```


EQUALS

'SATNUM' 1 1 1 1 610 1 25 /
 'SATNUM' 1 1 1 1 610 27 51 /
 'SATNUM' 1 1 1 251 610 26 26 /
 'SATNUM' 2 1 1 1 250 26 26 /
 /

SOLUTION

AQUCT

1	5.0	2.0	10000000.0	1.0	1
2.5	5.0	1	1	1	1/

AQUANCON

1 1 1 1 1 1 51 'J-'/
 /

PRESSURE

31110*2.0004050
 /

LAB 06:53 24 MAR 01

SWAT

31110*0.0
 /

LAB 06:53 24 MAR 01

SUMMARY

SEPARATE

RUNSUM

WOPR

'WELL1'
 /

LAB 18:05 17 MAR 01

WWPR

'WELL1'
 /

LAB 18:57 29 MAR 01

WWCT

'WELL1'
 /

LAB 18:57 29 MAR 01

WBHP

'WELL1'
 /

LAB 18:06 17 MAR 01

RPTSMRY

1 /

LAB 12:54 25 MAR 01

SCHEDULE

WELSPPCS LAB 15:43 25 MAR 01
 'WELL1 ','WAT-LER ' 1 610 1* 'LIQ' 1* 'STD'
 'SHUT','YES' 1* 'SEG' 1* /
 /

COMPDAT LAB 15:11 25 MAR 01
 'WELL1 ' 1 610 1 51 'OPEN' 1* 1* 0.01985000
 1* 1* 1* 'Z' /
 /

WCONPROD LAB 18:43 17 MAR 01
 'WELL1 ','OPEN','BHP' 1* 1* 1*
 1* 1* 1.00 1* 1* 1* /
 /

RPTSCHED LAB 17:07 30 MAR 01
 'SWAT' /

TUNING LAB 14:25 460 MAR 01
 0.01 0.01 0.01 1*
 1* 1* 1* 1* 1*
 /
 1* 1* 1* 1*
 1* 1* 1* 1*
 1* 1* 1*
 /
 1* 1* 80 1* 1* 1* 1* 1* 1* 1*
 /

TSTEP LAB 15:05 26 MAR 01
 1*1.25
 /

END

INCLUDE LAB 13:25 24 MAY 95

```

'data_15_11' /

INCLUDE                                LAB    10:58 24 MAY 95
'data_44' /

INCLUDE                                LAB    10:59 24 MAY 95
'data_3333' /

INCLUDE                                LAB    11:00 24 MAY 95
'data_15_6' /

INCLUDE                                LAB    11:00 24 MAY 95
'data_88' /

INCLUDE                                LAB    11:00 24 MAY 95
'data_kz' /

OLDTRANR

INIT

SAVE                                LAB    15:21 20 FEB 93
'UNFORMATTED ' /

PROPS

DENSITY      1 TABLES    20 P NODES    20 R NODES    LAB    18:45 17 FEB 98
1.04240    1.02740    0.00000 /

PVDO          1 TABLES    20 P NODES    20 R NODES    LAB    18:46 17 FEB 98
2.2000 1.00000 1.16100
2.2110 0.99999 1.12500
2.2220 0.99998 1.17200
2.46030 0.99997 1.17600
2.2440 0.99996 1.18000
2.4550 0.99995 1.18500
2.6060 0.99994 1.19000
2.8070 0.99993 1.19500
/

PVTW          1 TABLES    20 P NODES    20 R NODES    LAB    18:48 17 FEB 98
2.4050    1.00000    0.0000000    5.44000    0.00E+00 /

INCLUDE                                LAB    18:46 29 MAY 95
'krs.data'                                ' /

ROCK          1 TABLES    20 P NODES    20 R NODES    LAB    10:45 26 MAY 95
2.4050          5.9E-06 /

REGIONS
EQUALS

```

```

'SATNUM' 1 1 15 1 200 26 26 /
'SATNUM' 2 1 1 1 460 1 25 /
'SATNUM' 3 2 2 1 460 1 25 /
'SATNUM' 4 3 3 1 460 1 25 /
'SATNUM' 5 4 4 1 460 1 25 /
'SATNUM' 6 5 5 1 460 1 25 /
'SATNUM' 7 6 6 1 460 1 25 /
'SATNUM' 8 7 7 1 460 1 25 /
'SATNUM' 9 8 8 1 460 1 25 /
'SATNUM' 10 9 9 1 460 1 25 /
'SATNUM' 11 10 10 1 460 1 25 /
'SATNUM' 12 11 11 1 460 1 25 /
'SATNUM' 13 12 12 1 460 1 25 /
'SATNUM' 14 13 13 1 460 1 25 /
'SATNUM' 15 14 14 1 460 1 25 /
'SATNUM' 16 15 15 1 460 1 25 /
'SATNUM' 2 1 1 1 460 27 51 /
'SATNUM' 3 2 2 1 460 27 51 /
'SATNUM' 4 3 3 1 460 27 51 /
'SATNUM' 5 4 4 1 460 27 51 /
'SATNUM' 6 5 5 1 460 27 51 /
'SATNUM' 7 6 6 1 460 27 51 /
'SATNUM' 8 7 7 1 460 27 51 /
'SATNUM' 9 8 8 1 460 27 51 /
'SATNUM' 10 9 9 1 460 27 51 /
'SATNUM' 11 10 10 1 460 27 51 /
'SATNUM' 12 11 11 1 460 27 51 /
'SATNUM' 13 12 12 1 460 27 51 /
'SATNUM' 14 13 13 1 460 27 51 /
'SATNUM' 15 14 14 1 460 27 51 /
'SATNUM' 16 15 15 1 460 27 51 /
'SATNUM' 2 1 1 11 460 26 26 /
'SATNUM' 3 2 2 11 460 26 26 /
'SATNUM' 4 3 3 11 460 26 26 /
'SATNUM' 5 4 4 11 460 26 26 /
'SATNUM' 6 5 5 11 460 26 26 /
'SATNUM' 7 6 6 11 460 26 26 /
'SATNUM' 8 7 7 11 460 26 26 /
'SATNUM' 9 8 8 11 460 26 26 /
'SATNUM' 10 9 9 11 460 26 26 /
'SATNUM' 11 10 10 11 460 26 26 /
'SATNUM' 12 11 11 11 460 26 26 /
'SATNUM' 13 12 12 11 460 26 26 /
'SATNUM' 14 13 13 11 460 26 26 /
'SATNUM' 15 14 14 11 460 26 26 /
'SATNUM' 16 15 15 11 460 26 26 /
/

```

SOLUTION

AQUCT

1	5.0	2.0	10000000.0	1.0	1
2.5	5.0	1	1	1	1/

AQUANCON

1 1 15 1 1 1 51 'J-'/
/

PRESSURE
351900*1.0004050
/

LAB 06:53 24 JUN 95

SWAT
351900*0.0
/

LAB 06:53 24 JUN 95

SUMMARY

SEPARATE

RUNSUM

WOPR
'WELL1'
'WELL2'
'WELL3'
'WELL4'
'WELL5'
'WELL6'
'WELL7'
'WELL8'
'WELL9'
'WELL10'
'WELL11'
'WELL12'
'WELL13'
'WELL14'
'WELL15'
/

LAB 18:05 17 FEB 98

WWPR
'WELL1'
'WELL2'
'WELL3'
'WELL4'
'WELL5'
'WELL6'
'WELL7'
'WELL8'
'WELL9'
'WELL10'
'WELL11'
'WELL12'
'WELL13'
'WELL14'
'WELL15'
/

LAB 18:57 29 MAY 95

WBHP

LAB 18:06 17 FEB 98

'WELL1'
 'WELL2'
 'WELL3'
 'WELL4'
 'WELL5'
 'WELL6'
 'WELL7'
 'WELL8'
 'WELL9'
 'WELL10'
 'WELL11'
 'WELL12'
 'WELL13'
 'WELL14'
 'WELL15'
 /

RPTSMRY

LAB 12:54 25 MAY 95

1 /

SCHEDULE

WELSPPCS

LAB 15:43 25 MAR 99

'WELL1'	','	'WAT-LER'	1	460	1*	'LIQ'	1*	'STD'
'SHUT'	'YES'	1*	'SEG'	1*	/			
'WELL2'	','	'WAT-LER'	2	460	1*	'LIQ'	1*	'STD'
'SHUT'	'YES'	1*	'SEG'	1*	/			
'WELL3'	','	'WAT-LER'	3	460	1*	'LIQ'	1*	'STD'
'SHUT'	'YES'	1*	'SEG'	1*	/			
'WELL4'	','	'WAT-LER'	4	460	1*	'LIQ'	1*	'STD'
'SHUT'	'YES'	1*	'SEG'	1*	/			
'WELL5'	','	'WAT-LER'	5	460	1*	'LIQ'	1*	'STD'
'SHUT'	'YES'	1*	'SEG'	1*	/			
'WELL6'	','	'WAT-LER'	6	460	1*	'LIQ'	1*	'STD'
'SHUT'	'YES'	1*	'SEG'	1*	/			
'WELL7'	','	'WAT-LER'	7	460	1*	'LIQ'	1*	'STD'
'SHUT'	'YES'	1*	'SEG'	1*	/			
'WELL8'	','	'WAT-LER'	8	460	1*	'LIQ'	1*	'STD'
'SHUT'	'YES'	1*	'SEG'	1*	/			
'WELL9'	','	'WAT-LER'	9	460	1*	'LIQ'	1*	'STD'
'SHUT'	'YES'	1*	'SEG'	1*	/			
'WELL10'	','	'WAT-LER'	10	460	1*	'LIQ'	1*	'STD'
'SHUT'	'YES'	1*	'SEG'	1*	/			
'WELL11'	','	'WAT-LER'	11	460	1*	'LIQ'	1*	'STD'
'SHUT'	'YES'	1*	'SEG'	1*	/			
'WELL12'	','	'WAT-LER'	12	460	1*	'LIQ'	1*	'STD'
'SHUT'	'YES'	1*	'SEG'	1*	/			
'WELL13'	','	'WAT-LER'	13	460	1*	'LIQ'	1*	'STD'
'SHUT'	'YES'	1*	'SEG'	1*	/			
'WELL14'	','	'WAT-LER'	14	460	1*	'LIQ'	1*	'STD'
'SHUT'	'YES'	1*	'SEG'	1*	/			
'WELL15'	','	'WAT-LER'	15	460	1*	'LIQ'	1*	'STD'
'SHUT'	'YES'	1*	'SEG'	1*	/			

/

COMPDAT							LAB	15:11	25 MAR	99
'WELL1	'	1	460	1	51	'OPEN'	1*	1*	0.06985000	
1*		1*	1*			'Z' /				
'WELL2	'	2	460	1	51	'OPEN'	1*	1*	0.06985000	
1*		1*	1*			'Z' /				
'WELL3	'	3	460	1	51	'OPEN'	1*	1*	0.06985000	
1*		1*	1*			'Z' /				
'WELL4	'	4	460	1	51	'OPEN'	1*	1*	0.06985000	
1*		1*	1*			'Z' /				
'WELL5	'	5	460	1	51	'OPEN'	1*	1*	0.06985000	
1*		1*	1*			'Z' /				
'WELL6	'	6	460	1	51	'OPEN'	1*	1*	0.06985000	
1*		1*	1*			'Z' /				
'WELL7	'	7	460	1	51	'OPEN'	1*	1*	0.06985000	
1*		1*	1*			'Z' /				
'WELL8	'	8	460	1	51	'OPEN'	1*	1*	0.06985000	
1*		1*	1*			'Z' /				
'WELL9	'	9	460	1	51	'OPEN'	1*	1*	0.06985000	
1*		1*	1*			'Z' /				
'WELL10	'	10	460	1	51	'OPEN'	1*	1*	0.06985000	
1*		1*	1*			'Z' /				
'WELL11	'	11	460	1	51	'OPEN'	1*	1*	0.06985000	
1*		1*	1*			'Z' /				
'WELL12	'	12	460	1	51	'OPEN'	1*	1*	0.06985000	
1*		1*	1*			'Z' /				
'WELL13	'	13	460	1	51	'OPEN'	1*	1*	0.06985000	
1*		1*	1*			'Z' /				
'WELL14	'	14	460	1	51	'OPEN'	1*	1*	0.06985000	
1*		1*	1*			'Z' /				
'WELL15	'	15	460	1	51	'OPEN'	1*	1*	0.06985000	
1*		1*	1*			'Z' /				

/

WCONPROD							LAB	18:43	17 FEB	98
'WELL1	'	'OPEN'	'BHP'	1*	1*	1*				
1*	1*	1.00		1*	1*	1*	/			
'WELL2	'	'OPEN'	'BHP'	1*	1*	1*				
1*	1*	1.00		1*	1*	1*	/			
'WELL3	'	'OPEN'	'BHP'	1*	1*	1*				
1*	1*	1.00		1*	1*	1*	/			
'WELL4	'	'OPEN'	'BHP'	1*	1*	1*				
1*	1*	1.00		1*	1*	1*	/			
'WELL5	'	'OPEN'	'BHP'	1*	1*	1*				
1*	1*	1.00		1*	1*	1*	/			
'WELL6	'	'OPEN'	'BHP'	1*	1*	1*				
1*	1*	1.00		1*	1*	1*	/			
'WELL7	'	'OPEN'	'BHP'	1*	1*	1*				
1*	1*	1.00		1*	1*	1*	/			
'WELL8	'	'OPEN'	'BHP'	1*	1*	1*				
1*	1*	1.00		1*	1*	1*	/			
'WELL9	'	'OPEN'	'BHP'	1*	1*	1*				
1*	1*	1.00		1*	1*	1*	/			
'WELL10	'	'OPEN'	'BHP'	1*	1*	1*				

1*	1*	1.00	1*	1*	1*	/
'WELL11	'	'OPEN','BHP'	1*	1*	1*	1*
1*	1*	1.00	1*	1*	1*	/
'WELL12	'	'OPEN','BHP'	1*	1*	1*	1*
1*	1*	1.00	1*	1*	1*	/
'WELL13	'	'OPEN','BHP'	1*	1*	1*	1*
1*	1*	1.00	1*	1*	1*	/
'WELL14	'	'OPEN','BHP'	1*	1*	1*	1*
1*	1*	1.00	1*	1*	1*	/
'WELL15	'	'OPEN','BHP'	1*	1*	1*	1*
1*	1*	1.00	1*	1*	1*	/

/

RPTSCHED
'SWAT' /

LAB 17:07 30 JUN 99

TUNING
0.00051 0.00051 0.00051
1* 1* 1*

LAB 14:25 460 OCT 98

/

1*	1*	1*	1*
1*	1*	1*	1*
1*	1*	1*	

/

1*	1*	80	1*	1*	1*	1*	1*	1*	1*
----	----	----	----	----	----	----	----	----	----

/

TSTEP
1*1.65
/

LAB 15:05 26 MAR 99

END

APPENDIX C

BATCH FILE

```
#!/bin/csh -f

set count = 2000
while ($count)

krs.out
@eclipse OIL
cat WF.PRT | grep "(\\*" | cut -c14-21 | sed s/\\*/\\./g > old.data
getJold.out >> abd
error.out >> error.data

deltaA.out
@eclipse OIL
cat WF.PRT | grep "(\\*" | cut -c14-21 | sed s/\\*/\\./g > A.data
getJa.out >> abd

deltaB.out
@eclipse OIL
cat WF.PRT | grep "(\\*" | cut -c14-21 | sed s/\\*/\\./g > B.data
getJb.out

deltaC.out
@eclipse OIL
cat WF.PRT | grep "(\\*" | cut -c14-21 | sed s/\\*/\\./g > C.data
getJc.out

deltaD.out
@eclipse OIL
cat WF.PRT | grep "(\\*" | cut -c14-21 | sed s/\\*/\\./g > D.data
getJd.out

deltaE.out
@eclipse OIL
cat WF.PRT | grep "(\\*" | cut -c14-21 | sed s/\\*/\\./g > E.data
getJe.out

G.out >> check
J.out >> A.matrix
gauss.out

newabcd.out >> abd
```

```
#!/bin/rm junky

coeff.out >> coeff.data
sum.out >> sum.data

@ count--

end
#end outer loop

999: echo "The program is done!"

echo
```

APPENDIX D

PUBLICATIONS

Alajmi, A. F., and Grader, A. S., Analysis of Fracture-Matrix Fluid Flow Interaction Using X-Ray CT, *SPE* 65628 presented at 2000 SPE Eastern Regional meeting in Morgantown, West Virginia, 17-19 October 2000.

Alajmi, A. F., and Grader., The Impact of a single fracture on fluid flow displacement, *KIPCE-A08*, Proceedings of the Kuwait International Petroleum Conference and Exhibition on IOR management, Kuwait City, Kuwait, 14-16 December 2002.

Alajmi, A. F., and Grader, A. S., Multi-Phase Flow in the Presence of a Fracture Tip: Experiments and Modeling, *A91*, Proceeding of the Society of Core Analysis International Conference , Pau, France, 21-24 September 2003.

Karpyn, Z., Alajmi, A. F., Parada, C., Grader, A. S., Halleck, P., and Karacan, O., Mapping Fracture Aperture Using Micro Computing Tomography, *A24*, Proceeding of the Society of Core Analysis International Conference , Pau, France, 21-24 September 2003.

VITA

Abdullah F. Alajmi is from a small town south of Kuwait city called Abu-Halifa. He was born on September 18, 1971. He attended Abu-Halifa high school and graduated in 1989. He earned his B.S. in Petroleum Engineering from Marietta College in Marietta, Ohio in spring 1995. He joined Kuwait Oil Company in August 1995 as production operation engineer. In summer 1997, he was granted a scholarship from the Petroleum Engineering Department in Kuwait University to continue his graduate studies. He resigned from Kuwait Oil Company in December 1997 and joined Kuwait University. In January 1998 he started his graduate studies with Pennsylvania State University in the Petroleum and Natural Gas Engineering. He earned his Master of Science on December 1999. He received his doctoral degree in the Petroleum and Natural Gas Engineering on August 2003 from the Pennsylvania State University. Beside his academic achievement, he had social activities. He was nominated with the Almu'tadila list for the National Union of Kuwaiti Students in the U.S. branch in November 2000. He co-founded the Kuwaiti Student Association in the Pennsylvania State University in Fall 2000. He was elected as the association Public Relation Officer from January 2001 to August 2001. He was the association's advisor from August 2001 to August 2002 and from August 2002 to August 2003. He was elected as the General Secretary of the Islamic Society of Central Pennsylvania from February 2002 to February 2003. His hobbies are reading, travel, and soccer. He is a member of Society of Petroleum Engineering (SPE) and the Society of Core Analysis (SCA). He will join Kuwait University in August 2003 as a faculty member of the Petroleum Engineering Department.